Molecular-Scale Devices from First Principles

by

Nicholas E. Singh-Miller

M.S., Materials Science and Engineering
Case Western Reserve University, 2004

B.S., Materials Science and Engineering
Case Western Reserve University, 2002

Submitted to the Department of Materials Science and Engineering
in partial fulfillment of the requirements for the degree of

Doctor of Philosophy in Materials Science and Engineering

at the

MASSACHUSETTS INSTITUTE OF TECHNOLOGY

June 2009

Author .....
Department of Materials Science and Engineering
April 23, 2009

Certified by .....
Nicola Marzari
Associate Professor
Thesis Supervisor

Accepted by .....
Christine Ortiz
Chairman, Department Committee on Graduate Students

Molecular-Scale Devices from First Principles

by

Nicholas E. Singh-Miller

Submitted to the Department of Materials Science and Engineering
on April 23, 2009, in partial fulfillment of the
requirements for the degree of
Doctor of Philosophy in Materials Science and Engineering

Abstract

Electronic structure calculations are becoming more widely applied to complex and realistic materials systems and devices, reaching well into the domain of nanotechnology, with applications that include metal-molecule junctions, carbon-nanotube field effect transistors, and nanostructured metals or semiconductors. For such complex systems, characterizing the properties of the elementary building blocks becomes of fundamental importance. In this thesis we employ first-principles calculations based on density-functional theory (DFT) to investigate fundamental properties of molecular-scale devices. We focus initially on the constituent components of these devices (polymers, metal surfaces, carbon nanotubes), following with studies of entire device geometries (nanotube/metal interfaces).

We first study a proposed molecular actuating system in which the interaction between oligothiophenes is the driving force behind an electromechanical response. The oligothiophenes are attracted to each other through π-stacking interactions driven by redox reactions. We show that counterions strengthen this interaction further through enhanced screening of the electrostatic repulsion. Many molecular scale devices require contact with a metallic conductor, we also study the fundamental properties of metal surfaces in the slab-supercell approximation; in particular layer relaxation, surface energy, work function, and the effect that slab thickness has on these properties. The surfaces of interest are the low index, (111), (100), and (110) surfaces of Al, Au, Pd, and Pt and the close packed (0001) surface of Ti. We show that these properties are well converged for slabs that have between 5 and 10 layers, depending on the property considered and the surface orientation.

We then focus on understanding and characterizing devices. Since it is widely proposed that carbon nanotubes (CNTs) could replace Si in future transistor devices, we examine the work function of single-wall CNTs and the effects that covalent functionalization could have in engineering performance. Electrostatic dipoles form due to the charge asymmetries in the functionalized CNT unit cell, and the use of periodic boundary conditions affects our calculations. We correct for these spurious dipole-

dipole interactions with a real-space potential derived directly from the solution to Poisson's equation in real-space with open boundary conditions. We find that the functionalizations can be clearly labeled as electropositive and electronegative, and that they decrease or increase the work function of the CNT accordingly.

Finally, we join metal surfaces and CNTs to study Schottky barrier heights (SBHs) that form at the interface. We take Al(111) and Pd(111) as examples of low- and high-work function metal surfaces and contact them with the semiconducting (8,0) CNT. We find that in all cases a surface dipole forms that shifts the band structure of the CNT locally. In these systems, we investigate the effects of surface roughness and functionalization on SBHs, and find that controlling the electrostatics at the interface (with functionalization, adsorbates, and device geometry) can lead to further engineering of the SBHs.

Thesis Supervisor: Nicola Marzari
Title: Associate Professor

Acknowledgments

I am thankful for having a great guide and mentor in my advisor, Nicola Marzari. He had the patience to take on me, a student with a background in experimental work, and guide me through this theoretical and computational world, allowing for a few pit stops in India and industry. All the while he has taught me to be a rigorous thinker, clearer speaker, and better writer.

I have had the pleasure of coming into contact with a few professors over the years. I thank my committee members, Prof. Stellacci, Prof. Bulovic, and Prof. Yip, for taking the time to provide suggestions about my thesis work and for good conversations about the future. I thank Prof. Sebastian and Prof. Narasimhan for being outstanding hosts while I visited and studied in India. I thank Prof. Lechtman for broadening my understanding of Materials Science and ultimately its place in human history.

The quasiamore group has been a great support structure both professionally and socially. I have had the great pleasure of collaborating over the years with Damian Scherils, Young-Su Lee, Ismaila Dabo, and Boris Kozinsky.

I am grateful for the support and motivation that my parents and grandparents have always provided, even if it occasionally came in the form of that dreaded question, "So, when are you going to graduate?" This small accomplishment is also in some part due to the constant support of the extended families of mine. My parents-in-law have been there for many ups and downs. My siblings and siblings-in-law have never failed to lend an ear and share a laugh when needed. While my Uncle Ed has now on two occasions provided me with first-class accommodations in sunny CA.

A friend once thanked her computer for all the years of faithful service, and I would like to say the same for my computer runjun. Sadly though runjun has been living up to the meaning of the name (Hindi for the sound that thunder makes) and has been replaced just last week with a *new* runjun.

It is funny how a small and utterly helpless human can completely change your perspective on life (or at least reign in some bad habits). I thank my son Neel for truly being my new motivating factor.

Saving the best for last, I am indebted forever to my wife Natasha. Through the course of our relationship she has pushed me to be the best that I can, and I cannot envision arriving at this point without her.

Contents

List of Figures

List of Tables

Chapter 1

Introduction

As Richard Feynman once said "there is plenty of room at the bottom"[1]. Even though this statement is more than forty-five years old, it seems more applicable now than ever as we have the ability to manipulate individual atoms and molecules to fabricate increasingly complicated devices from the "bottom-up". In the bottom-up approach materials are constructed into devices through methods such as self-assembly (and in extreme cases the manipulation of single atoms). On the other hand, the "top-down" approach is the mainstay of the microprocessor industry. In this methodology the transistors and interconnects are patterned onto the semiconductor through a series of lithography steps. One of the driving forces to move to the bottom-up is that this type of top-down methodology and the resulting devices are reaching their fundamental design limits: Si-based transistor scalability, performance, and power dissipation [2]. However, economically and scientifically we would like to continue on a trend similar to Moore's Law.[1] Continued advancement in electronic devices that parallels this trend will require "new technologies based in non-traditional routes"[2].

One such new technology and route is the bottom-up design of molecular scale

[1]Moore's law is an empirical observation stating that the complexity of an integrated circuit, with respect to cost will double roughly every two years(Electronics Magazine 19 April, 1965)

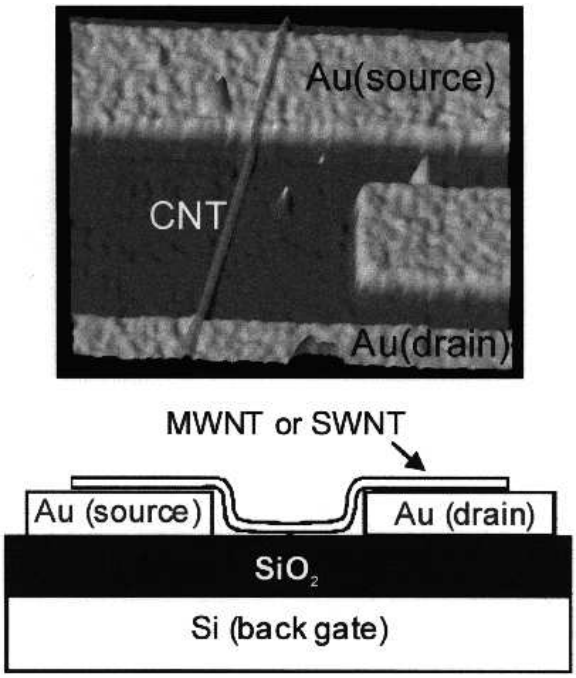

Figure 1.1: An example of a bottom-up design of a molecular scale electronic device: A back-gated carbon nanotube field effect transistor (CNTFET)[5]

.

devices. There are already laboratory examples of many devices at this scale, such as; single molecule conductors across break junctions [3], single carbon nanotube field effect transistors [4], as well as others based on inorganic nanocrystals or molecular components [2]. Figure 1.1 shows a back-gated carbon nanotube field effect transistor (CNTFET)[5]. However, when comparing such devices to the current Si-technology, fundamental problems, other than cost, arise, such as the inability to accurately control on-current voltages of transistor devices [4], or the fact that all semi-conducting nanotubes that are synthesized display p-type semiconductor characteristics in air [4].

Resolving the aforementioned issues in molecular scale devices requires elucidation of their fundamental electronic properties. Investigating what controls properties such as work function, surface energy, charge transfer, and Schottky barrier height at the molecular level will assist in engineering devices with the desired properties. However, from an experimental prospective, the economic cost involved with investigation of

properties at this scale for non-traditional materials sets can be prohibitive.

With the advances made in electronic structure theory and relatively cheap computational power, we now have the tools to investigate such fundamental properties of materials, where we can probe device characteristics from first principles.

1.1 Overview

We begin with a chapter that briefly introduces first principles calculations is presented, Chapter 2. This chapter focuses specifically on the development of density functional theory (DFT) and the manner at which it is used for the studies presented here.

The four chapters that follow are the application of DFT to solving a real materials science problem – the molecular - Schottky junction. The lay out of these chapters is such that we first investigate the constituent parts of the junction – i.e. molecules and charge transfer (Chapter 3), metal surfaces (Chapter 4), carbon nanotubes and electrostatic corrections (Chapter 5). Followed by a study of the Schottky barrier heights in a CNT-metal junction (Chapter 6). Each of these chapters is structured as an individual study; including short introduction, any additional methodological considerations, and results and discussion.

Chapter 2

First Principles Methodologies

2.1 Introduction

The development of quantum mechanics has opened many routes to studying materials with theoretical and truly *ab initio* tools. One of the core tenants of quantum mechanics is the description of particles as waves through a wave function, $\psi(\mathbf{r}, t)$. Knowledge of this function for the ground state of a system is all that is needed to predict many ground state physical observables of the system. The wave function is a solution to the wave equation known as the Schödinger equation:

$$\left[-\frac{\hbar^2}{2m}\nabla^2(\mathbf{r}) + V(\mathbf{r})\right]\psi(\mathbf{r}, t) = i\hbar\frac{\partial}{\partial t}\psi(\mathbf{r}, t). \tag{2.1}$$

While this equation is thought to hold true for any system, solving for $\psi(\mathbf{r}, t)$ is not feasible in most cases. This difficulty leads to the use of many approximations, the combination of which allow for the study of materials science from first principles. These approximations and theories are outlined further in this chapter.

2.1.1 Time Independence

We are generally only concerned with the time-independent form Eqn. 2.1, through separation of variables into a spatially dependent part and a temporally dependent part. We are left with the time independent equation, as an eigenvalue equation:

$$\hat{H}\Psi(\mathbf{r_1}, ..., \mathbf{r_N}) = E\Psi(\mathbf{r_1}, ..., \mathbf{r_N}), \tag{2.2}$$

where $\Psi(\mathbf{r_1}, ..., \mathbf{r_N})$ is now the many-body time-independent wave function, $\hat{H}$ is the Hamiltonian operator, and E is the energy eigenvalue for the corresponding eigenvector $\Psi(\mathbf{r_1}, ..., \mathbf{r_N})$. However, we are still working under the assumption that all parts of the system need to be described by a wave function. The relatively large difference in mass between the proton and the the electron (≈ 1800 times) leads to a decoupling of the electronic and ionic states called the Born-Oppenheimer approximation. Thus the nuclei (herein called the ions) are taken as stationary and we only solve for the wave function of the electrons, the electronic wave function.

Thus our Hamiltonian operator for Eqn. 2.2 can be expressed as:

$$\hat{H} = \hat{T}_e + \hat{V}_{ne} + \hat{V}_{ee}, \tag{2.3}$$

where the Hamiltonian is constructed of a kinetic energy operator,[1]

$$\hat{T}_e = -\frac{1}{2}\sum_i \nabla^2, \tag{2.4}$$

a potential energy operator for the ion-electron interactions

$$\hat{V}_{ne} = -\sum_i \sum_I \frac{Z_I}{|\mathbf{r_i} - \mathbf{R_I}|}, \tag{2.5}$$

where Z_I is the charge of the I^{th} ion, $\mathbf{r_i}$ and $\mathbf{R_I}$ are the positions of the i^{th} electron

[1] Atomic units are used here, where: $\hbar = m_e = 4\pi\epsilon_0 = 1$

and I^{th} ion, respectively, and a potential energy operator for the electron-electron interactions

$$\hat{V}_{ee} = \frac{1}{2}\sum_{i \neq j} \frac{1}{|\mathbf{r_i} - \mathbf{r_j}|}. \tag{2.6}$$

Within the Born-Oppenheimer approximation the nucleus-nucleus interaction enters the equation, only dependent on the interaction of the nuclei,

$$V_{nn} = \frac{1}{2}\sum_{I \neq J} \frac{Z_I Z_J}{|\mathbf{R_I} - \mathbf{R_J}|}. \tag{2.7}$$

The total energy of the system, W, is thus found by solving Eqn. 2.2 for the electronic ground state energy, E, and the ground state many-body wave function $\Psi(\mathbf{r_1}, ..., \mathbf{r_N})$ and adding the nucleus-nucleus energy term:

$$W = E + V_{nn} \tag{2.8}$$

As mentioned earlier, in principle all of the ground-state physical properties of a system can be calculated from the ground-state wave function and we see we know exactly the equation and exactly how to solve it in order to obtain the wave function. However, even in the time-independent regime, the electronic Schrödinger equation is an intractable many-body problem for systems greater than a few particles.[2] Because of this intractability, great effort has gone into finding alternative approaches and approximations.

There are many texts on the subject, and the reader is directed towards the books of Parr and Yang [6], Szabo and Ostlund [7], and R. Martin [8] for more in depth study. We focus here on the breakthroughs of density functional theory, where the electron density is used as the variable that uniquely defines the ground state wave function. The remainder of this chapter discusses the central theorems of density functional

[2]For even a small system of 20 electrons on a conservative numerical grid of $10 \times 10 \times 10$, 10^{60} points would need to be solved for.

theory followed by a discussion of the current implementation of the theories used throughout this thesis.

2.2 Density Functional Theory

In brief, density-functional theory attempts to solve the many-body problem by re-casting the time-independent Schrödinger equation seen in the previous section as a functional of one variable, the charge density $n(\mathbf{r})$. A notable attempt to do this early on was by Thomas and Fermi, where the entire equation is solved as a function of the electron density. The Thomas-Fermi energy functional is:

$$E^{TF}[n(\mathbf{r})] = \int \frac{3}{10}(3\pi^2)^{2/3} n^{5/3}(\mathbf{r}) + \int v(\mathbf{r}) n(\mathbf{r}) d\mathbf{r} + \frac{1}{2}\int \frac{n(\mathbf{r})n(\mathbf{r}')}{|\mathbf{r}-\mathbf{r}'|} d\mathbf{r} d\mathbf{r}', \tag{2.9}$$

The first term is the kinetic energy obtained through integrating of the kinetic energy of the homogeneous electron gas. The ground state energy is found by minimizing Eqn. 2.9 with the constraint that

$$\int d^3\mathbf{r} n(\mathbf{r}) = N, \tag{2.10}$$

where N is the number of electrons. However the TF method can miss crucial chemistry, such as binding. It wasn't until the rigorous proofs of Hohenberg and Kohn [9] followed by the formulation of Kohn and Sham [10] that we see DFT as we know it today.

2.2.1 Hohenberg-Kohn Theorems

The first Hohenberg and Kohn theorem proved that the ground state density can be used as the basic variable. That is for a system of interacting particles under an external potential $v(\mathbf{r})$, $v(\mathbf{r})$ is a unique functional of the ground state density $n(\mathbf{r})$, implying that once the external potential $v(\mathbf{r})$ is determined so is the ground state

density for that potential, and thus the ground state is a unique functional of the the density [9].

The second Hohenberg and Kohn theorem proved that solving for the ground state wave function of the time independent many-body problem with the density as the basic variable is a variational problem. The ground state energy functional is comprised of a universal functional and a $v(\mathbf{r})$ dependent term. The universal functional, $F[n(\mathbf{r})]$, is independent of $v(\mathbf{r})$:

$$F[n(\mathbf{r})] \equiv \langle \Psi | \hat{T}_e + \hat{V}_{ee} | \Psi \rangle, \tag{2.11}$$

where $\hat{T}_e$ and $\hat{V}_{ee}$, the kinetic energy and electron-electron interaction, respectively, are functionals of only the charge density. the ground state energy functional is written as

$$E[n(\mathbf{r})] \equiv F[n(\mathbf{r})] + \int v(\mathbf{r}) n(\mathbf{r}) d\mathbf{r} \tag{2.12}$$

Thus the ground state energy, E_0, for any given potential is at its minimum for the ground state charge density $n(\mathbf{r})$ and always greater than that for any arbitrary density that is not the ground state, $\tilde{n}(\mathbf{r})$.

$$E_0 = E[n(\mathbf{r})] \leq E[\tilde{n}(\mathbf{r})] \tag{2.13}$$

However simple minimization of the functional to determine the ground state is not possible because no exact solution to the universal functional $F[n(\mathbf{r})]$ is currently known.

2.2.2 Kohn-Sham Theory

Kohn and Sham proposed approximating the universal functional, $F[n(\mathbf{r})]$, through a mapping of the many-electron problem to one of a non-interacting single-electron [10].

The non-interacting system's wave function Ψ is expressed as a Slater determinant,

$$\Psi = \frac{1}{\sqrt{N!}} \det[\psi_1, ..., \psi_N] \tag{2.14}$$

and the charge density given by

$$n(\mathbf{r}) = \sum_{i}^{N} |\psi_i(\mathbf{r})|^2. \tag{2.15}$$

We then have the Kohn-Sham eigenvalue equation, which can be solved for self-consistently to obtain the single particle Kohn-Sham wave functions and thus the charge density.

$$\left[-\frac{1}{2}\nabla^2 + v_{KS}\right] \psi_i(\mathbf{r}) = \epsilon_i \psi_i(\mathbf{r}) \tag{2.16}$$

The final form of the ground state energy can be expressed as the energy functional, which consists of the kinetic energy $T[\psi_i]$, Hartree energy $E_H[n(\mathbf{r})]$, exchange-correlation energy terms $E_{xc}[n(\mathbf{r})]$, and the external potential:

$$E[\{\psi_i\}] = T[\psi_i] + E_H[n(\mathbf{r})] + E_{xc}[n(\mathbf{r})] + \int v(\mathbf{r}) n(\mathbf{r}) d\mathbf{r} \tag{2.17}$$

The non-interacting kinetic energy term T is given by

$$T[\psi_i] = -\frac{1}{2} \sum_i \int \psi_i^*(\mathbf{r}) \nabla^2 \psi_i(\mathbf{r}) d\mathbf{r}, \tag{2.18}$$

and the Hartree potential is:

$$E_H[n(\mathbf{r})] = \frac{1}{2} \int \frac{n(\mathbf{r}) n(\mathbf{r}')}{|\mathbf{r} - \mathbf{r}'|} \tag{2.19}$$

The E_{XC} can be thought to capture all of the remaining complex contributions. the contributing factors can be seen by equating the ground state energy (with the universal functional) in Eqn. 2.12 with the energy functional in Eqn. 2.17 and solving

for E_{XC}:

$$E_{XC} = F[n(\mathbf{r})] - (T[\psi_i] + E_H[n(\mathbf{r})]), \tag{2.20}$$

which, when expanded further, reveals that the exchange correlation is a combination of the difference in the kinetic energies of the many-body and non-interacting systems as well as the non-classical part of the electron-electron interaction.

Finally, the effective potential, or the Kohn-Sham potential v_{KS} is thus:

$$v_{KS} \equiv v(\mathbf{r}) + v_H(\mathbf{r}) + v_{xc}(\mathbf{r}) \equiv v(\mathbf{r}) + \int \frac{n(\mathbf{r}')}{|\mathbf{r} - \mathbf{r}'|} d\mathbf{r}' + \frac{\delta E_{xc}[n(\mathbf{r})]}{\delta n(\mathbf{r})} \tag{2.21}$$

The main approximation enters in the choice of an exchange-correlation functional, $E_{xc}[n(\mathbf{r})]$.

2.2.3 Exchange-Correlation Functionals

No exact form for the exchange-correlation function is currently known, thus DFT relies on approximations. The local density approximation (LDA) suggested by Kohn and Sham [10] is still widely used. The form of the LDA functional is:

$$E_{XC}^{LDA} = \int n(\mathbf{r}) \epsilon_{XC}(n(\mathbf{r})) d(\mathbf{r}) \tag{2.22}$$

The exchange correlation energy is taken as that of the uniform electron gas of the same density, where $\epsilon_{XC}(n(\mathbf{r}))$ is the exchange and correlation energy of a uniform electron gas of density n. In principle this approximation only applies to regions where the density is slowly varying, and in practice it has been useful for extended metallic systems, and is applied later in this thesis.

Refinement to the exchange-correlation functional that incorporate the effects of first order changes in the density are known as generalized gradient approximations (GGAs). GGAs are still local, but they take into account gradients in the density

$\nabla n(\mathbf{r})$:

$$E_{XC}^{GGA} = \int d^3\mathbf{r} f(n(\mathbf{r}), \nabla n(\mathbf{r})). \tag{2.23}$$

There are a number of different formulations of GGAs. The one employed later in this thesis is that of Perdew, Burke, and Ernzerhof (known as PBE) [11].

Higher order gradient corrections ($\nabla\nabla n, \nabla\nabla\nabla n$, etc.) can be applied, and are known as meta-GGAs. However, currently the computational cost outweigh any possible numerical gains.

2.3 DFT Implementation

DFT can be implemented in a number of ways, however, the following section describes how it is implemented for the manner in which it is and will be utilized for this thesis; namely the use of periodic boundary conditions, plane-wave basis sets, and pseudopotentials. The implementation used here is available under the GNU-public license as quantum-ESPRESSO [12].

2.3.1 Plane-waves and Periodic Boundary Conditions

A popular manner in which DFT is implemented utilizes plane-wave basis sets and periodic boundary conditions (PBCs). Through use of the Bloch's theorem, calculation of the total energy of a system with a periodic potential, $v(\mathbf{r}) = v(\mathbf{r} + \mathbf{R})$, becomes tractable. The wave function in Bloch's theorem becomes the product of a wave-like part, $e^{i\mathbf{k}\cdot\mathbf{r}}$ and a periodic part $u_{n\mathbf{k}}(\mathbf{r})$:

$$\psi_{n\mathbf{k}}(\mathbf{r}) = e^{i\mathbf{k}\cdot\mathbf{r}} u_{n\mathbf{k}}(\mathbf{r}), \tag{2.24}$$

where n is the band index, and $\mathbf{k}$ is the reciprocal lattice vector. Expanding the periodic part using plane-waves, we have:

$$u_{n\mathbf{k}}(\mathbf{r}) = \sum_{\mathbf{G}} c_{i,\mathbf{G}} e^{i\mathbf{G}\cdot\mathbf{r}} \tag{2.25}$$

and thus each electronic wave function can be written as a sum of plane-waves

$$\psi_{n\mathbf{k}}(\mathbf{r}) = \sum_{\mathbf{G}} c_{i,\mathbf{k}+\mathbf{G}} e^{i(\mathbf{k}+\mathbf{G})\cdot\mathbf{r}} \tag{2.26}$$

While in principle an infinite number of plane-waves would be necessary to expand the wave function at each $\mathbf{k}$-point, in practice only the small kinetic energy terms are important. Thus an energy cutoff can be imposed on the plane waves such that $|\mathbf{k}+\mathbf{G}|^2 < E_{cut}$. This ability to systematically increase or decrease the accuracy of the basis set is one of the advantages of plane-waves, others being that they are not atomic species specific and they span the entire space of the unit cell (which can also be a disadvantage if large areas of vacuum are included in the unit cell).

2.3.2 Pseudopotentials

Typically only the outermost, or valence, electrons are involved in the interaction we are interested in studying – i.e. bonding and scattering – thus, a method that only addresses these electrons explicitly and incorporates the core electrons into the ionic potential can be used. Pseudopotentials group the core electrons with the ionic core of the atom in an effort to smooth out the many nodes of the atomic wave function and make them and the potential more easily representable (especially with plane waves).

The two main classifications of pseudopotentials are norm-conserving and ultrasoft. The norm-conservation maintains that the integral of the squared amplitude of the real and pseudo wave functions are equal, while ultrasoft potentials relax this restriction in the hopes that a cheaper – i.e. lower E_{cut} – pseudopotential can be

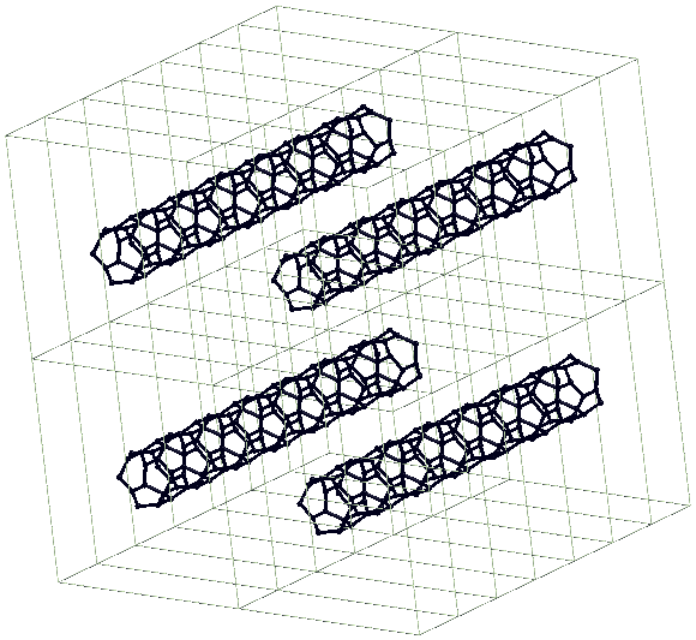

Figure 2.1: Representation of a super-cell constructed for and isolated (5,0) carbon nanotube. Shown here is the unit-cell repeated $2 \times 2 \times 7$ times to illustrate the use of the vacuum region to isolate the nanotube.

found. Throughout this thesis, ultrasoft pseudopotentials are typically used.

2.3.3 Super-cells

In order to describe a system that is finite in any direction within periodic boundary conditions – e.g. a molecule or a nanotube – a region of vacuum must be inserted in between periodic images. Care must be taken in creating such super-cells that the vacuum region is large enough that there are no interactions with images. It is typically enough to make sure that the images do not have overlapping densities, however, electrostatic interactions are long ranged, thus for cells that have charges and/or dipoles other methods (discussed in Chapter 5) need to be used. The construction of a super-cell for the study of a (5,0) CNT can be seen in Figure 2.1, here

four of the repeated tubes are shown to illustrate the inclusion of the vacuum region.

Further information on the nature of the implementation of DFT in codes such as quantum-ESPRESSO is summarized in the paper of Payne, *et al.* [13].

Chapter 3

Conjugated Polymers

3.1 Introduction

π-conjugated polymers have received considerable attention since their introduction decades ago [14]. Due to their conductive properties that can be controlled by doping, these polymers have seen applications as conductors and semiconductors [14] with many notable examples in optoelectronics[15, 16], electronic devices [17, 18], and as components in molecular scale actuators [19, 20, 21, 22, 23, 24]. With respect to electronics, the interactions of charged oligomers, in particular π-stacking, could prove useful to the bottom-up assembly of molecular scale devices. Figure 3.1 shows one example of such an actuator. This actuator consists of a flexible calixarene hinge and rigid conjugated oligothiophenes. The actuation in this case it driven by the π-stacking of the oligothiophene when charged. It is this stacking that this study is most concerned with. This study explores the effects that the common counterion hexafluorophosphate, PF_6^-, has on charged oligothiophene systems with quantum chemistry techniques, discussed in the following section. In addition, we study the properties of the individual molecular species (electron affinities and ionization potentials), the charge transfer and binding properties of singly-charged oligothiophene monomers, and the binding interactions within doubly-charged, dimerized oligothiophenes. Pub-

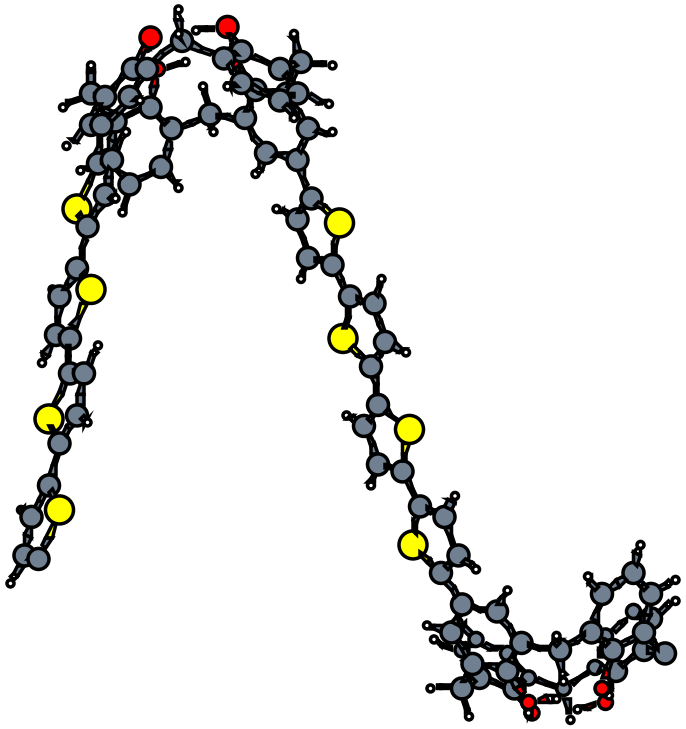

Figure 3.1: A molecular actuator consisting of flexible calixarene hinges and rigid oligothiophenes. actuation is driven through a π-stacking interaction between the charged oligothiophenes.

lished details of this study can be found in Ref. [25], but are given in more detail in the following sections.

It has been shown previously experimentally [26] and theoretically [27, 28, 29] that when oligothiophenes are oxidized they will dimerize through π-stacking. The interaction takes place between two positively charged planar oligomers, where the strong tendency of the charged oligomers to repel each other via Coulomb interactions is overcome by π-bond hybridization and by solvation effects (such as polarization and screening of the surrounding dielectric medium and surface tension of the solvent [20]). Although dimerization of conjugated oligothiophenes occurs when the oligomers are charged, it has not been common practice to explicitly describe the counterions in the electronic structure calculations. In reality, charge compensating counterions will be necessarily present.

Functionality aside, questions still remain about the overall effect that counterions have on π-conjugated systems. Few studies, experimental[30, 31] or theoretical[32, 33], have focused on these effects with respect to conjugated polymers. It is expected that, beyond charge compensation, the counterion may affect the structure and electrostatic properties of these π-conjugated systems.

3.2 Methodology

The density functional theory methodologies used within this chapter represent a slight deviation for that described in Chapter 2. Specifically, the isolated molecular systems studied here lend themselves to be best described by localized basis sets. To that end we use here the commercial code package Gaussian03 [34]. Furthermore, we use the solvation methodologies implemented within Gaussian03. Localized basis-sets and solvation are briefly discussed in the next sections.

3.2.1 Localized Basis Sets

As previously mentioned, the isolated nature of the molecules in this study (i.e. no translational symmetry) leads to the choice of localized basis sets.[1] Localized basis sets are broken into two types of basis function; either Slater Type Orbitals (STO) or Gaussian Type Orbitals (GTO).

The Slater type orbital are of the form:

$$\chi_{\zeta,n,l,m}(r,\theta,\varphi) = NY_{l,m}(\theta,\varphi)r^{(n-1)}e^{-\zeta r}, \tag{3.1}$$

where $Y_{l,m}$ are the spherical harmonic functions and N is a normalization constant.

[1] In all of the other included in this thesis we work within periodic boundary condition and use plane-wave basis sets as outlined in Chapter 2.

While, the Gaussian type orbitals can be written as

$$\chi_{\zeta,n,l,m}(r,\theta,\varphi) = NY_{l,m}(\theta,\varphi)r^{(2n-2-1)}e^{-\zeta r^2}. \tag{3.2}$$

In general neither are solutions to an atomic Schrödinger equation and the r^2 dependence of the exponential of the GTO makes the STO a better choice. The GTO has problems representing the behavior near the nucleus due to tails that fall off too rapidly. However, both can be chosen to construct a complete basis set, and the general rule of thumb is that three times as many GTOs are needed [35].

In this study we are using a basis set built on the STOs and GTOs, and we outline here the specific basis sets used. However, there is a wealth of localized basis sets that are beyond the scope of this thesis, for reference see Ref. [35].

Contraction and Pople Style Basis Sets

The need for basis set contraction arises because the energy optimization is dominated by the inner core wave functions, which are typically chemically less interesting. The contraction is executed by making the variational constants of the inner basis functions constant. Contracted GTOs (CGTO) are thus fixed linear combinations of primitive GTOs (PGTO)

$$\chi(CGTO) = \sum_{i}^{k} a_i \chi_i(PGTO). \tag{3.3}$$

The Pople style basis sets are constructed of PGTOs, the exponents of which are determined by fitting to the STO. The basis set used here is the *6-311G*. The core orbitals are a contraction of six PGTOs and the valence is represented by three, one, and one PGTOs. In this basis set nomenclature the G is meant to indicate Gaussian type.

Furthermore, diffuse and polarization functions can be added to the basis set. These are s- and p-functions added to the basis, and are indicated by + or ++. The

first plus is for the diffuse functions of heavy atoms and the second is for diffuse s-functions for hydrogen. The basis set used here becomes *6-311+G* or *6-311++G* with diffuse functions. Polarization functions can be added as extra p-, d-, and f-functions. These functions are indicated as *6-311++G(d,p)* for instance.

3.2.2 Solvation

Most chemistry takes place in the presence of a solvent. However, explicitly including solvent molecules to a calculation is computationally impractical.[2] Thus, methodology exists to add a solvent as an dielectric background, with the main focus on the the static dielectric constant of the solvent. We use here a method called the polarized continuum model (PCM) for solvation.

The PCM model employs a cavity of interlocking van der Waals spheres centered at each atomic position. The solvation free energy is written as [35]:

$$\Delta G_{\text{solvation}} = \Delta G_{\text{cavitation}} + \Delta G_{\text{dispersion}} + \Delta G_{\text{electrostatic}} \tag{3.4}$$

The main choice comes in that of the dielectric constant of the solvation medium. This is then subsequently used to solve for the screened electrostatic interactions projected onto the cavity surfaces.

3.3 Counterions

This section contains the results and discussion of a study of the effects of counterions on the π-stacking of oligothiophenes [25] and is divided into three parts. First, the electronic properties of the individual hexafluorophosphate and oligothiophene ions are addressed, including electron affinities and ionization potentials. Second, the

[2]This is especially true for wave-function methods such as this that often scale much worse than $O(N^3)$ with system size.

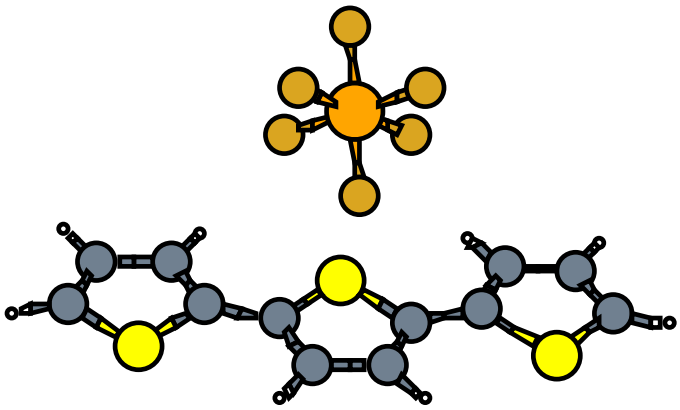

Figure 3.2: The counterion studied here, PF_6 with a oligothiophene (terthiophene in this case).

Table 3.1: Ionization potentials of the different oligothiophenes considered in vacuum, dichloromethane (DCM), acetonitrile (ACN), and water. Units are kcal/mol.

	thiophene		bithiophene		terthiophene		quarterthiophene	
	B3LYP	PBE	B3LYP	PBE	B3LYP	PBE	B3LYP	PBE
Vacuum	206.2	205.2	173.9	171.1	159.3	155.4	150.8	146.4
DCM	156.1	155.3	134.4	132.8	125.7	122.2	121.3	117.3
ACN	151.4	150.6	130.5	129.1	122.6	119.2	118.4	114.3
Water	150.5	149.7	130.4	127.3	121.8	118.4	117.6	113.6

interaction between PF_6^- and an oligothiophene monomer is investigated, including charge-transfer effects and binding energies. Finally, we examine the interactions between charged dimerized oligothiophenes in the presence of PF_6^-, and the role of the counterion in driving dimerization and structural stability. In all cases, the effects of different solvents are investigated in detail for clarity.

Properties of the Individual Molecules

The structure of PF_6 and of several oligothiophenes (from monothiophene to quarterthiophene) were determined in both the neutral and charged states (anion for PF_6 and cation for the oligothiophenes), together with the electron affinity of PF_6 and the ionization potentials of the oligothiophenes. Tables 3.1 and 3.2 contain the adiabatic ionization potentials (IPs) and electron affinities (EAs, respectively, both at the

Table 3.2: Electron affinities of PF_6 in vacuum, dichloromethane (DCM), acetonitrile (ACN), and water. Units are kcal/mol.

	PF_6	
	B3LYP	PBE
Vacuum	-187.3	-162.1
DCM	-235.2	-211.1
ACN	-239.8	-215.8
Water	-240.4	-216.5

B3LYP and PBE level. These values have been obtained subtracting from the total energy of the charged system in the neutral geometry the total energy of the neutral system. For the systems in solution non-electrostatic terms (cavitation, dispersion, and repulsion energies) are also included.

Experimental data[36] are available for terthiophene, and reasonable agreement is found: 143 kcal/mol versus the calculated 155.4 kcal/mol (PBE) and 159.3 kcal/mol (B3LYP). A decrease in the IP accompanying the increase in oligomer length is observed in vacuum and in all solvents, which is consistent with experimental[18] values for polythiophene (115 kcal/mol) and with a hybrid-functional calculation[37] (126 kcal/mol). While the IPs obtained with the two levels of theory are quantitatively similar, for EAs the discrepancies are far larger. This is somewhat expected as it is well-known that local or semi-local exchange-correlation functionals under-bind negative ions[38, 39] which leads to lower EAs (as it is seen here for the PBE case).

Monomer-Counterion Interactions

A system including a positively-charged oligothiophene and a negatively-charged counterion is electrically neutral. We thus evaluated the tendency for charge transfer between a single oligothiophene and a single counterion keeping the overall system neutral. From the electron affinities and the ionization potentials found in ables 3.1 and 3.2, both B3LYP and PBE simulations should exhibit spontaneous charge transfer between the molecules for all cases considered, except for thiophenes or bithiophenes

Table 3.3: Charge transfer energies for terthiophene-PF_6^-, calculated with B3LYP and PBE, units in kcal/mol.

	5Å separation		10Å separation		IP+EA	
	B3LYP	PBE	B3LYP	PBE	B3LYP	PBE
Vacuum	-77.7	-59.5	-56.5	+15.7	-28.0	-6.7
DCM	-108.8	-88.8	-112.3	-91.6	-109.5	-88.9
ACN	-113.4	-93.7	-117.6	-96.9	-117.2	-96.6
Water	-113.5	-93.6	-118.6	-98.1	-118.6	-98.1

in vacuum. To illustrate this point, we studied the energy involved in this charge transfer as a function of the separation, using terthiophene and a PF_6^- counterion. The results for 5Å and 10Å of separation and for all solvents are summarized in Table 3.3, where we report the total energy for the neutral system (terthiophene and counterion) minus the total energy of an isolated neutral terthiophene and an isolated neutral PF_6 (as usual for solvation studies, the non-electrostatic energy terms are also included). Charge transfer is always observed in our calculations, with the exception of the system in vacuum, for the two species 10Å apart, and when using PBE. This failure, reflected in the Mulliken populations, is discussed in more detail later in this section.

For the solvated cases, as expected, the sum of the IP and EA are in excellent agreement with the energy associated to charge transfer at large separations (columns 3 and 2 of Table 3.3, respectively), due to the screening of the long range Coulomb interactions by the dielectric medium, already very effective at a distance of 10Å. In vacuum, instead, the charge-transfer energy at 10Å is not yet converged to this same asymptotic limit due to the long-range electrostatics.

The dependence of the binding energy of the counterion to the charged terthiophene was also calculated. The counterion was moved normal to the plane of the terthiophene with the central sulfur of the terthiophene on the same axis of the phosphorous of the hexafluorophosphate. The equilibrium geometries determined for the individual charged molecules were used here. We show in Figure 3.3 the binding en-

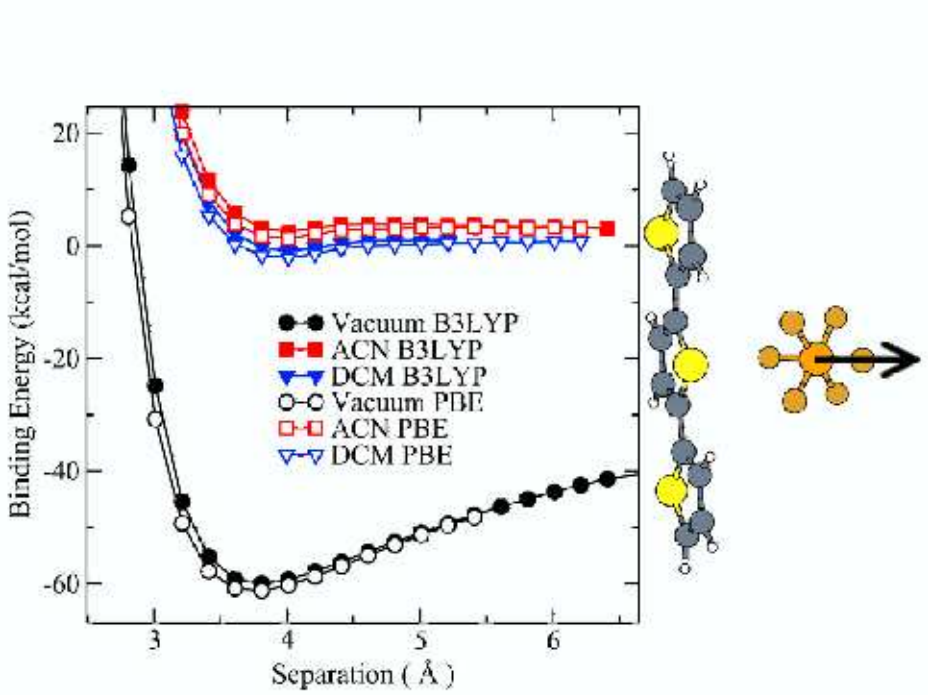

Figure 3.3: Interaction energy for the terthiophene cation and the PF_6^- anion as a function of separation, in vacuum (circles), acetonitrile (squares), and dichloromethane (triangles), using B3LYP (solid) and PBE (hollow). The direction of separation is shown schematically.

ergy for this system as a function of separation, in different solvents. As expected, in vacuum there is a strong interaction between the molecules (60 kcal/mol) due to the Coulomb attraction between them. However, in the polarizable solvents (acetonitrile and dichloromethane) the attraction is highly screened by the dielectric medium.

We found that for separations greater than 5.4Å convergence of the total energy was not easily achieved when studying this system in vacuum using PBE. Furthermore, when converged, the energy values were much higher than the B3LYP calculations, with a discontinuity at 5.4Å. The Mulliken charges were investigated: when charge transfer occurs, they sum to approximately -1 on PF_6^- and +1 on the terthiophene. We show in Figure 3.4 a plot of the sum of the Mulliken charge for PF_6 as a function of separation. Beyond 5.4Å the self-consistent algorithm is not able to

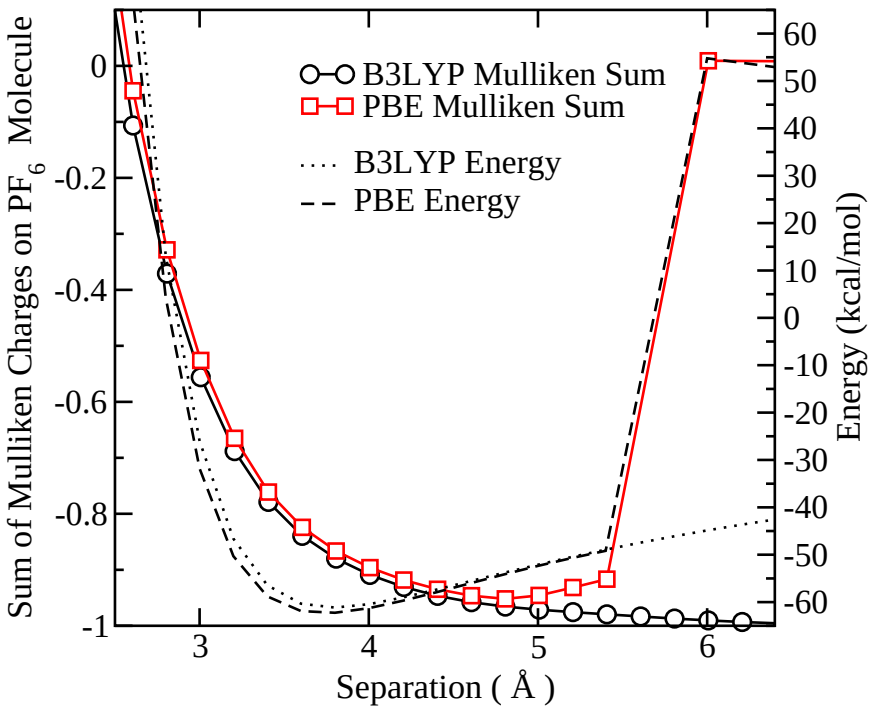

Figure 3.4: Mulliken charges for PF_6^- as a function of distance from the terthiophene cation, for B3LYP and PBE. A value of -1 corresponds to a full charge transfer. The binding energy is also overlaid.

converge to the correct charge transfer ground state. Regardless of this failure, both functionals PBE and B3LYP were used for the remainder of this study, due to the fact that the separations between the oligomer and counterion were always close to the equilibrium separations of 3.7 to 3.8Å.

Last, the potential energy surface was calculated for PF_6^- in the presence of a charged terthiophene (again, an overall neutral system), using a plane-wave periodic boundary code discussed in Chapter 2 This mapping required 63 separate ionic relaxations across the terthiophene plane using a 1Å $\times$ 1Å grid, as illustrated in Figure 5.5. The 63 points comprise one half of the system, exploiting the mirror symmetry orthogonal to the molecular plane (the 6Å line on the horizontal axis in Figure 5.5). During each relaxation the sulfur atoms of the terthiophene were held fixed, the carbon atoms held in a plane (i.e. at a fixed height), and the phosphorus atom of the hexafluorophosphate was restricted in its movement to the axis perpendicular to the

plane of the terthiophene (however, the fluorine atoms of the molecule were given no restriction in any direction). In this manner the counterion relaxes to its geometric minimum for each grid point without displacing the terthiophene. The potential energy surface is shown in Figure 5.5: most notably, it is found to be quite shallow with respect to any given point, with a difference between the global minimum and maximum of only 8.4 kcal/mol. The most favorable location for the counterion is that on the side of the terthiophene adjacent to the central sulfur atom on the chain. The location of the global minimum is further refined by full relaxations using B3LYP in both vacuum and acetonitrile: the counterion in vacuum is found slightly out of plane (0.37Å and 3.76Å away from the central sulfur, while for acetonitrile it remains in the plane, 4.24Å away from the central sulfur atom. These minima are marked in Figure 5.5 and the one structural minimum found for PF_6^- in vacuum will be later used to determine the potential energy surface of doubly-charged terthiophene dimers in the presence of two counterions.

Dimer-Counterion Interactions

The interaction between two charged terthiophenes in the presence of two PF_6^- counterions was investigated. The dimerized assembly consists of two singly-charged terthiophenes and two counterions. As before, this is overall a neutral system, and spontaneous charge transfer within the system leads to positively-charged terthiophenes and negatively-charged hexafluorophosphate ions. The PF_6^- counterions are located on opposite sides of the dimer (one in line with the central sulfur at the global minimum position, the other in line with an edge sulfur). The terthiophenes are in parallel planes separated by 3.4Å. A sketch of this geometry is shown in Figure 3.6. For this geometry the binding energy of the dimer has been calculated versus the lateral displacement of the two terthiophenes, in vacuum and acetonitrile. Other geometries were also investigated and show quantitatively and qualitatively similar results. Figure 3.6 displays the results for the lateral displacements of oligothiophenes

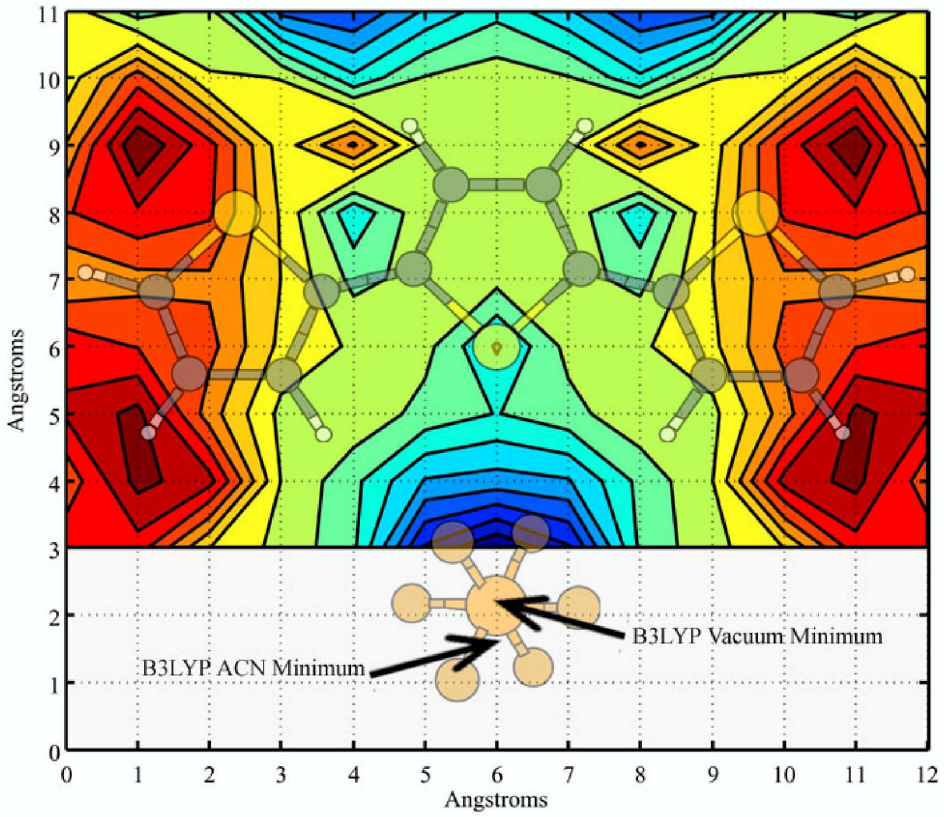

Figure 3.5: PBE potential energy surface for a PF_6^- onto a terthiophene in vacuum. The potential energy difference between the highest point (dark red) and the lowest one (dark blue) is 8.44 kcal/mol. Also shown are the geometry minima obtained with B3LYP in both vacuum and acetonitrile (ACN); these two points were calculated using Gaussian03 and are outside the periodic box of the plane wave calculation. The molecules are schematically overlaid for visual reference.

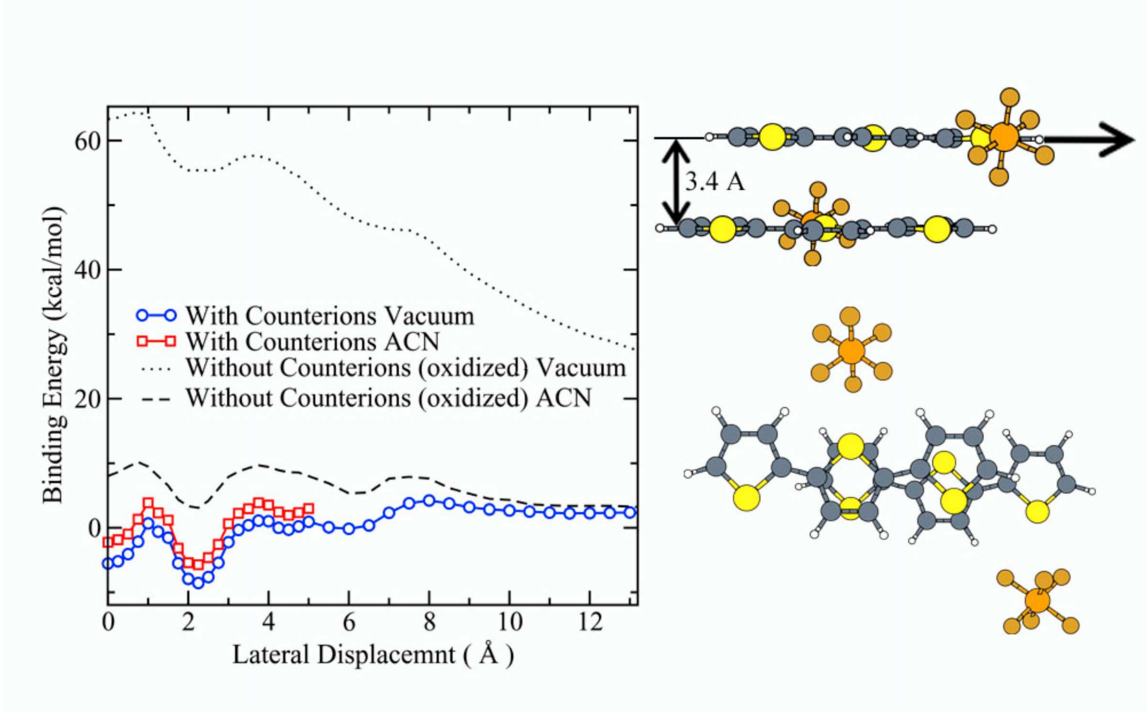

Figure 3.6: Interaction energy versus lateral displacement of the doubly-charged terthiophene dimer in the presence of PF_6^- (PBE), in vacuum and in acetonitrile. The energy of the doubly-charged dimer without counterions is also plotted for comparison (B3LYP). Side and overhead views of the molecular system are shown schematically.

and counterions in vacuum and in acetonitrile. The binding energy values reported here are determined as the total energy of the dimerized system minus the energy of the two constituent systems (singly-charged terthiophene bound to one counterion). For comparison, the binding energy versus lateral displacement of the doubly-charged dimer in the absence of counterions is plotted. For this latter case, a polarizable solvent such as acetonitrile stabilizes the binding of the doubly-charged dimer, in good agreement with a previous study[29] that showed the same effect in the presence of the solvent.

However it is apparent that the presence of counterions further stabilizes the dimerization process. Furthermore, even the counterions alone (i.e. without the solvent) stabilize the dimerized system, and we see that in both cases there exists energy minima in the presence of counterions that are below the limit approached at

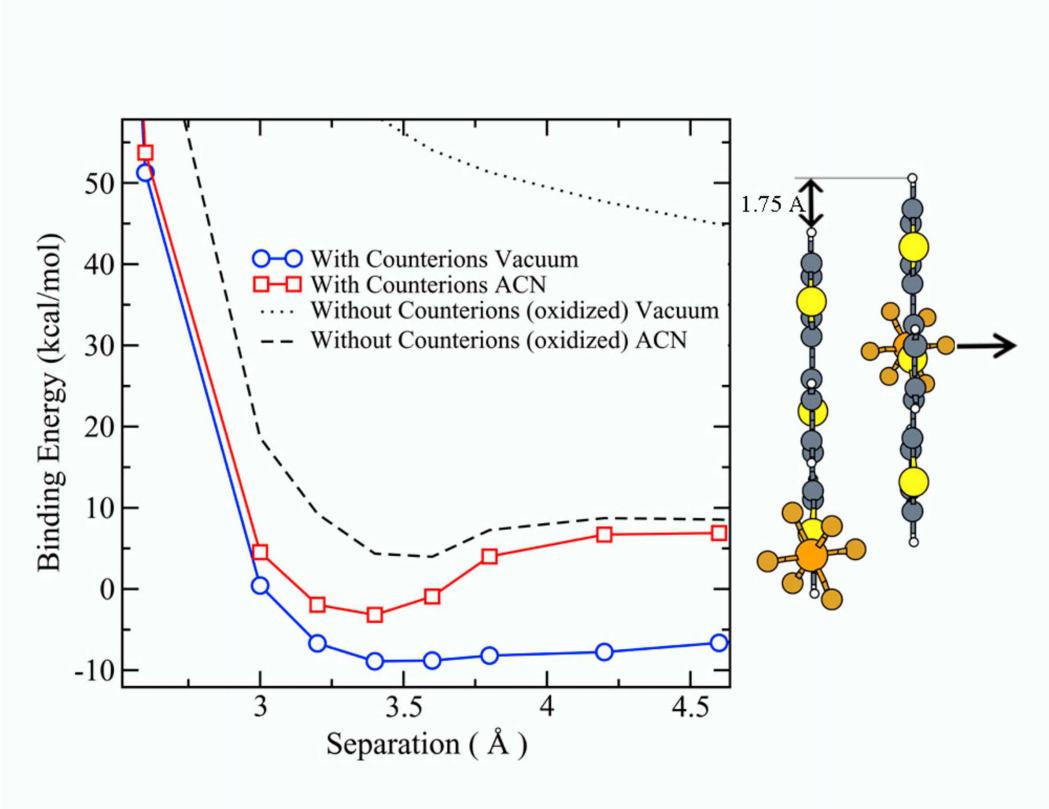

Figure 3.7: Interaction energies versus separation for the doubly-charged terthiophene dimer in vacuum and in acetonitrile (PBE). The energy of the doubly-charged dimer without counterions is also plotted for comparison (B3LYP). A side view of the molecular system is shown schematically.

full lateral separation of the dimer. Note also that the minima in Figure 3.6 correspond to electronic singlet states, which suggests π-bond hybridization, whereas the maxima correspond to triplet states. PBE and B3LYP show that these minima correspond to closed-shell singlets. Previous calculations done in the absence of counterions and using several exchange-correlation functionals have shown similar results[29]; where Hartree-Fock and MP2 calculations have instead predicted for these minima an open-shell singlet configuration, with unpaired electrons of opposite spin localized on each monomer[29] Such discrepancies between DFT and HF-based methods are attributable to the charge-density delocalization associated with the self-interaction error of the exchange-correlation functional. In spite of this disagreement regarding

the nature of the singlet, the interaction energies obtained with MP2, GGA, and multiconfiguration schemes such as CASSCF turn out to be quantitatively close[29]. The maxima along the lateral displacement curve, on the other hand, are triplets corresponding to the two radical fragments exhibiting no chemical bond (note that each charged terthiophene plus the attached counterion has one unpaired electron, and so the total spin arising from two unbound counterion-terthiophene units is a triplet). The presence of the negatively-charged counterions screens the Coulomb repulsion between the positively-charged terthiophenes and ultimately leads to stable π-stacked dimers in both acetonitrile and vacuum.

Finally, the energy of separation for the dimerized assembly in the presence of counterions was calculated. A laterally-displaced geometry in which the terthiophenes are in parallel planes yet displaced by 1.75Å was used for the separation-energy calculations. The geometry used, along with a plot of the binding energy for the dimer in vacuum and acetonitrile are shown in Figure 3.7. Again, for reference a plot of the interaction energy of the doubly-charged dimer in the absence of counterions is included in the same graph. The values reported here are the total energy of the fully dimerized system minus the total energy of the two constituent systems. Once again the presence of the polarizable solvent and the counterions stabilizes the dimerized oligothiophenes. However, for the case with no counterions in ACN the energy at the minimum is found to be positive. This is a slight deviation from the results presented in Reference [29], and can be attributed mainly to the choice of lateral displacement used here (not being the full minimum geometry) as well as the differences in the PCM and iPCM solvation methods. Regardless of this deviation, the results still show that the addition of counterions stabilizes further the π-stacked dimer.

Chapter 4

Metals

4.1 Introduction

Electronic structure calculations are becoming more widely applied to increasingly complex and realistic materials systems and devices, reaching well into the domain of nanotechnology with applications ranging from metal-molecule junctions, carbon-nanotube field effect transistors, and nanostructured metals or semiconductors [40, 41]. For such complex applications, characterizing the properties of the elementary building blocks becomes of fundamental importance. Consider the carbon nanotube field effect transistor: the performance of such a device depends critically on the properties of the metal-nanotube junction [4, 42]. Since Schottky barrier heights are in part governed by Fermi level alignment at the interface, it becomes critical to have a clear understanding of the fundamental properties of the metal lead surfaces – starting from surface energies, structural relaxations, and work functions. For this purpose we proceed here with a detailed study of the properties of clean metal surfaces of interest, as lead materials, to nanotechnological applications, and discuss the issues involved in obtaining converged estimates using electronic-structure modeling - in this case using density-functional theory (DFT) and the slab-supercell approximation - and the accuracy of these estimates compared to experimental values.

First, surface relaxations can arise from the creation of a new surface – i.e. cleaving of a bulk in two. This leads to a smoothing of the charge density at the new surface which causes a net force on the outermost surface layer of ions pointing into the bulk [43]. DFT calculations in the slab-supercell approximation, assuming a pristine unit cell of the unreconstructed surface, can be effectively used to study these surface layer relaxations.

Second, the surface energy is the energy required to cleave an infinite crystal in two – i.e. the amount of energy required to create a new surface. This is a difficult quantity to determine experimentally because it usually requires measuring surface tension at the melting temperature of the metal [44]. Theoretical determination of this quantity is relatively easy. However surface energy calculations within DFT are sensitive to numerical errors arising from differences in Brillouin-zone sampling [45]. Methodologies for avoiding these errors have been proposed in the literature [45, 46, 47] and are discussed in later sections of this study.

Third, the work function is the minimum energy needed to remove an electron from the bulk of a material through a surface to a point outside the material. In practice, this is the energy required at 0 K to remove an electron from the Fermi level of the metal to the vacuum potential [48]. Calculations of work function using DFT employ this definition and determine the Fermi energy and vacuum potential from calculations of the metals in slab-supercell geometries. However, work functions calculated with slab approximations are known to have a dependency on the thickness of the slab, thus further analysis is required to extract bulk metal work functions from slab approximation. This dependency is well documented in some cases and is attributed to finite size effects arising from classical electrostatic interactions or from quantum size effects (QSE) [49, 50, 51]. Methodology to lessen such effects is available in the literature [52].

Here we calculate the relaxations, surface energies, and work functions of the (111), (100), and (110) surfaces of Al, Pd, Pt, and Au and the (0001) surface of Ti

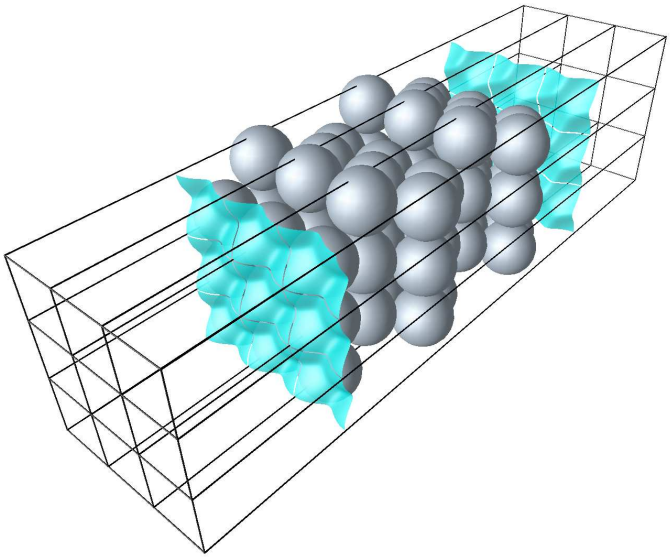

Figure 4.1: An illustration of a typical slab-supercell unit cell for the metal surfaces studied here. Pictured here are nine unit-cells of Al(111) slab that is seven layers thick. An isodensity surface is used to illustrate the (111) surface.

within DFT. We examine the convergence of all three quantities with respect to the thickness of the slabs, following the surfaces of Pd as an example. Furthermore, we employ and compare a number of different methods of calculation with respect to surface energy and work function. Well-converged values of these quantities for all of the metals and surfaces of this study are tabulated and compared, when available, to experimental quantities and/or DFT-LDA quantities from the literature. Some of the LDA generated data from the literature, and compared to here, were calculated with surface Green's functions methodologies [46, 53, 54]. These methods have been shown to be highly accurate, as well as inherently free from finite-size effects due to choices of boundary conditions. However, we feel that the widespread adoption and use of plane-wave DFT methods for more complex systems highlights the necessity for well converged slab-supercell calculated quantities.

4.2 Methodology

First-principles calculations within density functional theory are carried out using the PWscf code of the Quantum-ESPRESSO distribution [12], implemented in a manner described in Chapter 2. The Perdew-Burke-Ernzerhof (PBE) functional within the generalized gradient approximation (GGA) is used [11]. For the Brillouin-zone integration, we use a Monkhorst-Pack set of special **k**-points [55], and Marzari-Vanderbilt smearing [56] with a broadening of 0.02 Ryd.

Ultrasoft pseudopotentials (USPP) are used for Pd, Pt, and Au. For the case of Pd and Pt the USPPs used have been generated with the RRKJ3 scheme [57] with 10 valence electrons each in $4d^9 5s^1$ and $5d^9 6s^1$ configurations, respectively. The Au USPP have also been generated with the RRKJ3 scheme with 11 valence electrons in a $5d^{10} 6s^1$ configuration. These four USPPs are available at the PWscf website. [12] For the case of Ti the USPP was generated using the Vanderbilt scheme [58] with 12 valence electrons in a $3s^2 3p^6 4s^2 3d^2$ configuration. A normconserving pseudopotential is used for Al with electrons in a $3s^2 3p^1$ configuration. The kinetic energy cutoff for the plane wave basis are 32 Ryd for the wave function and 512 Ryd for the charge density for Al, Pd, Pt, and Au. For Ti these values are 40 Ryd and 640 Ryd, respectively.

Surfaces were constructed using a supercell with a thin slab of metal separated from its periodic images by a layer of vacuum. The size of this region is such that there are always ~ 16Å of vacuum between the surfaces; refer to Figure 4.1 for an example. For all the slabs considered, each layer in the unit cell contains one inequivalent atom. For (111) surfaces a hexagonal cell with a base defined by $a_0[110]$ and $a_0[101]$ and an inter-layer spacing of $\frac{a_0}{\sqrt{3}}$ and a stacking of ABCABC is used, where a_0 is the equilibrium lattice parameter. The other surfaces are similarly constructed; for (100) a tetragonal cell is used with a base formed by $\frac{a_0}{\sqrt{2}}[110]$ and $\frac{a_0}{\sqrt{2}}[1\bar{1}0]$ where the inter-layer spacing is $\frac{a_0}{2}$ and ABAB stacking. The (110) surface is constructed from an orthorhombic cell with a base defined by $\frac{a_0}{\sqrt{2}}[110]$ and $a_0[100]$ with an inter-layer spacing of $\frac{a_0\sqrt{2}}{4}$ and ABAB stacking. For the case of Ti the hexagonal cell is

used with a ABAB stacking in the z-direction.

The remaining methodological items are discussed in the following results section.

4.3 Bulk Properties

We calculate the lattice parameters and bulk moduli for Al, Pd, Pt, Au, and Ti. The calculations are performed for the total energy of the bulk system for a range of lattice parameters a. The total energy data are fit to the Murnaghan equation of state [59] to obtain the bulk moduli. For the case of bulk Ti, a hexagonal cell is used with a two atom basis to construct the hexagonal close packed (HCP) structure. Total energy calculations are performed for a range of c/a ratios and each of them fit to the Murnaghan equation of state. The results are found in Table 4.1. Here we see that the lattice parameters of the FCC Al, Pd, Pt, and Au are over estimated ($< 2\%$) by the use of the PBE-GGA exchange correlation functional. Similarly, for the bulk moduli the calculated values are underestimated with respect to the experimental values. However, for the calculations of these properties of Ti, PBE slightly overestimates the volume of the unit cell as well as over-estimating the bulk modulus. This type of behavior can be seen in a study of similar metals when calculated using PBE functional and using an FP-LAPW all electron methodology [47]. The remainder of this work the equilibrium lattice parameters calculated with PBE, found in Table 4.1, are used.

Recently in the literature, it has been shown that Pd calculated within GGA is incorrectly described as having a magnetic ground state in the bulk [60, 61]. To this end we also have calculated the bulk and surface properties of Pd with spin polarization. We also find that the ground state is described as magnetic, however, when applied to the surface properties, the introduction of magnetism has no noticeable effect. These calculations are reported and discussed in Appendix B.

Table 4.1: Calculated lattice parameters and bulk moduli of the metals considered in this study compared with experimental values.

	a_0 (Å)(c/a)	$a_{0,\text{expt.}}$ (Å)(c/a)	B (GPa)	$B_{expt.}$(GPa)
Al	4.06	4.05[a]	74	79[a]
Pd	3.98	3.89[a]	163	195[b]
Pt	3.99	3.92[a]	246	288[c]
Au	4.16	4.08[a]	140	180[d]
Ti	2.95 (1.57)	2.95 (1.59)[a]	121	110[e]

[a]Ref. [62]
[b]Ref. [63]
[c]Ref. [64]
[d]Ref. [65]
[e]Ref. [66]

4.4 Surface Relaxations

Surface relaxation is characterized as the percent change Δd_{ij} of the spacing between layers i and j versus the equilibrium layer spacing d_0. For the (111), (100), (110), and (0001) surfaces d_0 is $a_0/\sqrt{3}$, $a_0/\sqrt{2}$, $a_0\sqrt{2}/4$, and $c_0/2$, respectively.

As an example, the layer relaxations for Pd(100) as a function of slab thickness can be seen in Figure 4.2: Convergence of the relaxed layer spacing is achieved with increasing number of layers, and a slab thickness of 13-layers assures all relaxations are converged to within 0.1%. We show in Table 4.2 the top three surface layer relaxations for all surfaces for 13-layer slabs. As expected, the relaxation of the surface layers is related to the density of packing [43], with larger relaxation for the less-densely packed surfaces, with patterns of multilayer relaxation that become noticeable as we go from (111) to (100) to (110) surfaces. For the case of Ti(0001), the surface is hexagonal close-packed, however the large layer spacing leads to large relaxations. Comparison to low-energy electron diffraction (LEED) and other experimental values shows that our well converged values do not correspond directly to the experimentally observed values. However, regarding first layer relaxation or expansion, the qualitative trend is captured in all but the (100) surfaces.

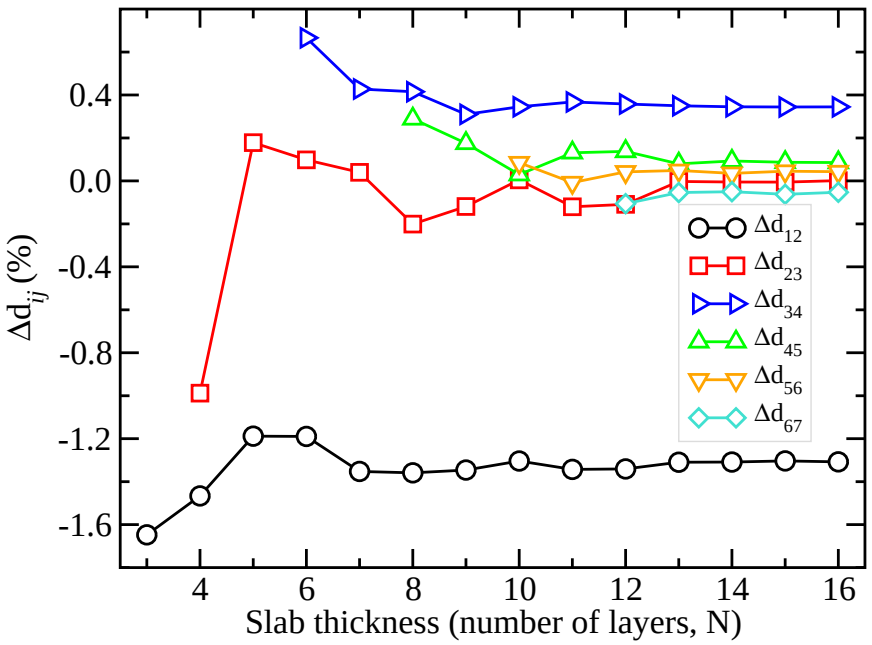

Figure 4.2: Layer relaxations for the top six layers of Pd(100) as a function of slab thickness. The numbers reported are the percent change, Δd_{ij}, of the spacing between layers i and j versus the initial layer spacing d_0 (for the (100) case $d_0 = a_0/\sqrt{2}$).

Finally, we note that for this study we are typically concerned with clean non-reconstructed surfaces (larger supercells in the in-plane dimension could allow for surface reconstruction). Some of the more widely know surface reconstructions are the $(22 \times \sqrt{3})$-reconstruction of the Au(111) surface [67], the (2×1) missing-row reconstruction of the (110) surfaces of Pt and Au [68, 69], and a number of reconstructions of the (100) surfaces of Au and Pt, the most studied being what is called the (100)-hex [70, 71]. To this end we investigate for comparison the Au(110) and Pt(110)(2×1)-missing row reconstruction for 13-layer slabs. We find that in both cases the first-layer relaxation more closely matches that of the experimental values in Table 4.2; -19.7% and -18.6% for Au and Pt, respectively. However, no improvement in see in the second layer relaxation. Finally, the surfaces of the $4d$-metal Pd as well as the Ti(0001) surface are know to be less likely to reconstruct at low temperatures.

Table 4.2: Surface relaxations for the top layer of all surfaces considered in this study. Reported are the values for a 13-layer slabs, compared to LDA and experimental values from the literature. For surfaces that are known to reconstruct, experimental values and those calculated as reconstructed in this study are given in square brackets.

	$\Delta d_{12}(\%)$		
Surface	PBE	LDA	Expt.
Al (111)	+1.04	+1.38 [72]	$+1.7 \pm 0.3$ [73]
			$+1.4 \pm 0.5$ [74]
(100)	+1.73	+0.5 [75]	$+2.0 \pm 0.8$ [76]
(110)	−5.59	−6.9 [77]	−8.4 [78]
Pd (111)	+0.25	−0.22 [47]	$+1.3 \pm 1.3$ [79]
		−0.1 [46]	$+0.0 \pm 4.4$ [80]
(100)	−1.30	−0.6 [46]	$+3.0 \pm 1.5$ [81]
			$+0.3 \pm 2.6$ [82]
(110)	−8.49	−5.3 [46]	-5.8 ± 2.2 [83]
			-5.1 ± 1.5 [84]
Pt (111)	+0.85	+0.88 [47]	$+1.1 \pm 4.4$ [85]
			$+0.5 \pm 0.9$ [86]
			$+1.4 \pm 0.9$ [87]
(100)	−2.37		$+0.2 \pm 2.6$ [88]
(110)	−15.03		$[-18.5 \pm 2.2]$ [89]
	[−18.62]		$[-19.5 \pm 7.2]$ [90]
Au (111)	−0.04	+0.8 [91]	
(100)	−1.51	−1.2 [92]	$[-20 \pm 3]$ [93]
(110)	−12.94	−9.8 [94]	$[-20.1 \pm 3.5]$ [95]
	[−19.7]		$[-18.1 \pm 6.9]$ [96]
			$[-22.2 \pm 6.9]$ [90]
Ti (0001)	−6.47	−6.44 [47]	−4.9 [97]

Table 4.3: Surface relaxations for the second layer of all surfaces considered in this study. Reported are the values for a 13-layer slabs, compared to LDA and experimental values from the literature. For surfaces that are known to reconstruct, experimental values and those calculated as reconstructed in this study are given in square brackets.

	$\Delta d_{23}(\%)$		
Surface	PBE	LDA	Expt.
Al (111)	-0.54		$+0.5 \pm 0.7$ [73]
(100)	$+0.47$		$+1.2 \pm 0.7$ [76]
(110)	$+2.20$		$+4.9$ [78]
Pd (111)	-0.34	-0.53 [47]	-1.3 ± 1.3 [79]
(100)	-0.00		-1.0 ± 1.5 [81]
(110)	$+3.47$		$+1.0 \pm 2.2$ [83]
			$+2.9 \pm 1.5$ [84]
Pt (111)	-0.56	-0.22 [47]	
(100)	-0.55		
(110)	$+7.61$		$[-24.2 \pm 4.3]$ [89]
	$[+10.59]$		$[-7.9 \pm 5.8]$ [90]
Au (111)	-1.86	-0.3 [91]	
(100)	$+0.33$	$+0.4$ [92]	$[+2 \pm 3]$ [93]
(110)	$+7.83$	$+7.8$ [88]	$[-6.2 \pm 3.5]$ [95]
	$[+10.45]$		$[-6.8 \pm 6.9]$ [96]
Ti (0001)	$+4.01$	$+2.64$ [47]	$+1.4$ [97]

4.5 Surface Energies

4.5.1 Methodology

The surface energy is the energy required to create a new surface, and as mentioned earlier, it is a difficult quantity to determine experimentally. In our calculations the surface energy σ can be determined by taking the energy difference between the total energy of a slab and an equivalent bulk reference amount, as seen in the following expression:

$$\sigma = \lim_{N\to\infty} \frac{1}{2}(E^N_{\text{slab}} - NE_{\text{bulk}}), \tag{4.1}$$

Table 4.4: Surface relaxations for the third layer of all surfaces considered in this study. Reported are the values for a 13-layer slabs, compared to LDA and experimental values from the literature. For surfaces that are known to reconstruct, experimental values and those calculated as reconstructed in this study are given in square brackets.

	$\Delta d_{34}(\%)$		
Surface	PBE	LDA	Expt.
Al (111)	+0.19		
(100)	−0.27		
(110)	−1.29		
Pd (111)	+0.10	−0.33 [47]	$+2.2 \pm 1.3$ [79]
(100)	+0.35		
(110)	−0.19		
Pt (111)	−0.15	−0.17 [47]	
(100)	+0.29		
(110)	−1.70		
	[−9.57]		
Au (111)	−1.40		
(100)	+0.24		
(110)	−2.66	−0.8 [94]	
	[−11.03]		
Ti (0001)	−0.68	+0.37 [47]	-1.1 [97]

where E^N_{slab} is the total energy of an N-atom slab, E_{bulk} is the total energy of the bulk per atom, and the factor $\frac{1}{2}$ accounts for the two surfaces in the slab unit-cell. However, this expression will diverge with increasing slab thickness if there are numerical differences between the calculation for the bulk and the slab (such as differences in the **k**-point mesh, etc.) [45]. Two methods have been suggested to determine surface energies while avoiding this divergence. Boettger [45] uses the bulk energy in Eqn. 4.1 as:

$$E^N_{\text{slab}} - E^{N-1}_{\text{slab}}, \tag{4.2}$$

thus avoiding a calculation on a separate bulk system and effectively eliminating the errors from differences in **k**-point sampling, while Fiorentini and Methfessel [98] make

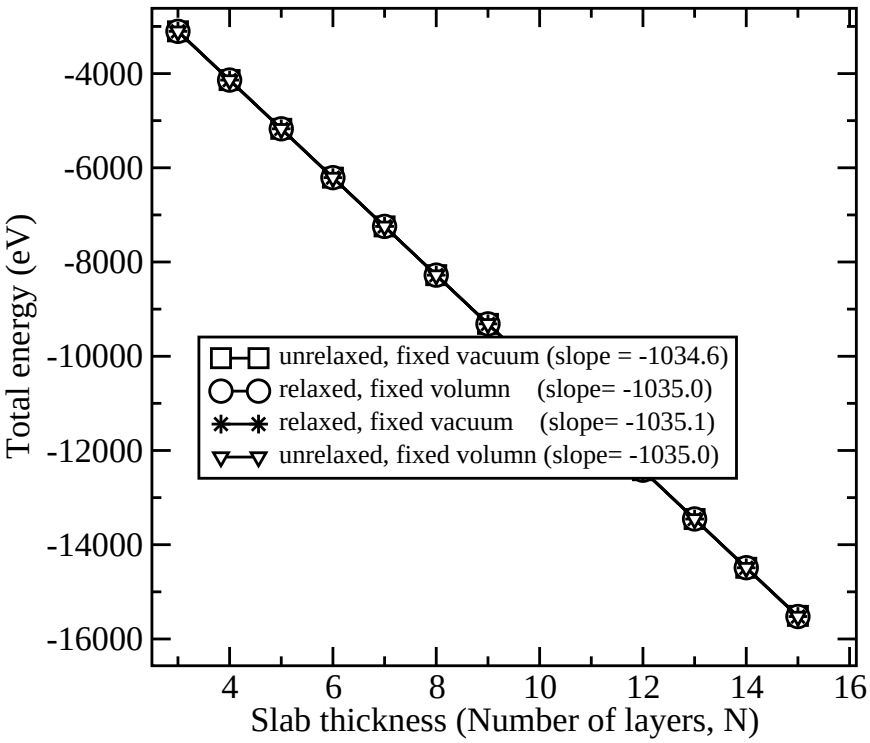

Figure 4.3: Total energy versus the thickness of a slab with Pd(100) surfaces. The four lines represent calculation where the surface was fully relaxed and not fully relaxed in cells with either a fixed volume of 22 layers or a fixed 6 layer vacuum region.

the assumption that in the limit of large N one can rewrite Eq. 4.1 as:

$$E^N_{\text{slab}} \approx 2\sigma + NE_{\text{bulk}}. \tag{4.3}$$

If the total energy of the slab depends linearly on slab thickness N, the bulk energy term E_{bulk} can be taken as the slope and used in Eq. 4.1, also avoiding a calculation on a separate bulk system. An example of the linear behavior of the total energy versus slab thickness for the Pd(100) surface is found in Figure 4.3. In practice, it has been shown that divergence can be avoided when large and matching **k**-point samplings are used for the slab and bulk calculations [47]. Here we compare these three methods using the labels "Boettger", "Fiorentini", and "direct" respectively. Figure 4.4 shows the comparison of surface energy versus slab thickness for Pd(100) surface

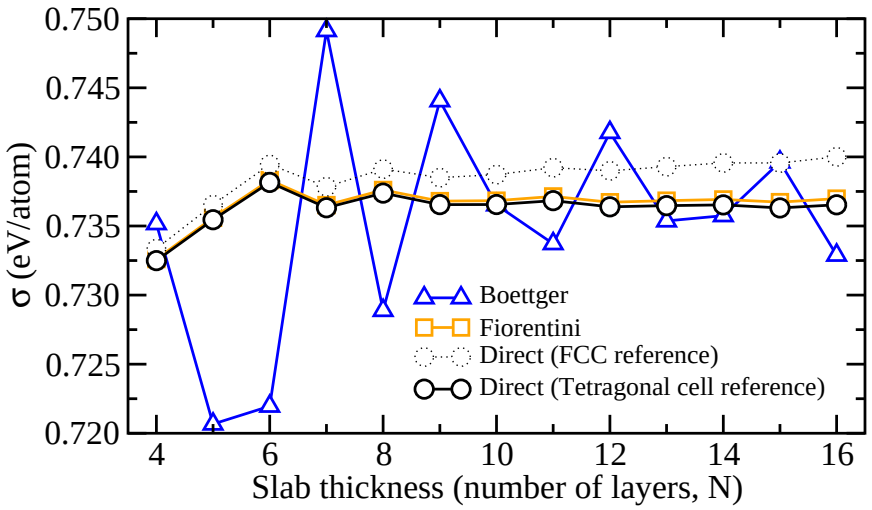

Figure 4.4: Surface energy versus slab thickness for the Pd(100) surface calculated with the methods of Boettger [45], Fiorentini and Methfessel [98], and directly from Eq. 4.1 with two different values for E_{bulk}.

energies. Here two different calculations are performed for the "direct" determination of E_{bulk}. First, a single FCC unit cell with a $16 \times 16 \times 16$ **k**-point mesh (dashed circles in Figure 4.4) and second a two atom tetragonal unit cell with a $16 \times 16 \times 11$ k-point mesh to, as closely as possible, match that of the **k**-point mesh used for the slab (solid circles in Figure 4.4).

It can be seen from Figure 4.4 that the best non-divergent results as a function of slab thickness are obtained with the method of Fiorentini and Methfessel, while the method of Boettger oscillates around these converged values. This periodicity is likely a manifestation of the finite size effects discussed earlier. Furthermore, even though a linear regression of the total energy versus slab thickness yields an excellent fit, the localized slopes $(E^{N}_{\text{slab}} - E^{N-1}_{\text{slab}})$ of the Boettger method lead to energy fluctuations in the bulk reference energy of the order 1×10^{-3}eV. These fluctuations are further amplified by the factor $-N$. These same fluctuations can be seen in all methods when comparing surface energy data for any given slab thicknesses N and $N \pm 1$; however, the choice of bulk reference in the direct and Fiorentini methods do not further amplify them. Finally, neither the Boettger or Fiorentini methods diverge in

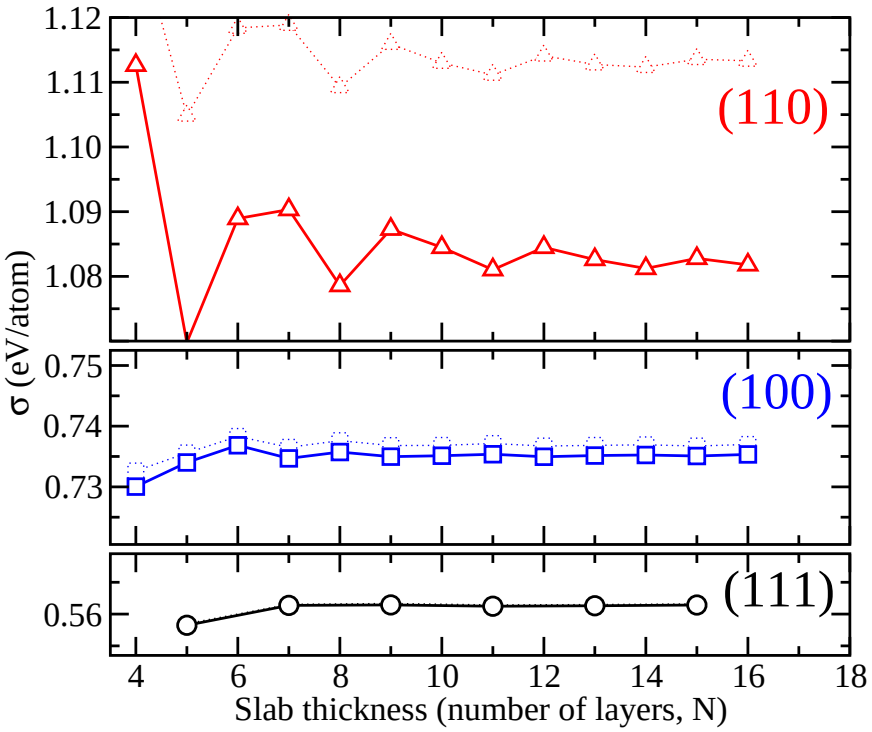

Figure 4.5: Surface energies of unrelaxed (dashed lines) and relaxed (solid lines) slabs of Pd(110), Pd(100), and Pd(111) surfaces versus slab thickness.

the same manner that the direct method does when the **k**-point grids do not match well for the bulk and surface calculations (dotted circles in Figure 4.4). However, similar to the findings of Da Silva *et al.* [47], we find that if the same care is used when choosing the **k**-point mesh (as is the case for the solid circles in Figure 4.4) an acceptable result is achievable through the direct method. For the remainder of this paper reported surface energies are calculated with the method of Fiorentini and Methfessel.

4.5.2 Results

Surface energies are calculated for both relaxed (but unreconstructed) and unrelaxed surfaces of all metals considered in this study. As an example, Figure 4.5 shows the surface energies as a function of slab thickness for all three Pd surfaces, both

Table 4.5: Surface energies for 13-layer slabs in both unrelaxed and fully relaxed geometries reported here in (eV/atom). LDA and experimental values compared with the surface energy of the relaxed surfaces reported here in units of (J/m^2).

	Surface	σ_u (eV/atom)	σ_r (eV/atom)	γPBE[a] (J/m^2)	γLDA (J/m^2)	γExpt. (J/m^2)
Al	(111)	0.30	0.30	0.67	1.27[b]	1.14[c]
	(100)	0.45	0.44	0.86		
	(110)	0.70	0.68	0.93		
Pd	(111)	0.56	0.56	1.31	1.87[d],1.64[e]	2.00[c]
	(100)	0.74	0.74	1.49	1.86[e]	
	(110)	1.11	1.08	1.55	1.97[e]	
Pt	(111)	0.65	0.65	1.49	2.23[d]	2.49[c]
	(100)	0.91	0.90	1.81		
	(110)	1.38	1.30	1.85	2.48[f]	
Au	(111)	0.35	0.35	0.74	1.04[g]	1.50[c]
	(100)	0.46	0.46	0.85	1.39[h]	
	(110)	0.71	0.69	0.90	1.55[f]	
Ti	(0001)	0.97	0.92	1.96	2.27[d]	1.99[c]

[a]Present study
[b]LDA-SGF [53]
[c]Ref. [44]
[d]LDA-Slab [47]
[e]LDA-SGF [46]
[f]LDA-Slab [99]
[g]LDA-Slab [91]
[h]LDA-Slab [92]

unrelaxed (dashed lines) and relaxed (solid lines). From the figure it is clear that surface energies are well converged for slabs as thin as 6-layers. Also, as expected, the surfaces that relax the most – i.e. (110) – experience the largest change in surface energy.

Calculated values for 13-layer slabs for all metals studied can be found in Table 4.5. All of the values calculated are converged with an accuracy comparable to those of Figure 4.5. Furthermore, in the table we compare our present PBE calculated values with LDA and experimental values from the literature. Remarkably, PBE seems to underestimate surface energies by as much as a factor of 2. In this context, we note the existence of exchange-correlation functionals that address this class of

problem [100, 101]. Finally, if better comparison to experimental values is desired, LDA represents the better choice of exchange-correlation functional for all of the (111) surfaces for which data was available. However, the converged value of surface energy for the Ti(0001) surface, calculated within PBE-GGA appears to more closely match the experimental data.

4.6 Work Function

As mentioned earlier, the work function is the minimum energy needed to remove an electron from the bulk of a material trough a surface to a point outside the material, and can be written as:

$$\Phi = V_{\text{vacuum}} - E_F. \tag{4.4}$$

4.6.1 Methodology

Again we need to test the calculation of the work function through use of the slab-supercell approximation. Thus, we compare and discuss the calculation of work functions *a posteriori* by two methods. First, we use directly Eq. 5.9, where both the potential in the vacuum region V_{vacuum} and the Fermi energy E_F are derived from the same calculation. Second, we use a methodology utilizing macroscopic averages [102, 52]. Here we take the macroscopic average of a potential step across the surface of the slab,

$$\Delta V = V_{\text{vacuum}} - V_{\text{slab interior}}, \tag{4.5}$$

and reference it to the macroscopic average of a potential obtained from a calculation on a separate bulk system, $V_{\text{bulk}}^{\text{Macro}}$. This allows for the use of the Fermi energy from the bulk system $E_{F,\text{bulk}}$, which will not suffer from quantum size effects [52].

$$\Phi = \Delta V + V_{\text{bulk}}^{\text{Macro}} - E_{F,\text{bulk}} \tag{4.6}$$

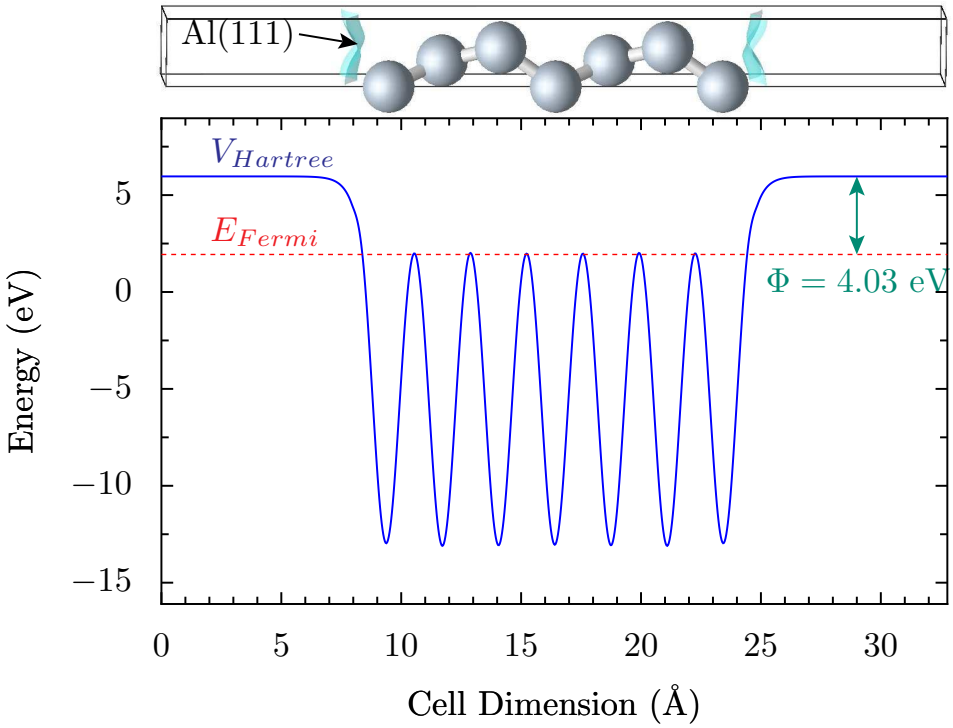

Figure 4.6: The work function of an Al(111) surface (single unit cell pictured above), taken as the difference of the Fermi energy and the electrostatic potential in the vacuum.

Note here that the window for macroscopic averaging is the unrelaxed equilibrium layer spacing. All of the potentials discussed here (both from the slab and the bulk reference) refer to the electrostatic part of the total potential (the Hartree potential). This part of the potential tails off more rapidly in the vacuum region of the slab-supercell when compared to the full Kohn-Sham potential including the exchange-correlation potential.

A comparison of these methods of calculation can be seen in Figure 4.7. Here the work function of Pd(100) slabs is plotted versus slab thickness for both the unrelaxed slabs (dashed lines) and relaxed slabs (solid lines). It is clear from the figure that both methods converge quickly for the unrelaxed case (in as little as 7-layers). However, when taking relaxation of all layers into account, the method of macroscopic averaging converges much more slowly. This is due to the fact that the averaging window for the

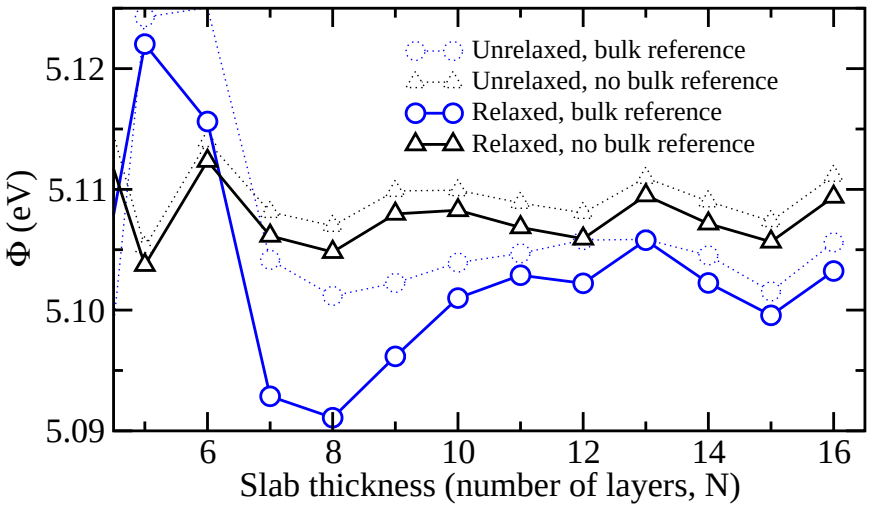

Figure 4.7: A comparison of work function calculations methods for work functions of Pd(100) slabs versus slab thickness. The bulk reference used is a single unit cell of FCC Pd.

reference potential and the layer spacing of the interior of the slab are not equivalent. Work functions reported in the remainder of this paper are taken directly by Eq. 5.9 without bulk references.

As a demonstration of the convergence of the work function as a function of slab thickness, the results for three Pd surfaces are shown in Figure 4.9. Here it can be seen that the work function of the (111) and (100) surfaces converges much more quickly than for the (110) surface. Even so, the work function of the (110) surface is converged to 0.1eV by 8-layers and $<$ 0.05eV by 11-layers. As in the previous subsection regarding the surface energy, oscillations can be seen. Furthermore, it is know that the work function of different facets can differ greatly [103] and the general trend is that work function will decrease with decreasing layer packing, which is consistent with the findings in Figure 4.9.

4.6.2 Results

Our final results for the work function of all the metals considered can be seen in Table 5.1; LDA and experimental values from the literature are provided when available.

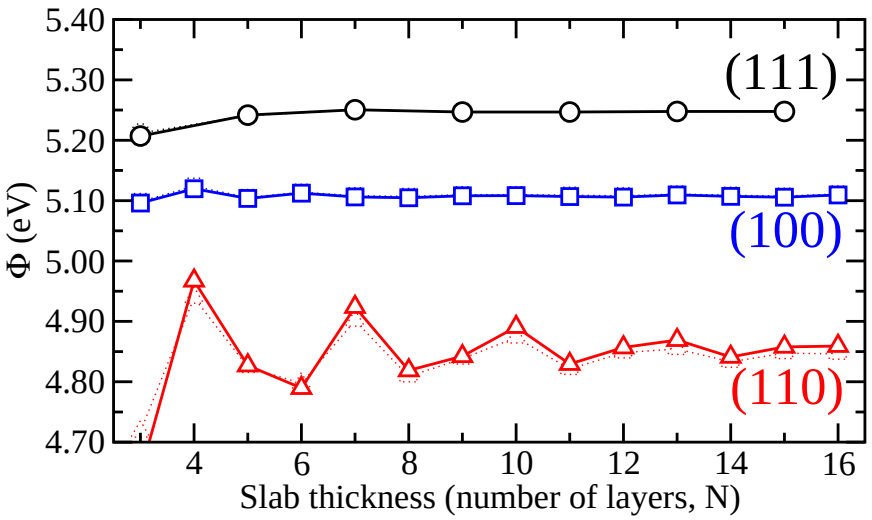

Figure 4.8: Work function versus slab thickness for the (111), (100), and (110) Pd surfaces, both unrelaxed (dashed lines) and relaxed (solid lines).

With the exception of Au and Ti, LDA again represents the better choice of exchange-correlation functional if a better match to experimental results is desired. Finally, regarding Al, we see the same anomalous behavior as recorded in Da Silva *et al.*, where the work function of the (111) and (110) surfaces are nearly equal, and the (100) has the larger of the three.

4.7 summary

Metals, and in particular metal surfaces, provide among other things the reaction surface for catalysis and the contact area for conductive devices. Thus, understating the surface properties of clean metallic surfaces can help develop a full picture of the systems containing them. Here we investigate the properties of metals that are used and proposed for contacts in current and future devices. The noble metals Au, Pt, and Pd are widely used in electronic system because they are good conductors and are more or less inert – i.e. they don't form performance-degrading oxides under working conditions. Ti is also a metal that is finding use in electronic systems. We investigate here the low index surfaces of these metals, in particular the (111), (100), and (110)

Table 4.6: Work functions calculated for 13-layer slabs of all metal faces considered in this study. All values in eV.

	Surface	Φ^a	Φ_{LDA}	$\Phi_{\mathrm{Expt.}}$
Al	(111)	4.02	4.25[b]	4.23[c]
	(100)	4.30	4.38[b]	4.42[c]
	(110)	4.09	4.30[d]	4.12[c]
Pd	(111)	5.25	5.64[e],5.53[f]	5.55[g]
	(100)	5.11	5.30[f]	
	(110)	4.87	5.13[f]	
Pt	(111)	5.69	6.06[e]	6.10[h]
	(100)	5.66		
	(110)	5.26	5.52[i]	
Au	(111)	5.15	5.63[j]	5.26[k]
	(100)	5.10	5.53[j]	5.22[k]
	(110)	5.04	5.41[j], 5.39[i]	5.20[k]
Ti	(0001)	4.38	4.66[e]	4.33[l]

[a]Present study
[b]LDA-Slab [104]
[c]Ref.[105]
[d]LDA-Slab [106]
[e]LDA-Slab [47]
[f]LDA-SGF [46]
[g]Ref. [107]
[h]Ref.[108]
[i]LDA-Slab [99]
[j]LDA-Slab [109]
[k]Ref.[110]
[l]Ref.[111]

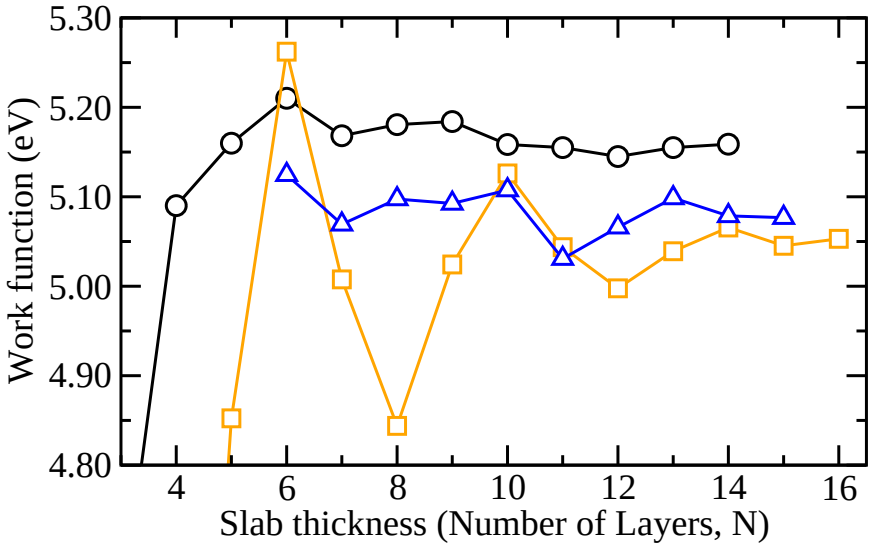

Figure 4.9: The work functions of Au(111) (circles), Au(110) (squares) and Au(100) (triangles) versus the slab thickness.

of the FCC metals Au, Pt, and Pd, and the (0001) basal surface of hexagonal Ti. We are mainly concerned with surface relaxations, surface energies, and work functions; and the illustration of the effects of slab thickness on these properties of interest. The calculated lattice parameters and bulk moduli of these metals can be found in Table 4.1.

Chapter 5

Carbon Nanotubes

Due to their many intriguing potential applications, carbon nanotubes (CNTs) are the focus of many experimental and theoretical studies. Engineering the properties of carbon nanotubes is of fundamental importance for many of their practical applications; we focus here on the work function of metallic nanotubes, and on the changes that can be induced by electropositive or electronegative functionalizations.

5.1 Introduction

Since their discovery in 1991 [112], CNTs have been the subject of an outstanding amount of scientific research.[1] While a simple introduction will not cover all of the great discoveries regarding CNTs, it should suffice to justify the excitement.

The first section of this Chapter serves as a general introduction to carbon nanotubes and the functionalization of CNTs. The remaining sections discuss the methodology (including a description of electrostatic corrections), the results, and discussion.

[1]There are other recorded experimental studies the mention in some part CNTs that predate Iijima's paper, however it has been convention to call the 1991 paper the discovery of CNTs.

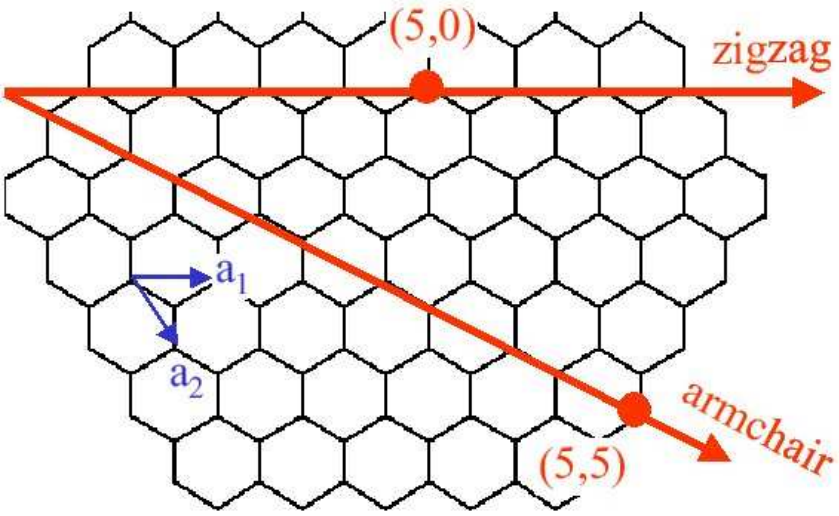

Figure 5.1: The chiral vector, $C = na_1 + ma_2$ is shown; the tube index is defined as (n,m). There are two special cases – zigzag and armchair ((n,0) and (n,n) respectively).

5.1.1 CNT Nomenclature

CNTs are essentially hollow tubes of graphite. They are small in size, with typical diameters on the nm scale and lengths on the μm scale. The order of magnitude difference in length to diameter and the underlying graphene-like symmetry make CNTs a quasi-one dimensional system. Furthermore, much like graphite can contain multiple layers, a CNT can have multiple walls. These coaxial CNTs are referred to as multi-wall nanotubes (MWNTs). However, for the sake of this document we are only concerned with single-walled nanotubes (SWNTs).

There are an infinite number of ways to 'roll' the graphene sheet into a CNT. Each CNT can be identified by a pair of indices (n,m). Where n and m define the chiral vector:

$$\mathbf{C} = na_1 + ma_2. \tag{5.1}$$

This is shown graphically in Figure 5.1, where one can envision a (n,m) CNT as simpling rolling up a graphene sheet along the appropriate chiral vector. In the figure two special cases are also noted; zigzag and armchair ((n,0) and (n,n) respectively).

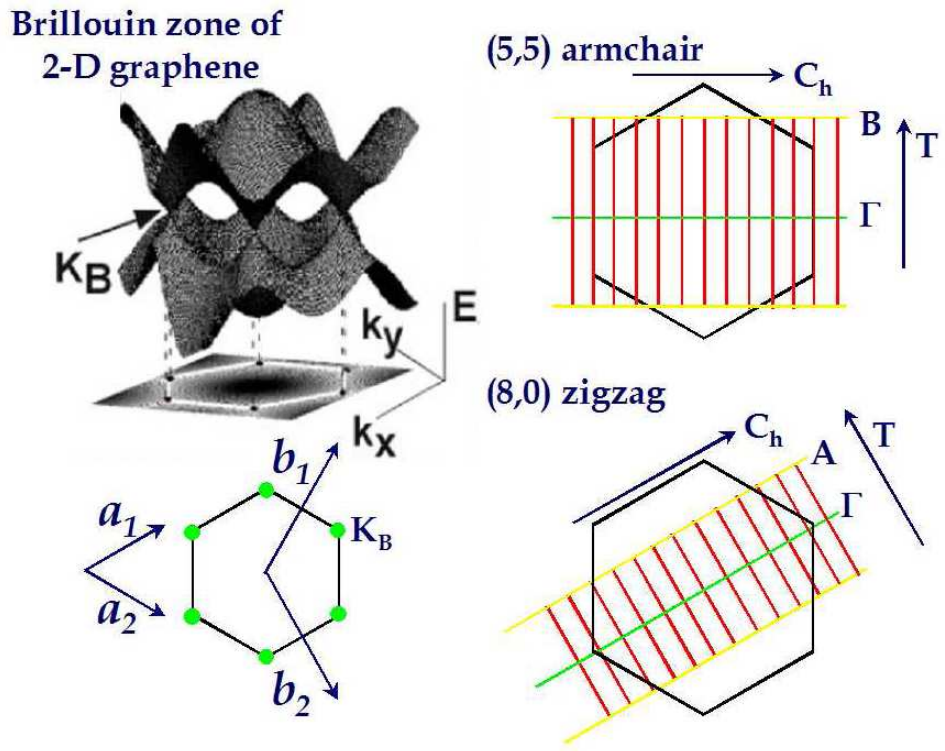

Figure 5.2: The electronic structure of graphene and how it corresponds to the CNT. Figure from Ref. [113])

5.1.2 Electronic Properties

One of the most fundamentally interesting and important properties of CNTs is that depending on the structure and the symmetry of the CNT, one can be classified as either a semi-conductor or a metal. More specifically, the electronic structure of CNTs is derived from graphene. The conduction bands of graphene meet the valence bands at a point (K) in the 2-D graphene Brillouin zone, Figure 5.2.

The CNT confines the wave function along the circumference, and leads to discritized wave vectors along the chiral vector. If one of the k-vectors of the discritized set passes through the K point the CNT will be metallic. Using the chiral vector

indices (n,m) a rule is developed to determine which is the case:

$$\mathrm{mod}(n-m,3) = \begin{cases} 0 & : \text{ Metallic} \\ 1,2 & : \text{ Semiconductor} \end{cases} \tag{5.2}$$

Of the two types of CNT considered in this thesis, the (5,5) CNT is metallic and ant (8,0) CNT is semiconducting. Further information on the fundamental properties of CNTs can be found in Ref. [114].

5.1.3 Functionalized CNTs

The functionalization of carbon nanotubes (CNTs) provides possible routes to both better process control and device performance engineering. For instance the difficult problems of solvation [115] and sorting [116] of CNTs often involve the addition of chemisorbed functional groups to the side walls of the CNT. Chemical additions ultimately change the sp^2 bonding structure of the CNT through introduction of sp^3 hybridization [117]. Thus it is of fundamental importance to understand the effect that chemical functionalization has on the electronic properties of CNTs.

We focus here on the work function of chemically functionalized CNTs. The work function of CNTs is a difficult quantity to measure experimentally. Typical experimental studies report only a spread of work function values for CNTs; for instance a spread of 0.2 eV is reported for single walled carbon nanotubes (SWCNTs) from a photo-emission electron microscopy (PEEM) study [118] and a spread of 0.5 eV as a function of diameter from Raman spectroscopy on SWCNTs in aqueous solution [119].

There have been a number of previous theoretical studies of work function of CNTs. These studies have shown that the work function of single-wall CNTs approach that of graphene for large diameter tubes ($>$ 1nm); however for small diameters ($<$ 1nm) the behavior is dependent on the chirality of the tube, where the work function of armchair (n,n) tubes increase with increasing diameter while the work

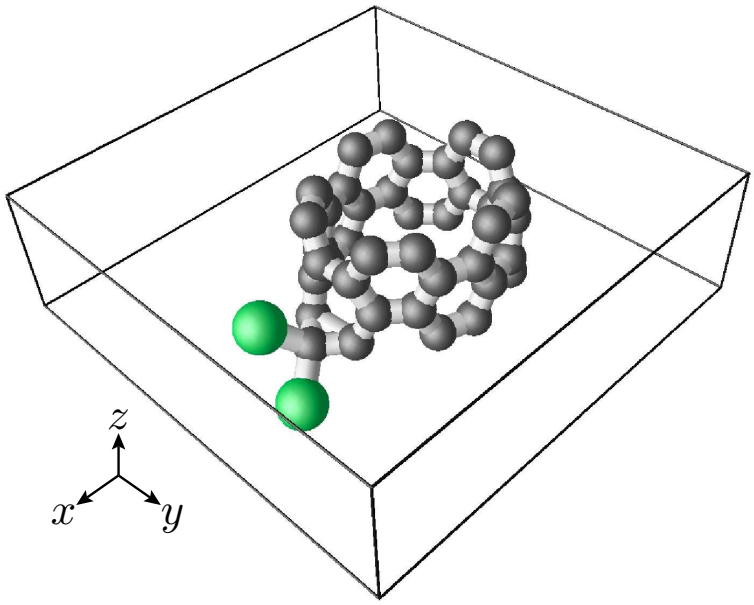

Figure 5.3: A representative unit cell of a (5,5) CNT functionalized with dibromo carbene in the horizontal (hor) position.

function of zigzag (n,0) tubes decrease [120, 121, 122]. Other studies have focused on the intercelation of metallic tubes and bundles with alkali metals, where it is shown that the addition of metal atoms tends to decrease the work function [122].

We study here with density functional theory (DFT) the covalent functionalization of the metallic (5,5) CNT and the semiconducting (8,0) CNT. We consider functional groups that can be categorized as either monovalent or divalent, in that the functional moiety bonds to either one carbon or two carbon on the CNT, respectively. We correct for spurious image dipole interactions self-consistently. We provide results for a number of functional groups, and discuss the observed trend that electropositive and electronegative functional groups tend to lower and raise the work function, respectively. We illustrate the reasons for these trends trough the investigation of charge transfer and resulting electrostatic potential for a representative example in both cases.

5.2 Methodology

We have constructed the one-dimensional periodic CNT using the supercell approximation within three-dimensional periodic boundary conditions (PBCs). The CNT was nominally placed along the z-axis and the size of the unit cell in the x- and y-directions was determined by the size of the functional group; an example of a typical unit cell can be seen in Figure 5.3. Two possible attachment geometries were considered for both the (5,5) and (8,0) CNTs. For the (5,5) CNT these two geometries are referred to as "horizontal"(*hor*) and "skew"(*skw*). In the *hor* geometry the functional group is bonded to two carbon atoms that are perpendicular to the longitudinal axis of the CNT (see Fig 5.3), while in the *skw* geometry the bonded carbons are at an angle of 30° to the longitudinal axis. The two geometries for the (8,0) CNT are referred to as "longitudinal"(*lon*) and "skew"(*skw*). In the *lon* geometry the functional group is bonded to two carbon atoms that are parallel to the longitudinal axis of the CNT, while in the *skw* geometry the bonded carbons are at an angle of 60° to the longitudinal axis.

5.3 Electrostatic Corrections

The addition of the covalent functional groups typically causes a charge asymmetry across the unit cell leading to the formation of a dipole. In PBCs this dipole can spuriously interact with its periodic images. We see in Figure 5.5 a comparison of the electrostatic potentials (averaged to a single xy-plane) for a (5,5) CNT functionalized with dibromo-carbene $(CBr)_2$) in the *skw* geometry. Figure 5.5 (A) shows the electrostatic potential calculated with PBCs, while Figure 5.5 (B) shows the potential calculated for the isolated CNT in open boundary conditions.

The dipole that has formed across the functionalized CNT is clearly visible in the Figure 5.5. These two potentials are unique, thus if we want to study the isolated case some care has been taken to eliminate the periodic image interactions. Because the

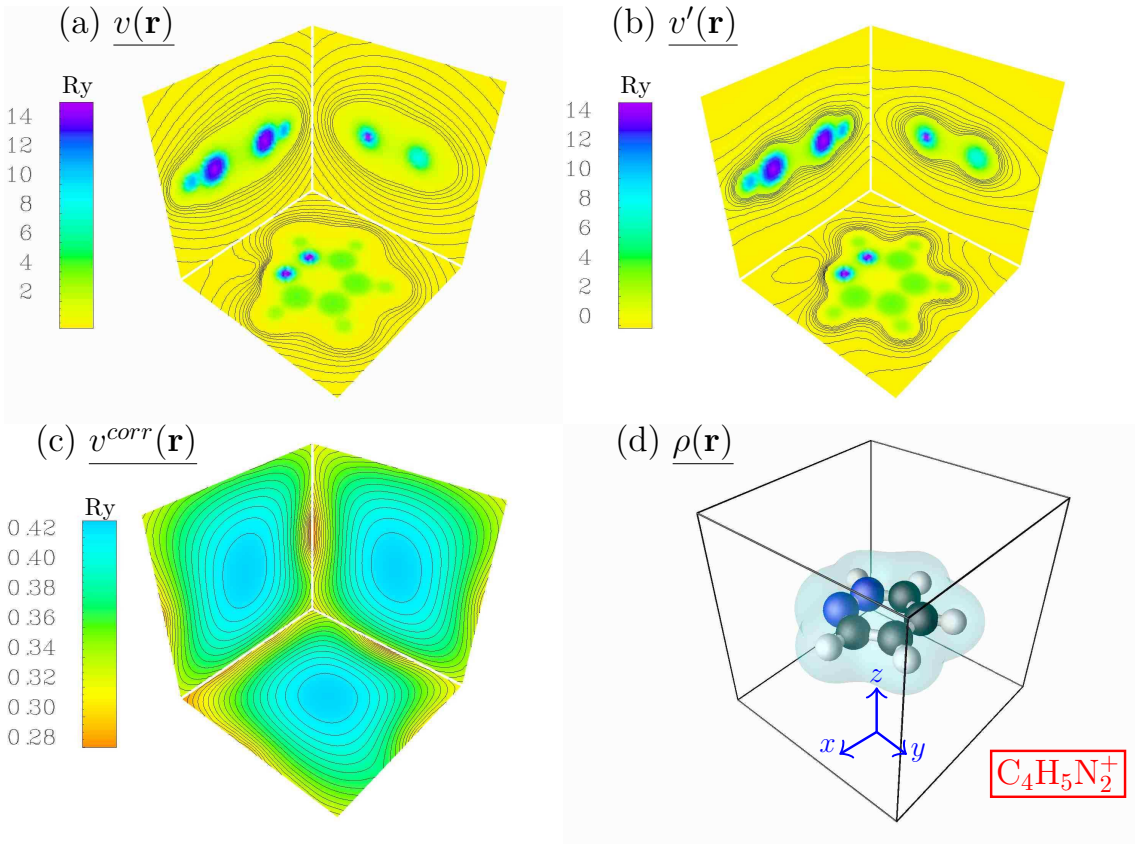

Figure 5.4: Panel (d) shows the pyrzidine cation, (a) The electrostatic potential solved for with open boundary conditions. (b) The electrostatic potential solved in periodic boundary conditions. (c) The quasi-parabolic corrective potential that is the difference between (a) and (b). Figure from Dabo *et al.* [123].

the total charge of the system remains zero, this can be done (at high computational cost) by increasing the dimensions of the vacuum region between the CNTs, where as the cell dimension L$\rightarrow \infty$ the potential calculated in periodic boundary conditions will approach the form of the isolated potential.

In general, representing systems that contain dipoles (and/or higher order multipoles) in a supercell with periodic boundary conditions (see Chapter 2) gives rise to spurious electrostatic interactions. This is a well-know issue in periodic boundary conditions, and thus a number of methodologies have been devised to correct for the errors. A few of these methods are reviewed in the following section, followed by a

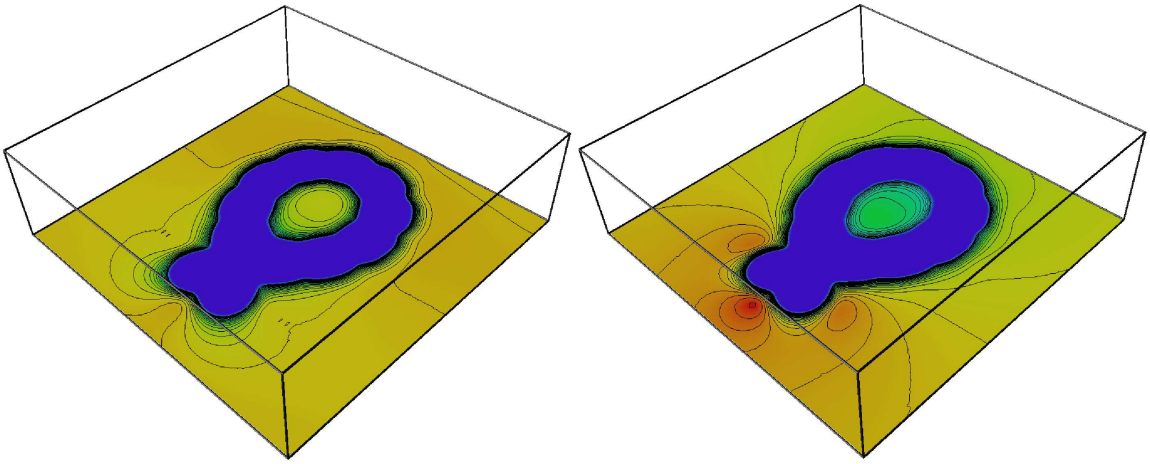

Figure 5.5: The electrostatic potential averaged to the xy-plane for a (5,5) CNT functionalized with a dibromo carbene in the skewed (skw) position; calculated with (A) periodic boundary condition (B) open boundary conditions.

more exact methodology.

In the paper of Makov and Payne [124] it is shown that the artifacts of these spurious interactions for neutral systems induce errors to the total-energy that scale as $1/L^3$, where L is the size of the supercell. By the method of Makov and Payne it is possible to correct the total energy *a posteriori*. However, corrections of this sort only deal with the final energy, and in some cases we are interested in obtaining the correct potential that surrounds a system. For such systems a correction by Jarvis *et al.*, the electrostatic-cutoff approach, suppresses these effects by damping the electrostatic potential beyond a certain interaction range [125]. Other proposed corrections introduce counter charges to correct the potential [126, 127].

In the method of Schultz [127], know as the local moment counter charge method (LMCC), the effects of spurious dipoles are corrected using Gaussian counter charges. Gaussians representing the respective charges are placed at the positive and negative charge centers. The real-space electrostatic potential is calculated for this system. Finally, the difference between the real-space potential of the isolated Gaussians and the periodic potential is the correction. This method takes advantage of the fact that the exact electrostatic potential will have tails into the vacuum that are well

represented by the potential of the Gaussians. Furthermore, there are well know analytical solutions to the potential of a Gaussian, thus the increase in CPU time due to correction is not prohibitive.

The total charge density (electronic plus ionic) can be used to calculate a correction to the electrostatic potential, rather than using the Gaussian counter charges discussed in the previous section. In this case a charge asymmetry has formed across the unit cell for a (5,5) carbon nanotube with two chemisorbed hydrogen atoms. The difference between the PBC potential, refereed to here as $v'(\mathbf{r})$, and the real-space potential, $v(\mathbf{r})$, is called here the corrective potential, $v^{corr}(\mathbf{r})$.

Here we use the correction scheme of Dabo *et al.* [123] where a corrective potential is added self consistently to compensate for the formation of electrostatic mulitpoles. The corrective potential v^{corr} is the difference between the periodic and isolated potentials, arrived at as follows.

The isolated charge density, ρ, generates a potential v that can be solved for with the Poisson equation

$$\nabla^2 v(\mathbf{r}) = -4\pi\rho(\mathbf{r}), \tag{5.3}$$

in open boundary condition ($v(\mathbf{r}) \to 0$ as $r \to \infty$), this leads to the integral expression:

$$v(\mathbf{r}) = \int \frac{\rho(\mathbf{r}')}{|\mathbf{r} - \mathbf{r}'|} d\mathbf{r}', \tag{5.4}$$

which corresponds to the potential in Figure 5.4(a) and Figure 5.5(B).

For the case of a potential in periodic boundary conditions, a net zero charge has to be maintained, thus we have a similar differential equation:

$$\nabla^2 v'(\mathbf{r}) = -4\pi(\rho(\mathbf{r}) - \langle\rho\rangle). \tag{5.5}$$

Evaluating v' in reciprocal space, we have

$$v'(\mathbf{r}) = \sum_{\mathbf{g}\neq\mathbf{0}} \frac{4\pi}{\mathbf{g}^2}\rho(\mathbf{g})e^{i\mathbf{g}\cdot\mathbf{r}}, \tag{5.6}$$

where $v'(g=0) = \langle v' \rangle$ is set to zero.

Finally the difference between v and v' is the correction:

$$\nabla^2 v^{corr}(\mathbf{r}) = -4\pi\langle\rho\rangle. \tag{5.7}$$

This correction has been implemented numerically as part of the quantum-ESPRESSO distribution. There are some simplifications that can be made for a system that is periodic in less than three dimensions, for instance a slab (2D) or a CNT (1D).

The focus here is the one dimensional system, CNTs. The electrostatic correction to the 1D system can be calculated in 2D, reducing the computational cost of solving the Poisson equation.

In general the total charge ρ can be determined in 3D and subsequently averaged to a single plane , $\overline{\rho}(\mathbf{r})$, (normal to the axis of the 1D system), Figure 5.5. The Dirichlet boundary conditions needed to solve for the corrections in Eqn. 5.7 can the be solved with 2D solution for the Poisson equation:

$$v^{2D}(\mathbf{r}) = -4\int \overline{\rho}(\mathbf{r}')\ln(|\mathbf{r}-\mathbf{r}'|)d\mathbf{r}' \tag{5.8}$$

The correction then be re-exapanded uniformily to the 3D system and applied to the electrostic potential.

For the case of the CNT this 2D generalization is necessary to realize the periodicty of the CNT – i.e. the boundary conditions in the 3D case would truncate the potential leaving an isolated CNT piece. In this case the multipoles of the CNT are treated as infitite lines of charge interecting the 2D plane. However, there are some possible negeative side-effects to taking this averaging approach. In particular, one could

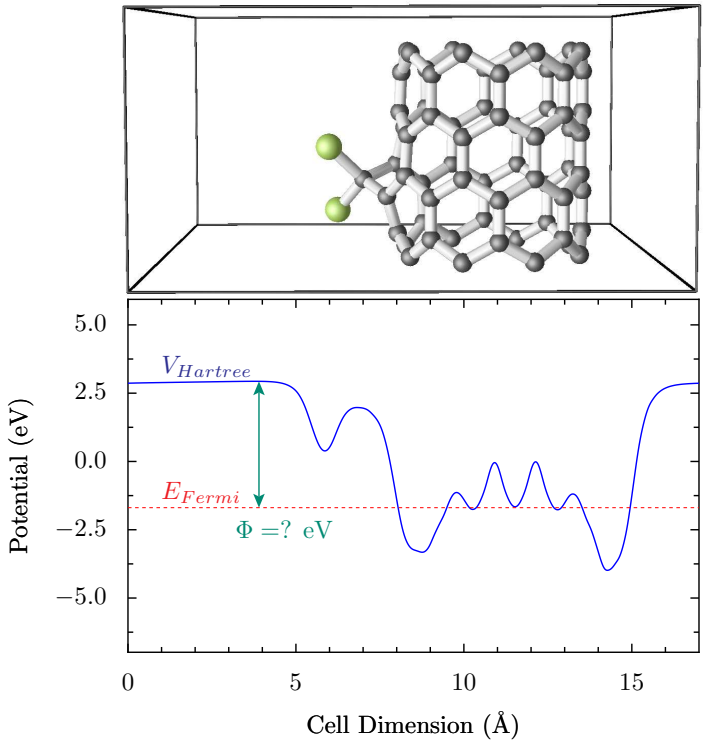

Figure 5.6: The dipole formation makes accurate determination of the vacuum level difficult for the isolated system (in periodic boundary conditions). Top panel, the unit cell for the (8,0) CNT functionalized with CCl_2. Bottom panel, planar average of the electrostatic potential along the x-axis in the system above.

concieve of a system that had ossilating charges along the 1D system that cancel each other out in the planar average (leaving no correction). One such case for a variaent of the polymer PVDF can be found in Appendix C and Ref. [123] along with further information about the implementaion of this correction.

5.4 Work Function Results

This section includes a definition of the work function and subsequently the results for all of the CNTs and functionalized CNTs considered in this study. A discussion

of the results is reserved for the following section.

The work function is the minimum energy required to extract an electron from the Fermi energy to a point outside the surface where the electron is no longer affected by the image potential that it generates. This can be expressed as

$$\Phi = V - E_F, \tag{5.9}$$

where V is the vacuum potential and E_F is the Fermi energy. For the case of semiconducting CNTs at zero temperature, the convention has been to place the Fermi energy in the center of the band-gap [128, 121], such that

$$E_F = E_V + \frac{E_g}{2}, \tag{5.10}$$

where E_g is the band gap and E_V is the energy of the valence band edge.

We investigate here both metallic and semiconducting CNTs, thus work functions are calculated using Eqn. 5.9 and Eqn. 5.10, respectively. For the semiconducting case the band gap E_g is determined from a band structure calculation using a larger number of **k**-points for the Brillouin-zone integration.

We investigated the effect a number of different covalent functionalizations have on work function. These functionalizations can be grouped into two types; monovalent and divalent. The monovalent functional groups bond to one carbon on the CNT while the divalent bond to two. The results are presented in the following subsections.

5.4.1 Pristine

First we considered the CNT with no functional group attached (called herein the pristine case). The minimal unit cells for the pristine (5,5) and (8,0) CNTs contain 20 atoms and 16 atoms, respectively.

It is well known that the (5,5) CNT is metallic [129]. Therefore, using Eqn. 5.9, we find a work function of 4.27 eV. This value is lower than the LDA-DFT value of

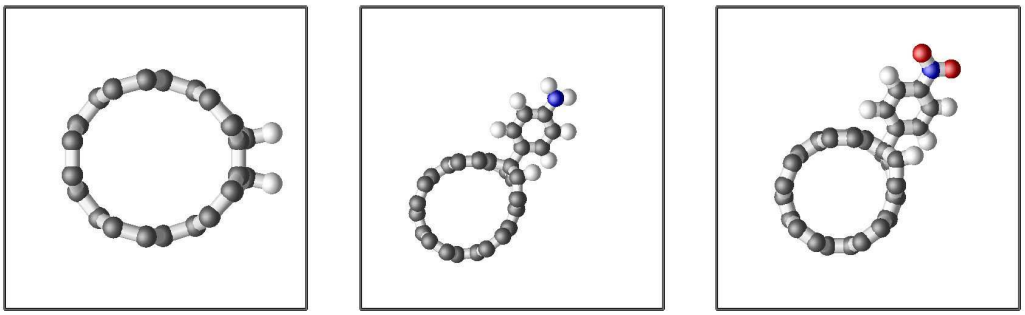

Figure 5.7: The monovalent functionalizations. left: 2 H atoms in the *hor* position, center: amino-phenyl in the *skw* position, right: nitro-phenyl in the *skw* position.

Table 5.1: Work function and coverages for all of the functionalized (5,5) CNTs considered in this study.

Functional group	Coverage (%)	Φ(eV)	$\Delta\Phi$(eV)
none (pristine)	-	4.27	0.0
2 Hydrogen (hor)	3.3%	4.12	-0.15
2 Hydrogen (skw)	3.3%	4.21	-0.06
Nitrophenyl+H	3.3%	4.64	+0.37
Aminophenyl+H	3.3%	3.90	-0.36
CCl_2 (hor)	5.0%	4.38	+0.11
CCl_2 (skw)	5.0%	4.49	+0.22
CBr_2(hor)	5.0%	4.03	-0.24
CBr_2 (skw)	5.0%	4.45	+0.18
$C(CH)_2$ (hor)	5.0%	4.20	-0.07
$C(CH)_2$ (skw)	5.0%	4.16	-0.11

4.6 eV [120]. While for the semiconducting (8,0) CNT we calculated a work function of 4.72 eV; compared to the LDA values of 4.8 eV [120].

5.4.2 Monovalent Functionalization

For the (5,5) CNT the monovalent functional groups studied were atomic hydrogen and the aryl groups nitrophenyl and aminophenyl. It has been shown in the literature that a pair of hydrogen atoms bonded to the CNT is more energetically favorable than a single adsorbed hydrogen [130, 131] and that the hydrogen pair is most stable when

bound to nearest neighbor sites [132]. Therefore we study monovalent functional groups in pairs. For the case of hydrogen this resulted in two hydrogen atoms and for the case of the aryl groups, the aryl functional group was paired with a hydrogen atom on the nearest *skw* site, Figure 5.8. Furthermore, the coverage, which is computed as the number of bonded carbon atoms divided by the total number of carbon atoms of the CNT, is chosen to be 3.3% for these cases. This corresponds to a unit cell containing 3 'layers' of the 20 atom CNT unit cell. It was found that for higher coverages – i.e. 5% – that the breaking of the sp^2 hypbridization in favor of sp^3 hybridization causes the tube structure to be unstable, subsequently causing it to break apart during geometry optimization. This is tendancy is documented in a LDA-DFT study of the adsorption of atomic hydrogen on SWCNTs [133].

The work function results for the monovalent functionalization (5,5) CNT are found in Table 5.1. Here we see that the monovalent addition can both lower and increase the work function with respect to the pristine case. The addition of hydrogen at 3.3% coverage lowers the work function of the CNT in both the *hor* and *skw* geometries, as does the addition of aminophenyl. While the addition of nitrophenyl leads to an overall increases of the work function. These trends are ultimately the result of charge rearrangement on the CNT, where the more addition of the more electropositive functionalization will lead to an overall lower work function. This trend is discussed in more detail in the discussion section of this paper.

For the (8,0) CNT we studied only the addition of two atomic hydrogen in the *lon* and *skw* geometries. These results are found in Table 5.2. We again see the lowering of the work function with respect to the pristine case for the addition of hydrogen.

5.4.3 Divalent Functionalization

The divalent functionalizations considered here are classified as carbenes. The carbene binds two sites on the CNT. These carbenes are typically added experimentally through [2+1] cycloaddition reactions, where a small three member ring is formed

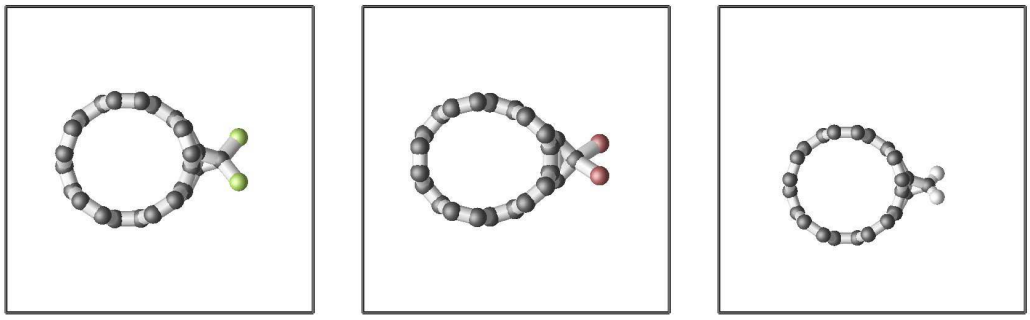

Figure 5.8: The monovalent functionalizations. left: dichloro-carbene (CCl_2) in the *skw* position, center: dibromo-carbene (CBr_2 in the *hor* position, right: CH_2 in the *skw* position.

Table 5.2: Work function and coverages for all of the functionalized (8,0) CNTs considered in this study.

Functional group	Coverage (%)	Φ(eV)	$\Delta\Phi$(eV)
none (pristine)	-	4.72	0.0
2 Hydrogen (lon)	3.3%	4.59	-0.13
2 Hydrogen (skw)	3.3%	4.43	-0.29
CCl_2 (lon)	5.0%	4.83	+0.11
CCl_2 (skw)	5.0%	4.76	+0.04

by the carbon of the carbene and two carbon atoms of the CNT. The carbenes are know to preserve the sp^2 bonding system of the CNT [134]. We initially considered 5% coverage, where one 40 atom CNT unit cell containing one bonded carbene.

We report all of the work function values calculated for the (5,5) CNTs functionalized with carbenes in Table 5.1. Similar to the monovalent species, some of the carbenes tend to lower the work function, while other raise it. Again, this is due to the electropositive and electronegative nature of the functional additions, respectively.

From Table 5.1 it is seen that there is a dramatic difference between the work function of the CNT functionalized with CBr_2 in the *hor* versus the *skw* position at 5% coverage. The expected trend would be that the difference should be similar in magnitude as the CCl_2 case. This behavior is due to a bonding interaction of the

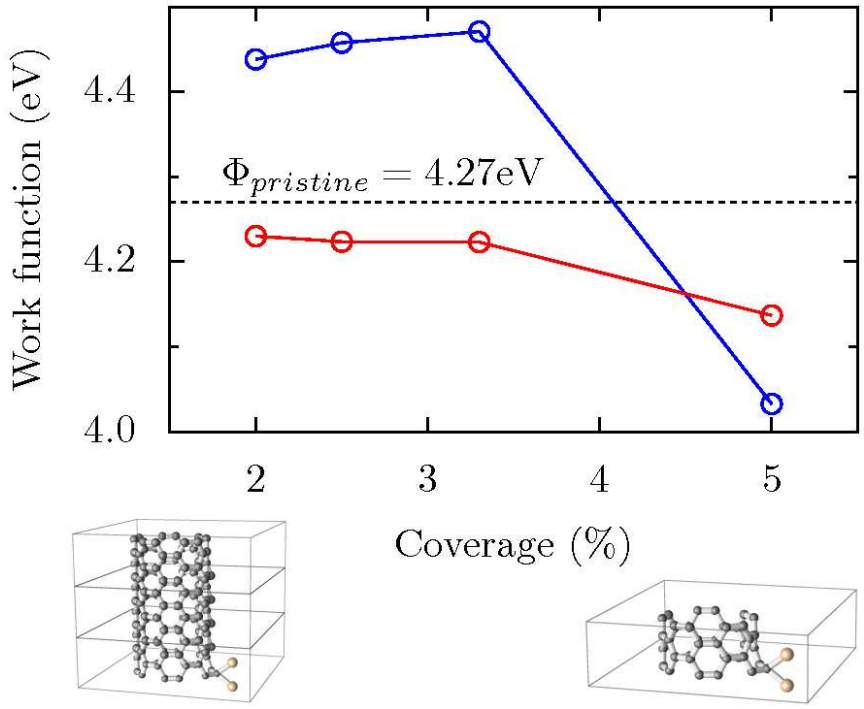

Figure 5.9: Dilute limit of work function of functionalized CNT. blue line: (5,5) CNT functionalized with CBr_2, red line: (5,5) CNT functionalized with 2 H atoms. The figures below are visual reference for the dilution of the functional group through addition of pristine sections of the CNT.

Br atoms along the backbone of the CNT at 5% coverage. The 5% coverage leads to periodic repeating functional groups that are close together in the *hor* geometry, such that the Br can bond to the the Br of the neighboring functional group. This results in a charge transfer situation that is dissimilar to that of the *skw* case. To verify that this is the case we perfored the same calculation at the lesser coverages of 3.3% and 2.5%, where we have calculated work function values of 4.47 eV and 4.46 eV, respectively, Fig 5.9.

5.5 Work Function Discussion

The trends observed in the results section point toward a possible division of functional moieties into two groups: electropositive and electronegative. Here the elec-

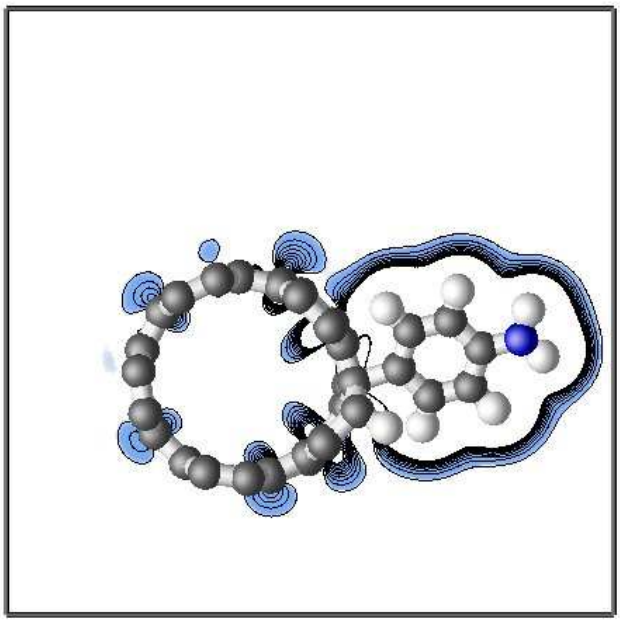

Figure 5.10: Density difference plots for (5,5) CNT functionalized with aminophenyl and a hydrogen. The density difference is taken as the functionalized CNT minus that of the clean CNT. The blue isodensity lines represent a charge transfer to the CNT.

tropositive addition refer to those that have a tendency to donate electrons to the CNT backbone; subsequently lowering the work function with respect to the pristine case. While the electronegative additions tend to pull electrons from the CNT onto the functional group; subsequently increasing the work function. The aim of this section is to show that this is indeed the case, and to further clarify this as the reason for the changes in work function.

5.5.1 Charge Transfer

To verify that the charge transfer occurs in the manner described above, we investigated the charge density differences for the electropositive and electronegative cases. Here we use the aminophenyl and the CCl_2 functionalizations to illustrate these phenomena, respectively.

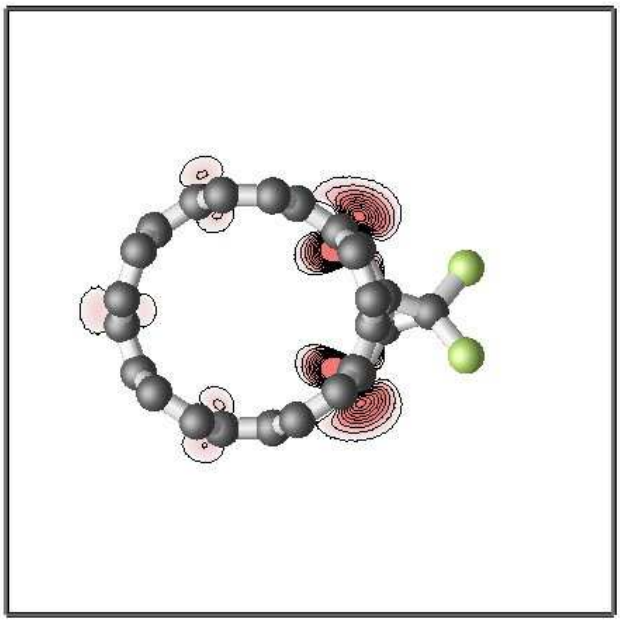

Figure 5.11: Density difference plots for (5,5) CNT functionalized with CCl_2. The density difference is taken as the functionalized CNT minus that of the clean CNT. The red isodensity lines represent a charge transfer from the CNT.

For both cases we calculated the electronic charge density of the functionalized CNT, ρ_{FCNT}. From this we subtract the charge density of the CNT alone, ρ_{CNT}:

$$\Delta\rho = \rho_{FCNT} - \rho_{CNT} \tag{5.11}$$

We plot $\Delta\rho$ for the (5,5) CNT functionalized with aminophenyl in Figure 5.10 and for the CCl_2 functionalized (5,5) CNT in 5.11. Indeed we see for the electropositive case (aminophenyl) that there is a net accumulation of charge on the CNT backbone – i.e. charge transfer has occurred from the aminophenyl functional group to the CNT. For the the electronegative case (CCl_2) there is less net change of charge on the CNT opposite the functional-group, however there is certainly addition of charge on the functional group.

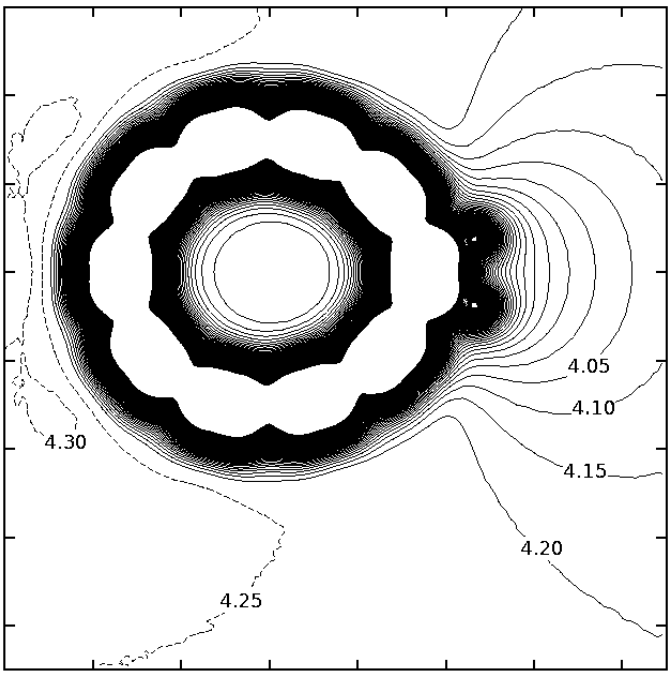

Figure 5.12: The electrostatic potential averaged to the xy-plane for the (5,5) CNT functionalized with two H atoms. The isopotential lines are labeled with their corresponding work function values. The isoline spacing is 0.05 eV. The macroscopic work function for this case is 4.20 eV.

5.5.2 Local Work Function

The local work function can be described as the energy required to extract an electron from the Fermi energy to a point just outside the surface. The local work function provides insight into how the larger electrostatic gradients around the surface details of the material affect the macroscopic work function.

We examine the (5,5) CNT functionalized with two H atoms in the *skw* geometry as the electropositive case. The electrostatic potential averaged to the xy-plane of the unit cell is plotted in Figure 5.12. The isoenergy lines are labeled with their corresponding work function values, such that the vacuum energy is set to zero and the iso-work function vales are determined as:

$$\Phi_{Local} = V_{Local} - E_F. \tag{5.12}$$

The dipole that the addition of the two hydrogen atoms induce across the CNT is clearly visible. Analysing the local work function we see a region of higher work function (relative to the macroscopic work function) is present on the side of the CNT opposite the functional group. While surrounding the functional group (the bonded hydrogen atoms have donated charge to the CNT) there is a lowered work function.

Similarly, we examine the (5,5) CNT functionalized with CBr2 in the *skw* geometry as the electronegative case. Plotted in Figure 5.13 is the electrostatic potential of the functionalized CNT. Again the induced dipole is clearly visible, however for this case the side of the CNT opposite the functional group represents the region of lower work function. analysing the local work function we see the region surrounding the functional group has peaks of very high work function (relative to the macroscopic work function).

5.5.3 Changes in Density of States

As a final analysis of the effects of functionalization we look at the changes induced in the density of states (DOS). Again we use the (5,5) CNT functionalized with 2H atoms and the (5,5) CNT functionalized with CBr_2 as an electropositive and electronegative examples, respectively. The DOS for these two cases along with the pristine (5,5) CNT are plotted in Figure 5.14. The Fermi energy is plotted in all three cases referenced to the vacuum potential (V=0) – i.e. the magnitude of the Fermi energy is the work function. From the figure we see that the electropositive chemical functionalization introduces some localized states above and below the Fermi energy, while the electronegative functionalization opens up to small energy gaps above and below the Fermi energy.

The changes in DOS in these cases differ from the metal intercelated CNT study mentioned in the introduction [122]. Where it is seen the the valence bands of the CNT remain unchanged and the Fermi energy of the intercelated system is forced into

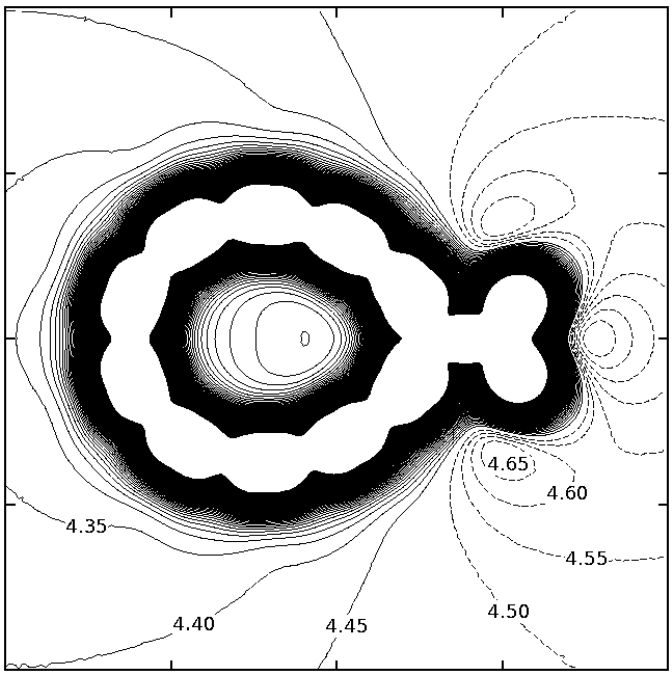

Figure 5.13: The electrostatic potential averaged to the xy-plane for the (5,5) CNT functionalized with $C(Br)_2$. The isopotential lines are labeled with their corresponding work function values. The isoline spacing is 0.05 eV. The macroscopic work function for this case is 4.45 eV.

the conduction bands of the CNT. Here we see the introduction of localized states as a result of the covalent bonding. Ultimately it seems that prediction of changes in work function due to changes in the density of states is not clear.

5.6 Summary

We have shown that the work function of the (5,5) CNT and (8,0) CNT can be changed through the chemical addition of functional groups. The changes in work function range from ± 0.36 eV with respect to the pristine case. We attribute these changes to charge rearrangement (transfer) in the systems and the effect that such a rearrangement has on the electrostatic potential of the CNT. We find that functionalizations that are electropositive or electronegative in nature tend to lower or raise the work function, respectively.

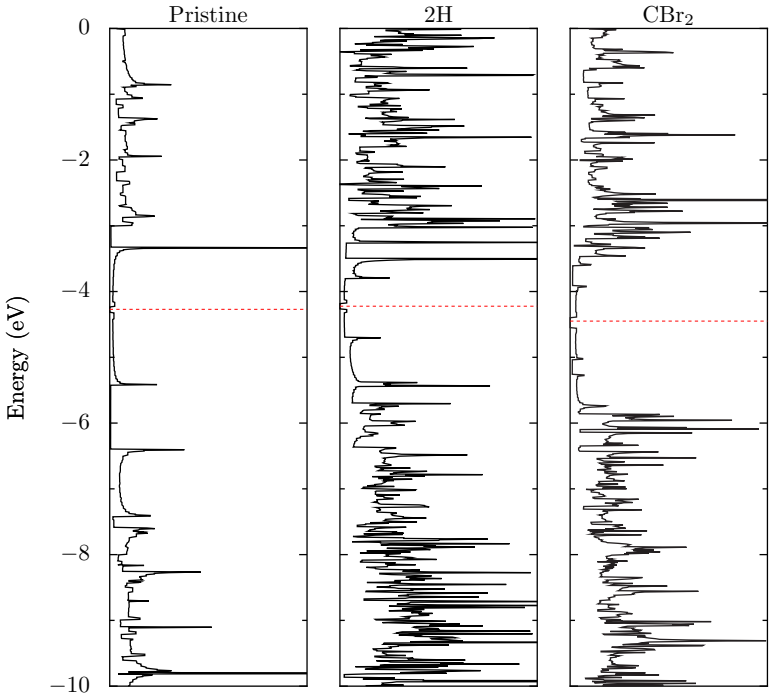

Figure 5.14: The density of states (DOS) plotted for the pristine (5,5) CNT (left), and the (5,5) CNT chemically functionalized with 2H atoms (center) and a dibromocarbene (right). The Fermi energy is plotted in each and reference to the vacuum potential (V=0).

Chapter 6

Schottky Barrier Junctions

6.1 Introduction

Many modern transistors devices rely on a metal/semiconductor contact. The electronic structure at this interface is of fundamental importance to the performance of these devices, and one of the crucial parameters of such an interface is the Schottky barrier height (SBH). SBH is a measure of the energy mismatch across the interface between the Fermi energy of the metal and the majority carrier band edge of the semiconductor. A metal/semiconductor junction that shows rectifying current-voltage behavior, as seen in Fig. 6.1, has a voltage barrier to overcome for current to flow.

In this chapter we explore what controls the SBH in CNT/metal systems. More specifically, we investigate the Schottky barrier that occurs between a close-packed metal (Al and Pd in this study) and a semiconducting (8,0) CNT. This chapter uses the calculations and insights of previous chapters (i.e. the metals of Chapter 4 and the CNTs of Chapter 5) to setup and execute the larger calculations needed to investigate CNT/metal interfaces. We first provide a definition of the SBH and a literature review including both experimental work and first-principles modeling approaches. The final sections detail the methodology of potential-profile lineups,

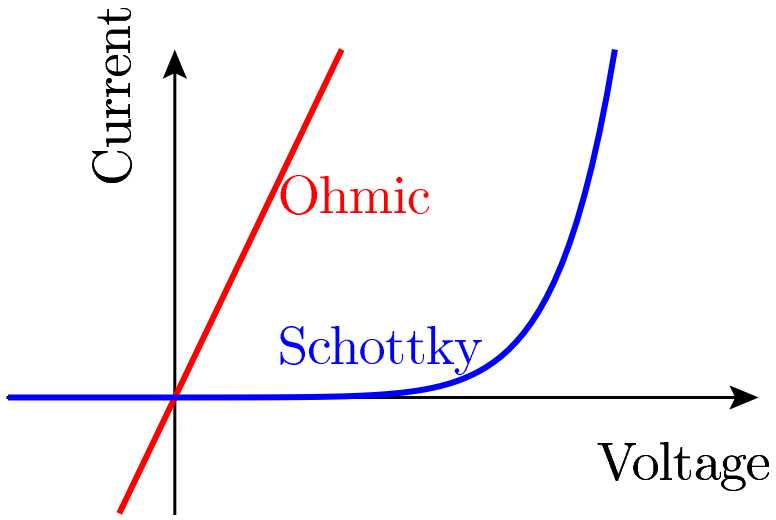

Figure 6.1: A schematic of Ohmic and Schottky (Rectifying) current-voltage characteristics.

present results, and discuss the results using charge transfer and projected density of states analyses.

6.1.1 Schottky Barrier Height

The concept of a rectifying junction has existed since the late nineteenth century. Schottky conducted his studies in the 1920s, yet the factors controlling the SBH are still not fully understood. The Schottky junction between a metal and semiconductor shows rectifying current-voltage characteristics, Figure 6.1. The Schottky barrier height (SBH) is thus a measure of the voltage barrier to transport of the majority carrier in such junctions.

The fundamental principle that leads to a SBH is the equilibration of the Fermi level across the two systems leading to a "bending" of the majority carrier band. The two basic types of SBH that can arise from a metal/semiconductor contact are characterized as either n-type or p-type, depending on whether the majority carrier in the system is either electrons or holes, respectively. The 'SBH can be described by the Gedenkan experiment of Mott [135] and Schottky [136]. The Mott-Schottky

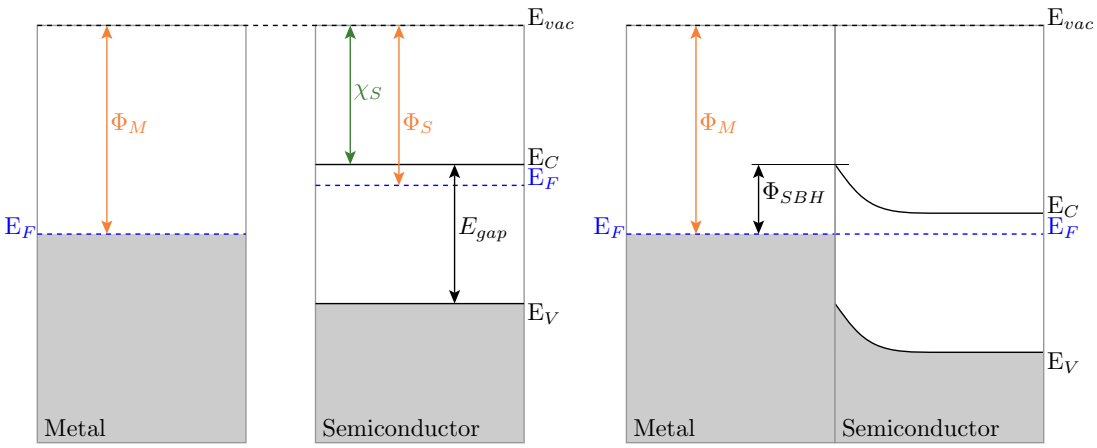

Figure 6.2: The Mott-Schottky model diagram for a n-type Schottky barrier. (left) A schematic band diagram of a metal and semiconductor such that the metal work function is larger. (right) The formation of the Schottky barrier as the two materials are brought into contact.

model is a generalization to the case where the junction is formed perfectly (i.e. no other effects such as Fermi-level pinning are taken into account); however it is still useful to understand this limiting case.

The n-type barrier occurs when the work function of the metal, Φ_M, is larger than the work function of the semiconductor, Φ_S. Note that we adopt the convention that the work function of the semiconductor falls in the center of the gap or in the case of n-type or p-type doping, closer to the conduction band or valence band, respectively. For this case, the barrier is then the offset of the work function of the metal and the conduction band edge of the semiconductor (also referred to as the electron affinity, χ_S), Figure 6.2,

$$\Phi^n_{SBH} = \Phi_M - \chi_S. \tag{6.1}$$

Here the values for Φ_M and χ_S are taken from the isolated bulk systems. This represents a barrier to transport of the majority carrier, electrons.

Similarly, the p-type barrier occurs when the work function of the metal is less than the work function of the semiconductor. For this case, the barrier is the offset of the work function of the metal and the valence band edge of the semiconductor,

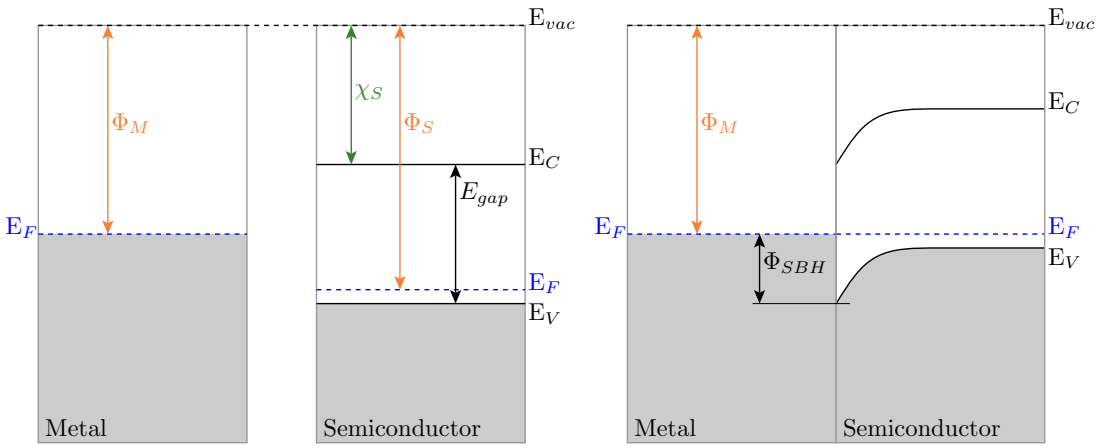

Figure 6.3: The Mott-Schottky model diagram for a p-type Schottky barrier. (left) A schematic band diagram of a metal and semiconductor such that the metal work function is larger. (right) The formation of the Schottky barrier as the two materials are brought into contact.

Figure 6.3. The valence band edge can be taken as the sum of the electron affinity and the band gap of the semiconductor, E_{gap},

$$\Phi^{p}_{SBH} = (\chi_S + E_{gap}) - \Phi_M. \tag{6.2}$$

Again, the values for Φ_M and χ_S are taken from the isolated bulk systems. This represents a barrier to hole transport.

Figures 6.2 and 6.3 are meant to be visual guides to the formation of the Schottky barrier at an interface. In both cases, the extent of the band bending and formation of a charge depletion region will depend on the extent of the charge transfer across the interface.

6.2 CNT/metal contacts

As discussed in Chapter 1, we are approaching the fundamental size limits in the current Si-based transistor technology. Carbon nanotubes (CNTs), discussed in Chapter 5, have excellent and rather unique electronic properties that make them a promising

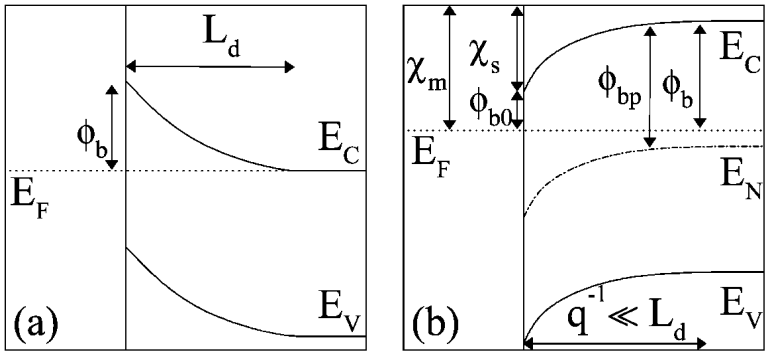

Figure 6.4: Image adapted from Ref. [137]. A schematic band diagram showing band energies and Fermi level as a function of distance from the interface. (a) Band bending on a larger scale of the depletion width, L_D of a heavily n-doped CNT. (b) Close up of interface showing band bending due to MIGS, length scales on the extent of the dipole region $q^{-1} << L_D$.

material to replace Si-based technologies. While CNT based devices are intriguing, there are many practical barriers to implementation. For most proposed devices that incorporate CNTs, there is a need to connect the nanotube to the another material, most likely a metal. It is at this CNT/metal interface where Schottky barriers can form.

6.2.1 Experimental and Numerical Studies

The potential use of carbon nanotubes in electronic devices has led to intense and extensive experimental and numerical studies over the last decade. While these studies are far too numerous to explain in depth here, we can focus the discussion specifically on advancements in understanding in Schottky barriers in CNT/metal and CNTFET systems.

The numerical studies of Léonard and Tersoff cover many of the fundamental properties of CNT and CNT/metal contacts. Of particular interest are the studies that elucidate the length scales of electrostatics in CNTs [139] and the role of Fermi-pinning at the interface [137]. They begin with the same general principle expressed

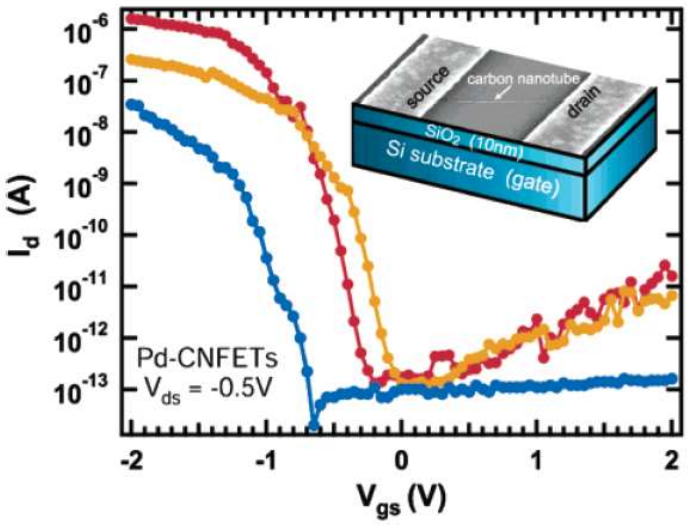

Figure 6.5: Experimental I-V characteristics of CNT/metal junction. Image adapted from Ref. [138]. Current, I_d, versus gate voltage, V_{gs} for a drain voltage of $V_{ds} = -0.5$V. The three lines represent three CNT/Pd system fabricated as in the inset figure. Not the variation in the quantitative behavior of all three devices.

in Eqn. 6.1, such that the Schottky barrier is described as:

$$\Phi_{b0}^{n} = \Phi_M - \chi_S, \tag{6.3}$$

where Φ_M is the metal work function and χ_S is the electron affinity of the semiconductor. They state that due to the metal induced gap states (MIGS) at the interface (and the image charge the MIGS generate in the metal) a surface dipole, D, will form. This raises or lowers the SBH:

$$\Phi_{b}^{n} = \Phi_{b0}^{n} + D. \tag{6.4}$$

However, in CNTs the reduced dimensionality reduces the electrostatic screening. Thus, they take a more microscopic approach to the SBH, modeling the dipole as a charge:

$$\sigma(z) = D_0(E_N - E_F)e^{-qz} \tag{6.5}$$

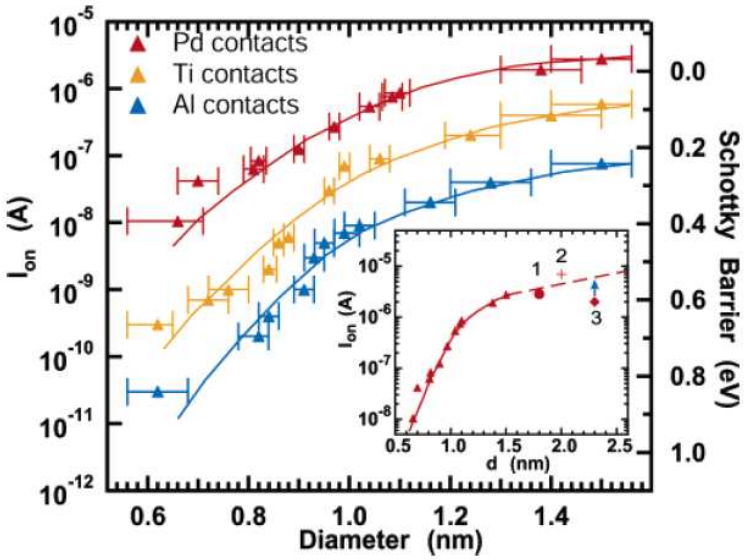

Figure 6.6: On-current voltage and Schottky barrier height versus CNT diameter for CNTs in contact with the metals Pd, Ti, and Al. Image adapted from Ref. [138].

where E_N is the charge neutrality level (the level which no surface dipole would exist) and q represents an approximate average value of the charge from all of the states. In Figure 6.4 the band bending on the scale of the depletion width, L_D, is seen for a heavily n-doped CNT in contact with a metal (panel (a)), while the microscopic picture (b) shows the details at length scales on the order of the influence that the dipole would have, $q^{-1} << L_D$. Here we see the effects that the interfacial dipole has on the alignment of levels. The results of their model show that the bending of the conduction band as a function of distance from the interface, for both high and low work function metals, approaches that of a CNT/metal interface that has no dipole at larger distances.

The main conclusion of Léonard and Tersoff in Ref. [137] is that the decay of the surface dipole is rapid enough that the barrier at the interface will only pose a small tunneling barrier to charge transport. This is illustrated by these figures and supported by the current-voltage calculation they perform (using the Landaur-Büttiker formalism). They find that the entire I-V curve behaves like that expected

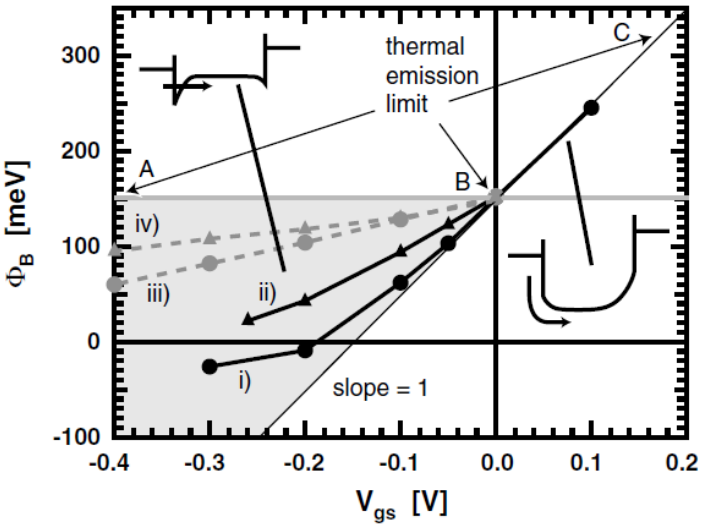

Figure 6.7: Adapted from [141]: Barrier height as evaluated assuming thermal emission theory as a function of V_{gs} for various FETs. (i) $m^* = 0.1m_0$, $t_{ox} = 2nm$, and $t_s = 1.4nm$, (ii) $m^* = 1.0m_0$, $t_{ox} = 2nm$, and $t_s = 1.4nm$ (iii) $m^* = 1.0m_0$, $t_{ox} = 10nm$, and $t_s = 1.4nm$ (iv) $m^* = 1.0m_0$, $t_{ox} = 10nm$, and $t_s = 5nm$.

for the un-pinned barrier height [137].

Taking these numerical studies into consideration, it is still found through experiment that the behavior of CNT/metal interfaces is not straightforward. One goal in experimental study is to ensure good contact between a semiconducting CNT and a metal surface – i.e. Ohmic contact. However, even if expected, this never seems to be the case [42, 138]. The more recent work of Javey *et al.* has shown that with some modulation of the surface, Pd contacts can be near Ohmic and more specifically conductance through the CNT channel can be ballistic [140]. In general Pd is found to make excellent contacts due to its high work function and good wetting interactions with CNTs.

Typically the Schottky barrier is not explicitly measured in experimental studies, it is usually used to explain rectifying behavior in the current voltage characteristics. A typical current-voltage (I-V) plot for a CNT/metal junction is found in Figure 6.5. The figure is adapted from Chen *et al.* Ref. [138]. The figure shows the current,

I_d, versus gate voltage, V_{gs} for a drain voltage, $V_d = -0.5$V. Here we see, as is often found in experiments, that the current for hole transport is orders of magnitude higher than that of electron transport, and thus the device is considered to be p-type. The different lines in the figure represent three different CNT/Pd devices that have been fabricated in the same manner. The fact that the on-current for the three devices can differ by almost two orders of magnitude, illustrates a persistent problem in experimental studies of CNTFETs. It is shown in Ref. [138] that the SBH in such devices can be predicted to some extent. With a large sampling of many CNT diameters (0.6 - 1.6 nm) and three metals (Al, Ti, and Pd), they show that the on-current and Schottky barrier height are correlated to the CNT diameter and type of metal, Figure 6.6.

When a FET is constructed from a new material such as a CNT, one of the questions that arises is whether the behaviour will be the same as traditional FET and MOSFET devices. The dominant mechanism to overcome the SBH in conventional systems has been thermal emission, and it has been suggested by Chen *et al.* that the dominant mechanism in CNTFETs is tunnelling [138]. Thus the question becomes, is there a competition between thermionic emission and tunnelling? A more recent paper by Appenzeller *et al.* [141] shows that at flat band conditions ($V_{gs} = 0$) the only possibility for carrier injection is thermal activation over the Schottky barrier. While the application of any negative gate voltage gives a smaller effective SBH due to tunneling [141]. The authors show the transition between tunneling and thermal emission, and show what effect the thickness of the oxide, the width of the channel, and the effective mass can have on charge injection in CNTFETs. Finally they predict that a semiconducting CNT on Ti should have a barrier to hole transport of $\Phi_B \approx 0.36 \pm 0.04$ [141]. Figure 6.7 shows that increasing the oxide thickness within the device causes the SBH crossing behavior to approach the thermal emission limit.

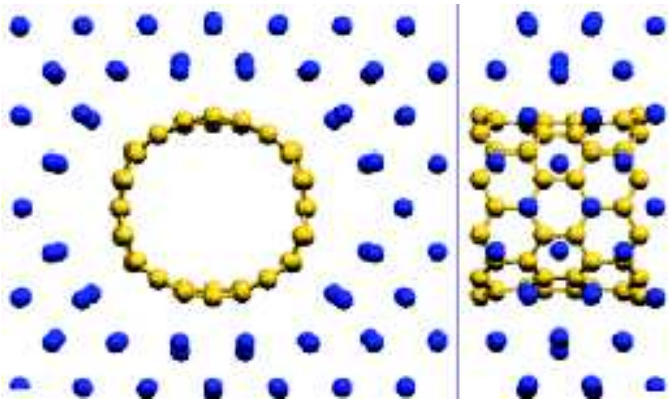

Figure 6.8: A (10,0)CNT embedded in Pd. Image taken from Ref. [142].

6.2.2 DFT Studies

The computational studies that explore CNT/metal contacts are few enough that the general parameters of the calculations are summarized in Table 6.1. The table shows the contact geometry type, metal surface, number of layers, and type of CNTs for a number of studies found in the literature. Although, these are not the only parameters that would determine the results of the calculation, this table gives a relatively good idea of the diversity of systems that have been subjects of previous studies.

The four geometries indicated in the table are characterized by where the CNT is located. The *top* geometry refers to the case where the CNT is placed across the surface of the metal, and in these cases the metal is taken as an infinite 2D slab and the CNT is infinite in 1D. The *between* geometry is similar to the *top*, except that the vacuum region between the CNT and the periodic image of the metal slab is reduced such that the CNT is "sandwiched" between the two metal surfaces. The *embedded* geometry refers to the case where the CNT is entirely surrounded by the metal (i.e. no vacuum region), while the *ring* geometry contains a ring of metal surrounding the CNT. The top geometry can be seen in Figure 6.12 and the embedded geometry can be seen schematically in Figure 6.8. There are also geometries in which the longitudinal axis of the CNT is oriented normal to the metal surface, however as in

Table 6.1: A summary of CNT/metal junctions that have been studied with DFT in the literature; geometry of the contact, type of surface, number of slab layers, type of CNT, and EX-functional are provided.

Contact	Metal	Layers	CNT	note	Ref.
Top	Au(100)	5	(8,0)	PW91	[145]
	Mo(110)	5	(8,0)	PW91	[145]
	Au,Pt,Pd(111)	5	(8,0)	LDA	[128]
	Au,Pt,Pd(100)	5	(8,0)	LDA	[128]
	Al(100)	7	(10,0)	LDA	[146]
	Ca(100)	5	(10,0)	LDA	[146]
	Al(111)	3	(10,0)	PBE, O adsorption	[147]
	Au(111)	3	(10,0)	PBE	[147]
	Au(111)	3	(10,0)	PBE	[148]
Between	Au(100)	5	(8,0)	PW91	[145]
	Mo(110)	5	(8,0)	PW91	[145]
	Au(111)	3	(10,0)	PBE, Pressure effects	[148]
Embedded	Pd	-	(8,0)	PW91	[142]
	Pd	-	(10,0)	PW91	[142]
Ring	Pd	-	(8,0)	PW91	[149]

Refs. [143, 144] these studies are typically focused on lead-conductor-lead transport calculations.

The metal surface in all of the cases (with the exception of the embedded CNT and ring geometries) is taken to be a clean low-index surface, with Miller indicies of either (100), (110), or (111). These previous studies use both LDA and GGA exchange-correlation functionals, and it is noted that the more recent studies use GGA.

The calculated Schottky barrier height (SBH) and some comments from the authors are summarized in Table 6.2. The SBHs are found for numerous CNT-metal contacts. These SBH values are presumably *p*-type, where the barrier height is the difference between the system Fermi energy and the valence band edge of the semiconductor, as described in Ref. [128]. There are not many reported calculated values of SBH, and many of them appear in Shan's paper [128]. However, it seems generally accepted that semiconducting tubes, and in particular the surfaces that also have

oxygen on them [147], induce a p-type barrier. Also interesting are the findings of Zhu and Kaxiras [142] for the cases when the CNTs are fully embedded in the metal; in particular that there is no electrostatic or Schottky-type barrier to electron transfer between metal and semiconducting CNT.

A more recent paper by Zhu and Kaxiras [149] more closely models a realistic system using a geometry that includes some part of the CNT that is not covered or in contact with metal – i.e. some CNT that goes through the vacuum region. This study includes a (8,0) CNT with a ring of 32 Pd atoms. The authors show that the local potential surrounding each C-atom levels off to nearly a constant in the vacuum (justifying the use of potential profile line-ups in this case). They report a p-type barrier of ~ 0.4 eV. While the geometry still remains a bit physically unrealistic, the results suggest that the presence of a vacuum region may be important to arriving at the correct physics for the Pd/CNT system.

Finally there are also a few studies that characterize the influence of other factors. Park and Hong [147] investigate the effect that oxygen adsorption on the surface of Al has on SBH. The authors find the the O adsorption increases the work function of the Al surface and effectively creates a similar SBH to that of the CNT/Au(111) system. Park *et al.* [148] investigates the effects of pressure on the junction. In this case pressure is simulated by moving the 'bottom' of the slab close to the 'top' of the CNT (taking advantage of the periodic boundary conditions in the direction normal to the metal surface). The authors find Fermi level goes from being pinned at the valence band edge to the conduction band edge.

6.2.3 Applying the Mott-Schottky Model

As a first approximation, we apply the model of Mott and Schottky discussed earlier in this chapter, Figures 6.2 and 6.3, to the CNT/metal interfaces studied here. We reconstruct the figures using some of the DFT results from Chapters 4 and 5, namely the work function and band edges of the clean (8,0) CNT and the work functions of

Table 6.2: Schottky barrier heights are found for numerous CNT-metal contacts found in the literature.

Contact	Schottky barrier (eV)	Comment	Ref.
Au(111)/(8,0) CNT	0.23	highly orientation dependent	[128]
Au(100)/(8,0) CNT	0.42	highly orientation dependent	[128]
	'small'	weak coupling of electronic states	[145]
Mo(110)/(8,0) CNT	0.4	strong electronic coupling	[145]
Pd(111)/(8,0) CNT	0.26		[128]
Pd(100)/(8,0) CNT	0.15		[128]
Pd(ring)(8,0) CNT	0.4		[128]

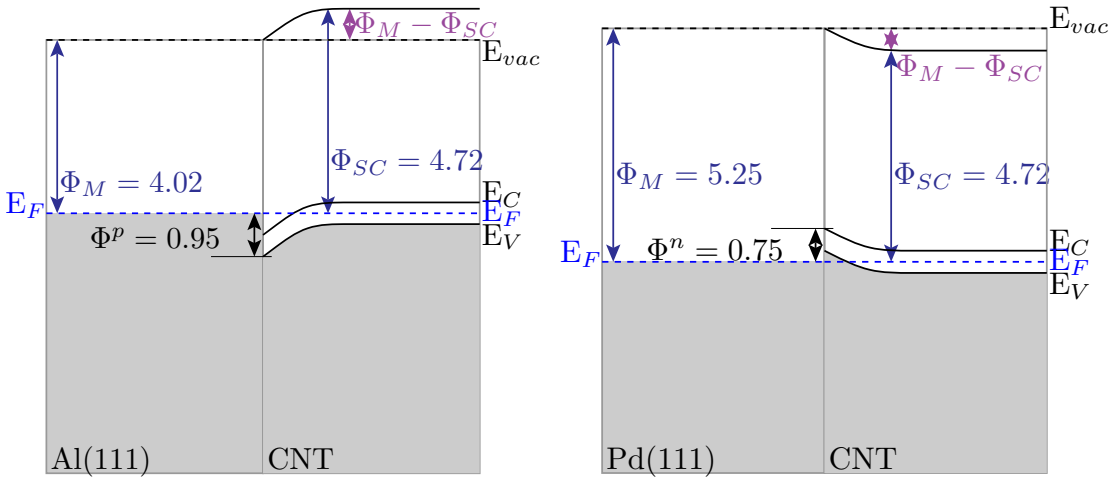

Figure 6.9: The Mott-Schottky model as applied to (left) the CNT on Al(111) and (right) the CNT on Pd(111). In both cases, the shift applied to the bands in the bulk semiconductor are due to the equilibration of the Fermi energies, and the magnitude of the shift is the difference in Fermi energies levels, $\Phi_M - \Phi_{SC}$

the Al(111) and Pd(111) surfaces, Figure 6.9.

From the work function values we see that the Fermi energies of both metals are outside the band gap of the semiconductor. The CNT/Al(111) becomes a system that is likely Ohmic, while the CNT/Pd(111) system shows the opposite effect having a large n-type barrier. However, we know that this is not the case for the experimental studies discussed previously, and as expected there is more involved with the lineup of these materials than just the alignment of the Fermi energy. The following sections outline the methodology and discuss the result for a DFT calculation of SBH in

CNT/metal systems.

6.3 Methodology

This study was performed with the DFT methodology as described in Chapter 2. Both the LDA and PBE exchange-correlation functionals are used. All of the pseudopotentials used here are discussed in previous chapters. Furthermore, all of the structures investigated here are fully relaxed, however, the size of the structures makes full relaxation with a dense k-point mesh prohibitive. The choice of a special **k**-point was made with the reciprocal lattice coordinates of $(\frac{1}{4}, \frac{1}{4}, \frac{1}{4})$ in crystal units, see Appendix D for more information. The remaining methodology sub-sections discuss the different methods used for the calculation of the Schottky barrier heights, namely potential profile lineups.

6.3.1 Potential Profile Lineup

One way to determine the SBH from first-principles is known as the potential profile lineup. This methodology is commonly used for DFT studies with periodic boundary conditions – e.g. plane wave basis sets, etc., discussed in Chapter 2.

In the previous sections we determined that the SBH was the offset of the Fermi energy of the metal, E_F, and either the valence band, E_V, or conduction band edge, E_C of the semiconductor, as expressed in Eqns. 6.1 and 6.2. The difficulty arises in determining how to represent these two values properly with respect to each other and the interface given the limitations that the periodic boundary conditions impose. Most importantly, these band energy terms must be chosen such that they are outside the interfacial region in which the charge density is different from that of the respective bulk system yet not exceeding any band bending length.

Calculation of the SBH can be expressed as the sum of two terms: The band structure contributions and the lineup of the electrostatic potentials, for the p-type

case this is

$$\Phi^{p}_{SBH} = [E_F - \langle V \rangle_M]^{bulk} - [E_V - \langle V \rangle_S]^{bulk} + [\langle V \rangle_M - \langle V \rangle_S]^{interface}, \tag{6.6}$$

where the $\langle V \rangle$ terms in the bulk systems refer to the average electrostatic potential in each respective system. The average electrostatic potential can be taken as

$$\langle V \rangle = V(\mathbf{G} = 0). \tag{6.7}$$

Thus, the band structure terms E_F and E_V are included in the calculation of SBH with respect to these electrostatic potentials. However, it is noted that these potentials are ill-defined. This arises from solving the the Poisson equation in reciprocal space. In real space, the Poisson equation is

$$\nabla^2 V(\mathbf{r}) = 4\pi\rho(\mathbf{r}), \tag{6.8}$$

which, for the periodic systems we are typically interested in studying wit plane wave basis sets, this is more conveniently solved in reciprocal space as

$$V(\mathbf{G}) = \frac{4\pi}{|G|^2}\rho(\mathbf{G}). \tag{6.9}$$

In this equation, the potential at $\mathbf{G} = 0$ is taken to be zero.

In the last term of Eqn. 6.6, while the two average electrostatic terms on either side of the interface are ill-defined, the difference between them is not. This difference is the interfacial dipole, $\Delta V^{interface}$ that forms

$$\Delta V^{interface} = [\langle V \rangle_M - \langle V \rangle_S]^{interface}. \tag{6.10}$$

The electrostatic potential that we obtain is periodic, and oscillatory reflecting the layered structures of the metal and the semiconductor. Note, when the semiconductor

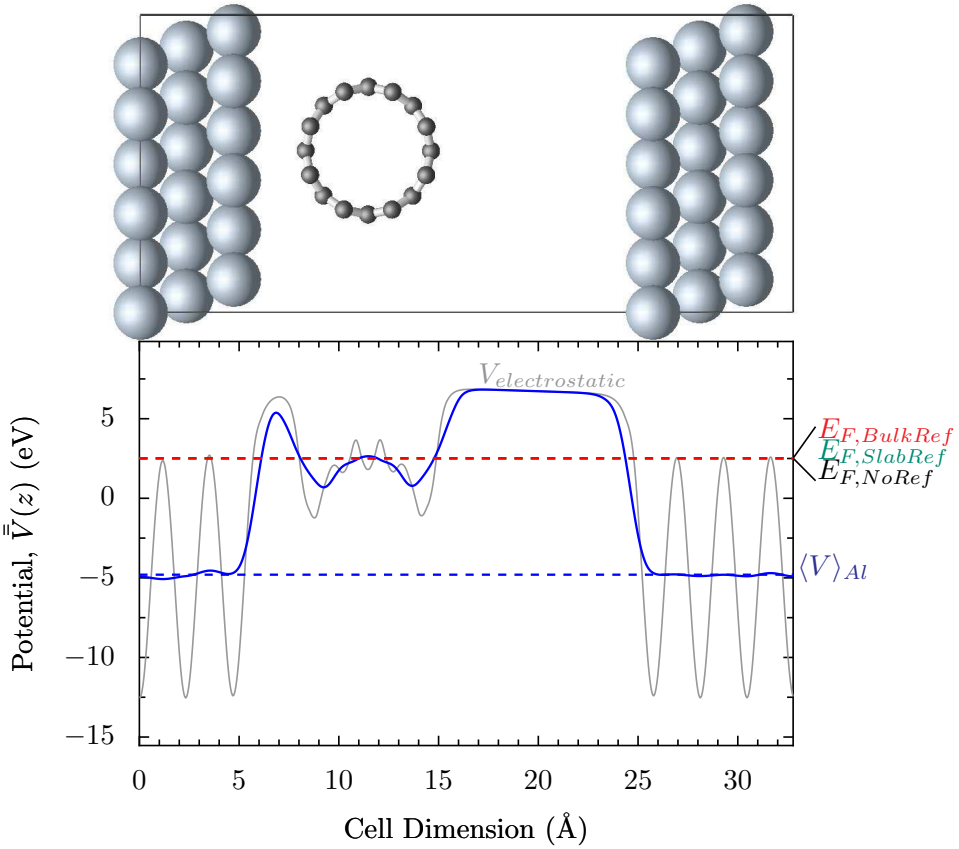

Figure 6.10: Gray Line: The electrostatic potential of the CNT on Al(111) system, averaged to the z-axis. Blue line: The macroscopic average of the potential with a sampling window set to the layer spacing of the Al(111) slab. Red line: Fermi levels aligned from different reference systems.

is not a 3D periodic solid, for example a 1D CNT, we have a slightly different case; this will be discussed in the next section. The oscillating potentials can be smoothed to find the average using the technique of macroscopic averaging discussed in Appendix A,

$$\overline{\overline{V}}(z) = \frac{1}{\alpha}\int_{z-\frac{\alpha}{2}}^{z+\frac{\alpha}{2}} \overline{V}(z')dz' \tag{6.11}$$

where $\overline{V}$ is the planar average of the potential. We find the average for two different windows, α; one that reflects the layer spacing of the metal, and one that reflects the layers spacing of the semi-conductor. The interfacial dipole $\Delta V^{interface}$ can then be obtained using Eqn. 6.6

Averaging around an Atom

We know that the CNT will not always be periodic normal to the interface, and therefore macroscopic averaging will not always be possible. This is illustrated in Figure 6.10 where the electrostatic potential is plotted for the CNT on Al(111) surface (this geometry are discussed in more detail in later sections). A macroscopic average of the potential $\overline{\overline{V}}(z)$ is also plotted. Here the averaging window α has been taking as the layer spacing of the Al(111) slab. This yields a good value for the average potential within the metal $\langle V \rangle_{Al}$. However, no averaging window α will give a good value for the average potential in the CNT. Thus, we have to determine a potential reference using a different method. . In a similar manner to the line-up of the average potential $V(\mathbf{G} = 0)$, we can use the average electrostatic potential of a much smaller volume of the system. One can choose the volume centered at one carbon atom far from the interface and find the average potential within that volume. Working with numerical grids makes choosing a cubic volume centered on a C atom a convenient choice, where the average can be taken over the grid points in the volume:

$$\langle V \rangle_C = \frac{1}{N^3} \sum^{N} \sum^{N} \sum^{N} V(x, y, z), \tag{6.12}$$

where N is the number of grid points to a side of the cube. In this manner we can calculate both $\langle V \rangle_C^{interface}$ and $\langle V \rangle_C^{bulk}$. Furthermore, introduction of numerical errors can be avoided through the use of exactly matching numerical (FFT) grids for the separate calculations of the interfacial and bulk CNT systems.

6.3.2 Projected Density of States

Park and Hong [147] use a method for determination of the SBH that utilizes the projected density of states (PDOS). In this method they use the PDOS to locate the bottom of the conduction band and the top of the valence band for n-type and p-type SBH respectively. The Fermi energy in this case is taken directly from the whole

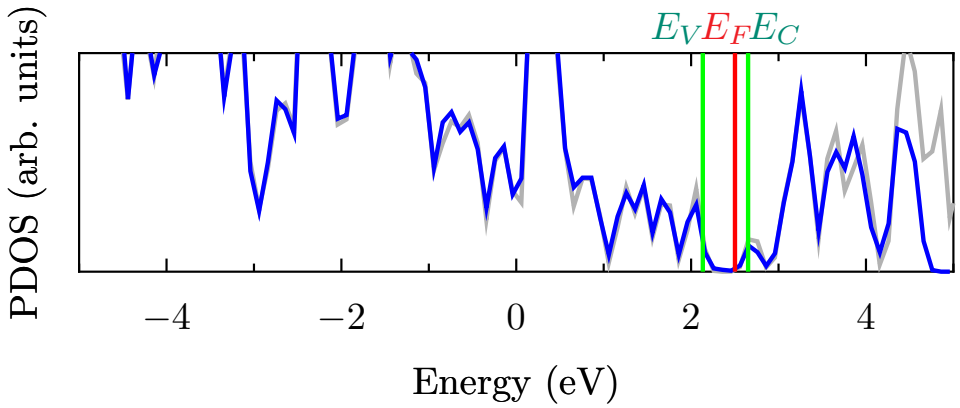

Figure 6.11: Blue: The PDOS for the CNT/Al(111) system projected onto a single carbon 2p-state. Gray: The PDOS for the same 2p-projection of the isolated CNT. Green: The valence and conduction band energies taken from a band structure calculation of the isolated CNT. Red: The Fermi energy taken from the full system.

calculation.

Similarly we can use the PDOS to visualize the energy shift applied in the potential profile line-up. This shows showing that the conduction band and valence band edges of the CNT, taken from a band structure calculation of the isolated CNT line-up with similar features in the PDOS projected on the 2p-states of a carbon atom that is sufficiently far away from the interface. We demonstrate that this is the case with the PDOS for a C-atom in a case where the CNT is in contact with Al, Figure 6.11. In the figure, the band edges of the isolated CNT (in green), line up well with the same features of the PDOS. Note, this case will be discussed in much more detail in the following sections, but is used here to illustrate the line-up of the the E_C and E_V from the isolated CNT with the feature in the PDOS. The Fermi energy is taken from the full CNT/metal system (also discussed in more detail later).

The prospect of using the PDOS to line-up the band energies in a robust way is intriguing, but can be prone to error. The bands of the CNT can split, especially in cases where strong chemical bonds for between the metal and the CNT. This is discussed further in Appendix E.

6.4 The Top Geometry

We initially study a system similar to that of the previous studies [145, 128, 146, 147, 148] discussed in Table 6.1. Within periodic boundary conditions, this geometry provides the smallest possible junctions with respect to number of atoms and volume of the unit cell. The general geometry is one in which an infinite 1D CNT is placed one the surface of an infinite 2D slab, with a vacuum region in the third dimension that separates this system from its periodic image. This can be done for any metal surface or CNT length, however care needs to be taken to limit the strain in the system from the lattice mismatch between the CNT and the metal.

6.4.1 Lattice Matching

We are interested in the interaction of the (8,0) CNT with the (111) surfaces of Al or Pd. It is necessary to find a commensurate lattice between the CNT and the metal surface, because of the periodic boundary conditions. From Table 4.1 we know that the bulk lattice parameters for Al and Pd are are 4.06 Å and 3.98 Å, respectively[1]. While the minimum unit cell for the relaxed (8,0) CNT contains 32 atoms and is 4.254 Å along the CNT axis.

A likely lattice match lies with orientation of the CNT longitudinally along the [110] direction of the (111) surface of both metals. In Al and Pd this [110] direction has a length of $\sqrt{2}a_0$, or 5.74 Å and 5.63 Å, respectively. If we adopt the convention that the CNT will take the strain in either system, the strain in the CNT would amount to nearly 25% for both metal surfaces. Thus, we must add translational units of both the CNT and metal in order to find a good match. In doing this we find that the closest match for both cases is to have two units of the (8,0) CNT and one and one half units of either metal. For the Al(111) surface this leads to a strain of $(8.61/8.51 - 1) * 100 = +1.20\%$, while for the Pd(111) surface the strain in the CNT

[1]DFT values for PBE and the ultra-soft pseudopotentials used in this study

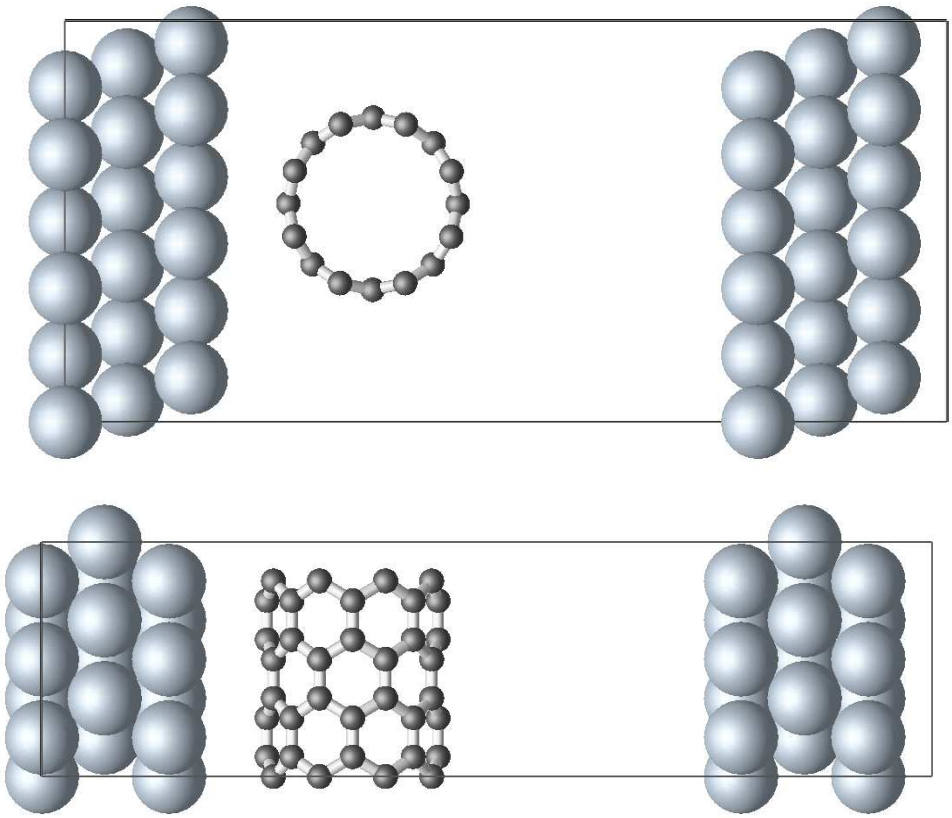

Figure 6.12: Unit cell of top geometry for (8,0) CNT on six layers of Al(111). Top panel: The unit cell looking down the longitudinal axis of the CNT. Bottom panel: The unit cell normal to the longitudinal axis of the CNT.

is $(8.445/8.51 - 1) * 100 = -0.74\%$. It should also be noted that other directions on the (111) surface were considered, however the [110] crystal direction proved to have the closest match for the smallest possible system in both cases.

This lattice matching leads to a slab surface that is three atoms in length along the close packed [110] direction (longitudinally with the CNT). Furthermore, the slab surface is six atoms in width along the less packed direction, this is done to sufficiently accommodate the width of the CNT, and to ensure that the CNT does not interact spuriously with its periodic images. Thus the system has 18 metal atoms per layer and 64 carbon atoms for the CNT.

Finally, the (111) surface are stacked such that they follow a ABCABC stacking

pattern as is found in FCC metals. The layer spacing is initially set to the equilibrium bulk spacing of $a_0/\sqrt{3}$. Recall from Chapter 4 that the layer relaxation for the (111) surfaces of Al and Pd is small, $+1.0\%$ and $+0.25\%$, respectively.

Figure 6.12 shows two views of the top geometry for the (8,0) CNT on Al(111) system. The top panel shows the unit cell looking down the longitudinal axis of the CNT. Note, that the six layer Al(111) slab continues on the right side of the unit cell due to the periodic boundary conditions. Centering the slab at the origin is not strictly necessary in this calculation, but led to quicker convergences due to inversion symmetry for the case with no CNT on the surface (Chapter 3), however there are no symmetry elements in Figure 6.12. The bottom panel shows the unit cell normal to the longitudinal axis of the CNT.

6.4.2 Fermi Energy Calculations

It was found in this geometry that the Fermi level of the system is determined solely by the metal. This follows the logic behind the schematics seen in Figures 6.2 and 6.3, where the Fermi level equilibration is what drives the band bending.

We investigate the Fermi level alignment in both the CNT in contact with the Al(111) surface and the Pd(111) surface by three methods to ensure their equivalency. First, through the method of using a strictly bulk reference for the Fermi energy. In this case a one atom FCC bulk unit cell is used to calculate the Fermi energy of the metal. From the same calculation we use the method of macroscopic averages and potential profile lineup to adjust the Fermi level, $E_{F,BulkRef}$, into same frame of reference as the CNT/metal system. The second method is similar, only in this case a slab of the same width is used as the reference. The Fermi energy, $E_{F,SlabRef}$, is aligned in the same manner as the first method. Finally, we take only the Fermi energy as it is computed directly from the CNT/metal system, $E_{F,NoRef}$.

Using these three methods, we can see that they are indeed equivalent for both the Al and Pd surfaces. Figures 6.10 and 6.13 show the three Fermi energies plotted

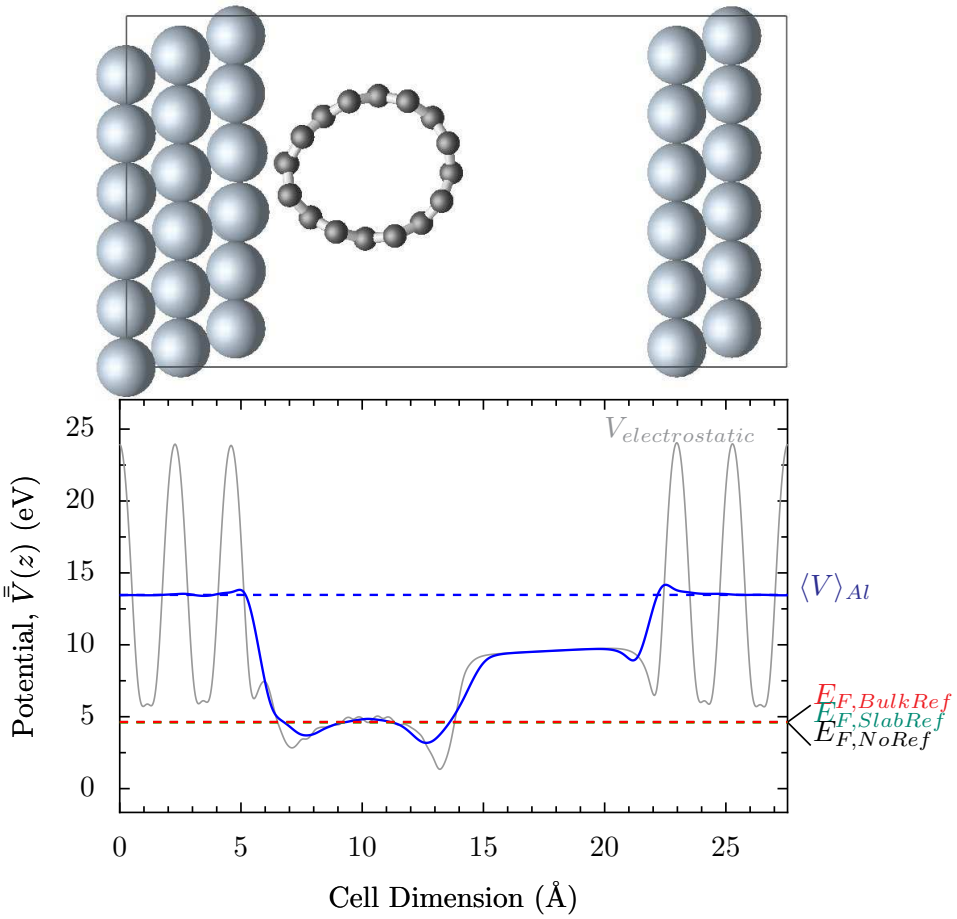

Figure 6.13: Gray Line: The electrostatic potential of the CNT on Pd(111) system, average to the z-axis. Blue line: The macroscopic average of the potential with a sampling window set to the layer spacing of the Pd(111) slab. Red line: Fermi levels aligned from different reference systems.

together for the Al(111) and Pd(111) surface, respectively. In both cases the maximal difference between the Fermi energies calculated with different methods is < 0.02 eV. With this equivalency the potential profile lineup method, Eqn. 6.6 can be simplified knowing that:

$$E_{F,NoRef} \approx [E_F - \langle V \rangle_M]^{bulk} + [\langle V \rangle_M]^{interface}. \tag{6.13}$$

Thus, we can rewrite Eqn. 6.6 as:

$$\Phi^p_{SBH} = E_{F,NoRef} - [E_V - \langle V \rangle_S]^{bulk} - [\langle V \rangle_S]^{interface} \tag{6.14}$$

We can simplify the equation further by referring to the difference in potential of the CNT and it respective isolated (bulk) case as, ΔV_{CNT}:

$$\Delta V_{CNT} = [\langle V \rangle_S]^{bulk} - [\langle V \rangle_S]^{interface} \tag{6.15}$$

Finally we have the p-type potential profile lineup written as,

$$\Phi^p_{SBH} = E_{F,NoRef} - E_{V,CNT} + \Delta V_{CNT} \tag{6.16}$$

6.4.3 SBH Versus Slab Thickness

We are using the slab-supercell approximation to represent a bulk-like system. In particular the metal leads are represented here by a few metal layers (the slab). As we saw in Chapter 4, surface properties of the metals are dependent to some extent on the slab thickness. However, these slab effects are smallest for the (111) surface. It was found that the work functions of (111) surface are well converged at thickness of 4 layers.

Because of the computational cost of performing the calculations for this chapter, we would like to use a small number of slab layers. To that end we calculate the SBH versus the thickness of the (111)Al slab. We calculate the SBH with slab thicknesses of 3 to 6 layers. Figure 6.12 shows the six layer thick slab, and one can obtain the other slab thicknesses through the removal of layers from the side of the slab opposite the CNT. For this study the CNT is relaxed to an optimal geometry. It is found that after only four slab layers the fluctuations in SBH are < 0.008 eV.

6.5 Results: Clean Surfaces

The remaining sections of this chapter are dedicated to applying the previous methods to a number of different CNT/metal geometries, starting from the clean lattice

Table 6.3: The Schottky barrier heights of a CNT on clean Al(111) Pd(111). All values are in eV.

System	Binding E	Φ_{WF}^{Metal}	Φ_{SBH}^{p}	Φ_{SBH}^{n}
Al(111)	-0.17	4.02	0.37	0.16
Pd(111)	-2.96	5.25	0.29	0.21

matched CNTs on Al or Pd (refer to Figure 6.12). Furthermore, analysis and discussion is made through investigation of charge transfer, states at the Fermi energy level, and the projected density of states.

6.5.1 SBH Results

Using the method of potential profile line-up described earlier, we calculate the SBH values for the CNT on the clean metal surfaces. Here we use the energy shift from the line-up of the electrostatic potentials to align the PDOS of a C-atom of the full system with the band-gap edges of the isolated CNT.

The results of the line-up are found in Table 6.3. We find that a *p*-type barrier forms in both the CNT/Al and CNT/Pd systems. The values in the table can be compared with the experimental data that was presented in Figure 6.6 from Ref. [141]. From the figure we see that the barrier in the Al case should be $\approx$ 0.8 eV and in the Pd case should be $\approx$ 0.4 eV. The Pd case gets the value much closer to the experimental values, but it is likely that both are incorrect due to both the underestimation of the band gap by DFT and the ideal geometries used to model the systems.

Figure 6.14 shows the PDOS for the 2p-projections of the labeled carbon atoms moving around the circumference of the CNT (points A $\rightarrow$ E). The values for the conduction and valence bands are taken from the isolated CNT and aligned with the potential line-up at atom-A – i.e. furthest from the CNT/metal interface. The band edges of the CNT are still visible in the PDOS at point A and the band edges from the band structure of the isolated CNT line up well with these features. Moving around

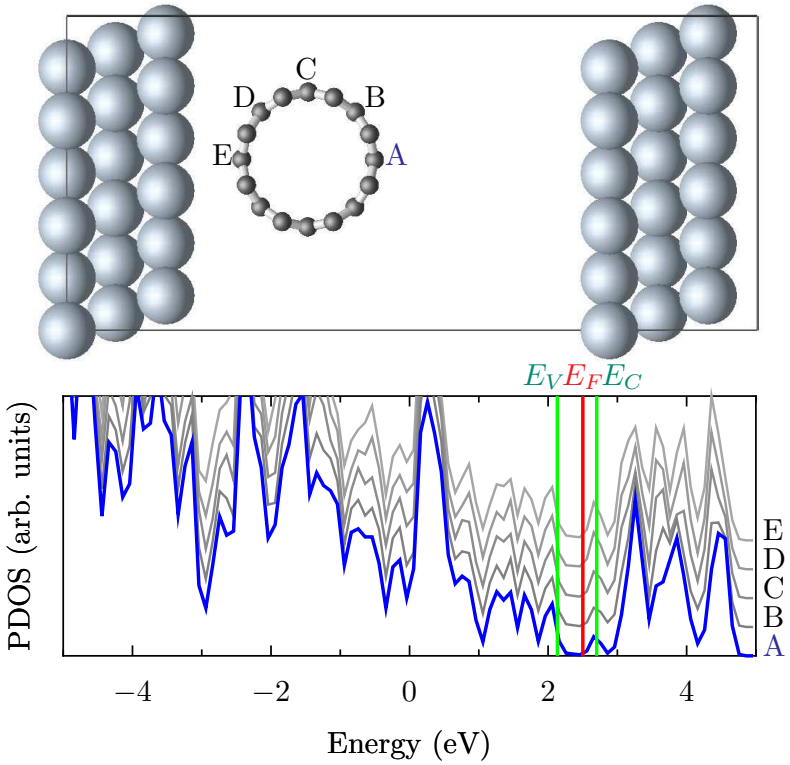

Figure 6.14: PDOS of C atom p-projections moving around CNT on Al(111) from points A to E. An arbitrary shift is applied to subsequent PDOS for clarity.

the CNT, the PDOS does not change much. Note also in the figure an arbitrary y-shift has been applied to the subsequent PDOS for clarity.

Similarly, Figure 6.15 shows the PDOS for the 2p-projections of the labeled carbon atoms in the CNT/Pd(111) system. Here only the PDOS at atom-A show a similarity to the conduction and valence bands of the isolated CNT. Moving around the CNT the PDOS features near the physical junction become more distorted because of the chemical bonding that has formed at the surface.

6.5.2 Charge Transfer

The charge transfer across the interface is calculated from the charge density differences between the full system of CNT on metal and the isolated CNT and metal slabs

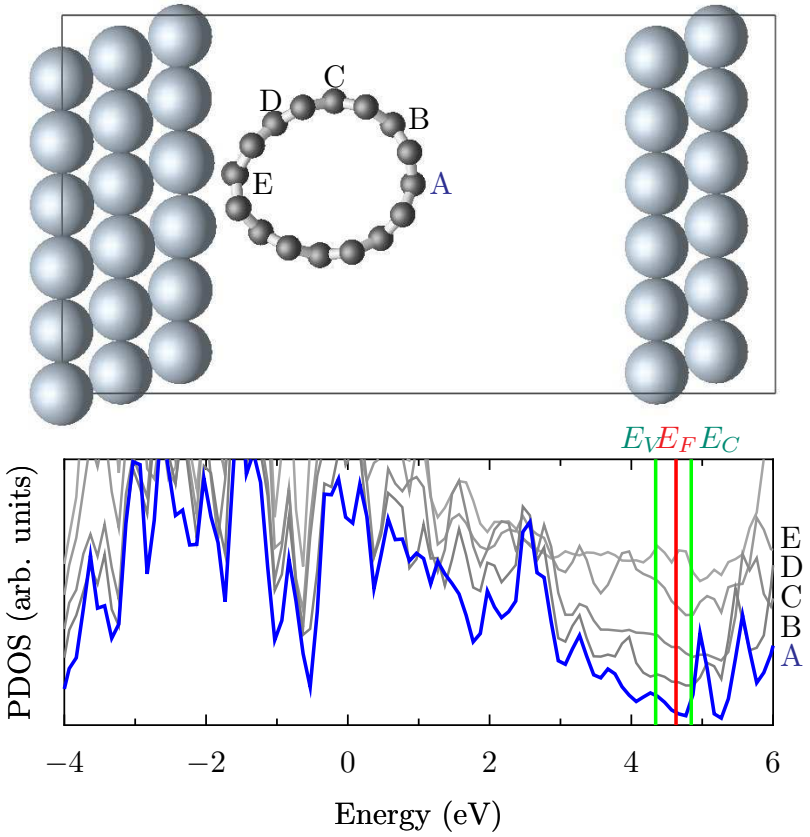

Figure 6.15: PDOS of C atom p-projections moving around CNT on Pd(111) from points A to E. An arbitrary shift is applied to subsequent PDOS for clarity.

systems:

$$\Delta\rho = \rho_{full} - (\rho_{CNT} + \rho_{metal}). \tag{6.17}$$

Figure 6.16 shows the density difference for the CNT/Al(111) system. The top panel is a slice of the isodensity surface, where blue represents the accumulation of charge and red the depletion of charge. The isodensity line is set at $\pm 4 \times 10^{-5}$. The middle panel shows the planar average, $\overline{\rho}(z)$, of $\Delta\rho$ for the entire system along the z-axis. Finally, the bottom panel shows the planar potential generated by the density difference. The potential is calculated using the Poisson equation, $\nabla^2 v(\mathbf{r}) = -4\pi\rho(\mathbf{r})$. Using open boundary conditions and the fact that we have the density difference as a planar average $\overline{\rho}(z)$ – i.e. a 1D function – we can use a 1D solution to the Poisson

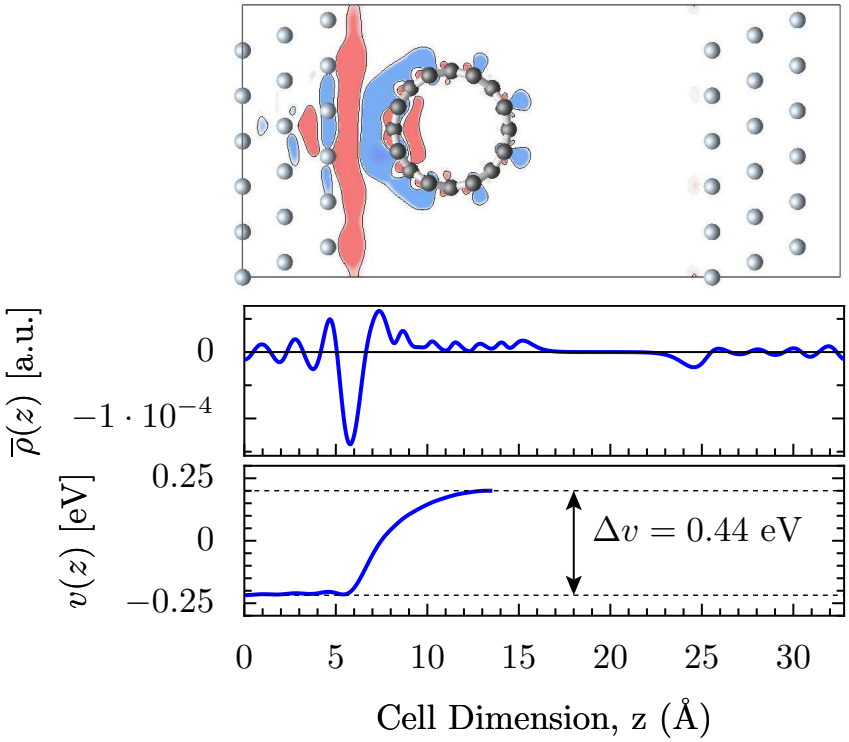

Figure 6.16: Density difference for the CNT/Al(111) system. Top panel: Blue represents the accumulation of charge and red the depletion of charge. The isodensity line is set at $\pm 4 \times 10^{-5}$. Middle panel: Planar average of $\Delta\rho$ for the entire system summed to a single axis. Bottom panel: The potential step across the interface, calculated from the 1D density.

equation:

$$v(z) = -4\pi \int \overline{\rho}(z')|z - z'|dz' \tag{6.18}$$

Note the formation of a surface dipole at the interface. This interfacial dipole formation is akin to the traditional metal-semiconductor contact interfaces. The charge transfer does not distort the CNT, and given the low binding energy, it is likely that the CNT is not chemically bonded to the surface. It is this surface dipole formation that can account for the shifting of the energy levels of the CNT band structure. The dipole in this case is pointing into the metal surface, raising the CNT band energies and effectively lowering the CNT work function. This is similar to the case of electropositive chemical functionalization seen in Chapter 5. However, we do not

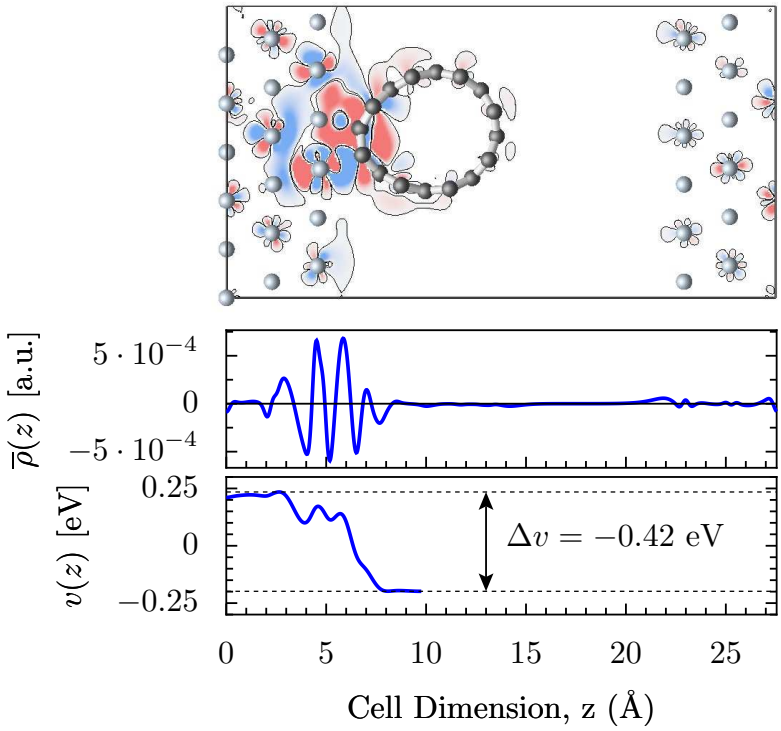

Figure 6.17: Density difference for the CNT/Pd(111) system. Top panel: Blue represents the accumulation of charge and red the depletion of charge. The isodensity line is set at $\pm 1 \times 10^{-4}$. Middle panel: Planar average of $\Delta\rho$ for the entire system summed to a single axis. Bottom panel: The potential step across the interface, calculated from the 1D density.

technically have a planar surface dipole, and in the limit that the spacing between the CNTs and their periodic images becomes very large, the planar surface dipole goes to zero. The case we have is much more localized, as suggested by Léonard and Tersoff [137], where the dipole in our system will likely decay as r^{-3}. Thus it is more likely that the dipole changes the band levels and SBH locally.

Similarly, Figure 6.17 shows the density difference of the CNT/Pd(111) system. Again the top panel is a slice of the isodensity surface, where blue represents the accumulation of charge and red the depletion of charge. The isodensity line is set at $\pm 1 \times 10^{-4}$. The middle panel shows the planar average, $\overline{\rho}(z)$, of $\Delta\rho$ for the entire system. Here it is less clear from both the isosurface and the planar average if there

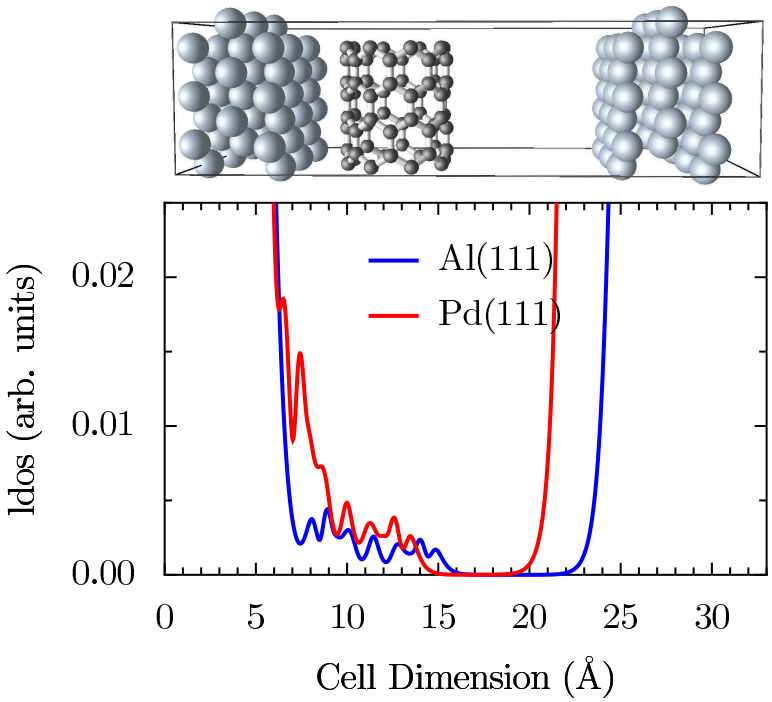

Figure 6.18: Planar average of the DOS at the Fermi level for both the CNT on Al(111) (blue) and Pd(111) (red) systems. Top panel: A schematic of the unit cell as a guide for the feature in the plot below.

is the formation of an interfacial dipole in this system. However the bottom panel showing the potential drop calculated with Eqn. 6.18 shows that a dipole does point out of the metal surface. Opposite the Al(111) case, this dipole lowers the band energies of the CNT, effectively increasing the CNT work function. This is similar to the electronegative chemical functionalizations seen in Chapter 5. Furthermore, from the high binding energy and the rearrangement of charge at the surface, this system has chemical bonding between the CNT and the metal surface, which could account for the good contacts reported experimentally [140].

6.5.3 States Near Fermi Level

Electronic states often form at the metal/semiconductor interface. These states can effectively "pin" the Fermi level of the system. One form, metal induced gap states

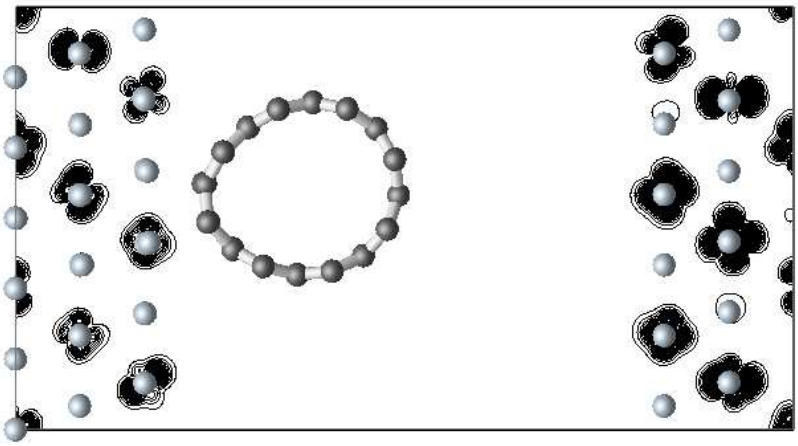

Figure 6.19: A cross section of a $|\psi|^2$ state for CNT/Pd(111) near Fermi level.

(MIGS), results from the tails of the metallic states overlapping into the semiconductor. While another form, deep level traps, are more likely due to impurities in the system.

We first investigate the density of states near the Fermi-level. Figure 6.18 shows the planar average of the LDOS at the Fermi level for the (8,0) CNT on Al(111) (blue) and Pd(111) (red). At this energy level the DOS is dominated by the metal in both systems, evident by the order of magnitude larger DOS on the left and right of the figure (corresponding to the metal slab). However, there are some features visible in both systems on or near the CNT. In particular, there is a peak in the Pd(111) system that corresponds to the physical interface between the CNT and metal surface.

In order to investigate these states further we look at the Kohn-Sham wave functions near the Fermi energy, searching an energy window of $E_F \pm 0.25$ eV in both systems. The 0.5 eV energy window corresponds to 12 bands for the Al(111) case and 45 bands for the Pd(111) case. To visualize these states, we take the square modulus of the Kohn-Sham wave function, $|\psi_{n,\mathbf{k}}|^2$, where n is the band index and $\mathbf{k}$ is the wave vector. We also look at the sum of the states over the range of bands that are in our energy window, $\sum_n |\psi_{n,\mathbf{k}}|^2$.

Figure 6.19 shows the states at one of the bands near the Fermi energy for the Pd(111) case, all of the states for all of the 45 band energies considered had a similar delocalized character. Figure 6.19 represents a slice through the isosurfaces of the plotted state, note the d-like character of the state, this was typical for all of the plotted Pd(111) states near the Fermi energy. Also, no localized states were found in the energy window near the Fermi energy for the Al(111) case. The Al(111) states, as expected, were more delocalized.

The lack of localized states near E_F in these two systems is in agreement with the conclusions in the literature, that MIGS in the CNT on top of the metal will be small [150, 137]. This is especially true for the case of Al where the CNT is only loosely bound, and the tails of the states of the metal will decay significantly before reaching the CNT [137].

6.5.4 Far From the Interface

We can visualize a device in the real world to have a CNT that is not infinitely in contact with the metal. If we consider the region that is in contact to be the interface, we can ask what will the electrostatic barriers look like further from the interface?

We know that the dipole that forms at the interface is not a 2D planar dipole, and thus it will decay with distance from the interface. However, as we saw in the previous sections, the band energies of the CNT are shifted under the influence of the surface dipole. Thus, outside the region of the dipole interaction a different picture will emerge. First, the chemical potential of the CNT and the Fermi energy of the metal will stay in equilibrium. Second, according to Léonard and Tersoff [137], the macroscopic picture (on the scale of the depletion width) is such that the un-pinned barrier is the only one seen. That is to say that the microscopic barrier that is influenced by the dipole, is of a width that is easily tunneled through in their calculations [137]. In our calculation this is a return to the barriers that were calculated using the vacuum level lineup of the Mott-Schottky models.

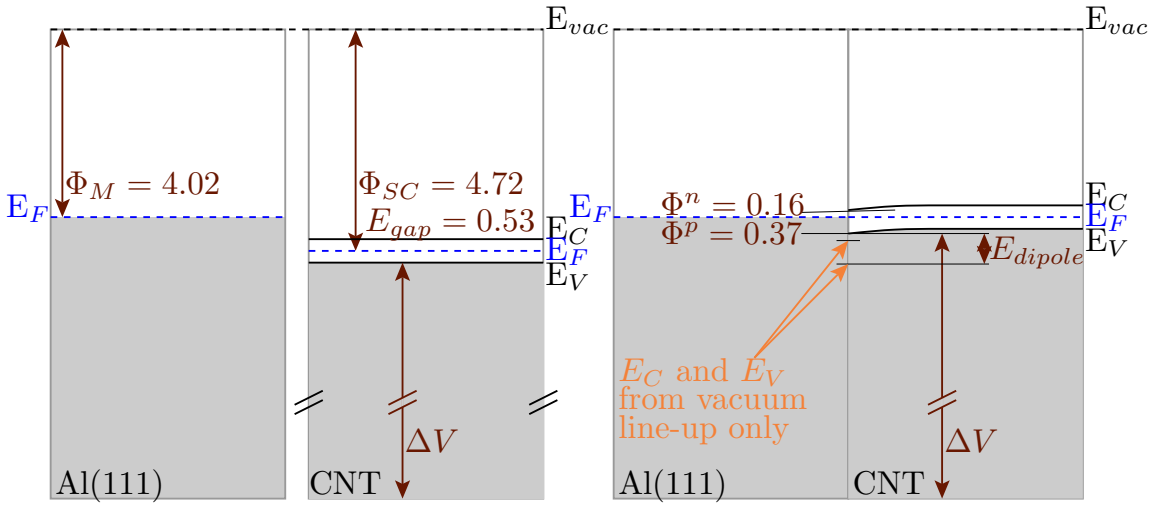

Figure 6.20: Redrawing the band schematic to reflect the effects of the surface dipole for the CNT/Al(111) system.

6.5.5 Summary

Even though the metals have a large difference in work function, the results for the CNT on the clean metal systems show that in both the CNT/Al(111) and the CNT/Pd(111) systems a *p*-type Schottky barrier forms. The results are different than the simple band-bending model presented, but this is to be expected. The bands of the CNT in both cases are driven either upward (for the Al(111) case) or downward (for the Pd(111) case), by the dipole that is formed by charge transfer in the interface region. Following the conclusions of Léonard and Tersoff, we can consider the surface dipole to be highly localized. Thus, the SBH on a more macroscopic scale will tend to the value found from the simple Mott-Schottky model.

Finally, this system is highly idealized, in that (1) it consists of a semi-infinite slab that is always in contact with a CNT that is infinite in 1D and (2) the metallic surface is atomically clean. A real system will consist of a part of the CNT that is not in contact with the metal, also, the system may include chemical impurities or surface roughness. These are the topics of the following sections.

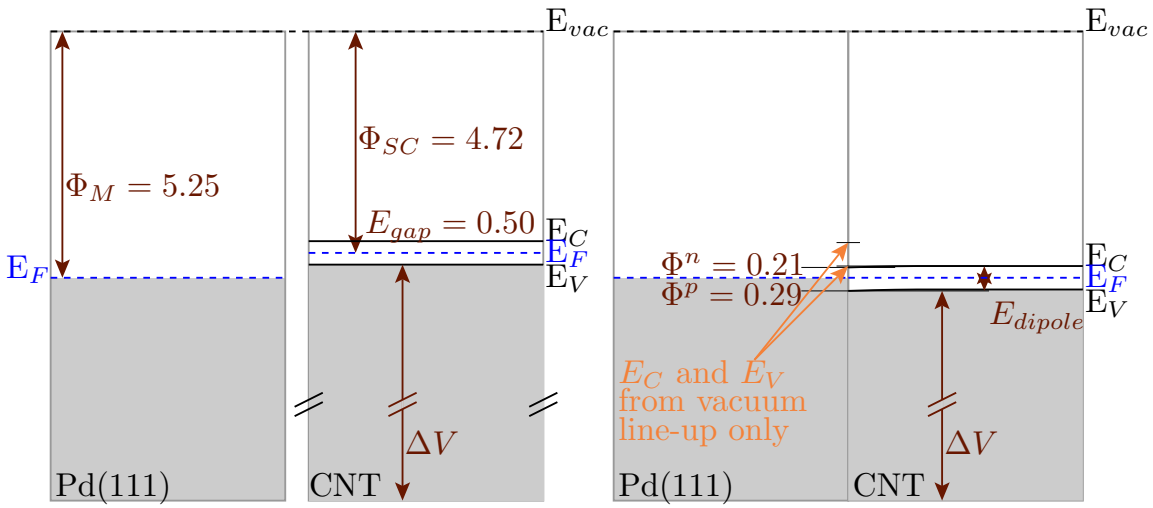

Figure 6.21: Redrawing the band schematic to reflect the effects of the surface dipole for the CNT/Pd(111) system.

6.6 Surface Roughness

It is unlikely that the metallic surface will be pristine in a real system. To this end we investigate the effect that surface roughness has on the CNT/metal systems.

6.6.1 Geometries

Surface roughness is simulated through the addition of metal atoms, half layers, and full layers of metal around the CNT. A half layer is constructed such that the extra metal atoms form a step edge longitudinally along the CNT. While a full layer corresponds to a step on both sides of the CNT (forming a valley that the CNT rests in). In all of the cases considered, full relaxation of the atomic coordinates is performed with the special **k**-point discussed in Appendix D.

For the Al(111) systems the additional layers of Al metal can be seen in the fully relaxed geometries in Figure 6.22. Note that for the case of two and four extra surface layers that the CNT becomes greatly distorted. This distortion of the CNT is only seen in these two systems. It is expected that the sharp edges (noticeable in the figure) create a more reactive surface, and the existence of two reactive edges in these

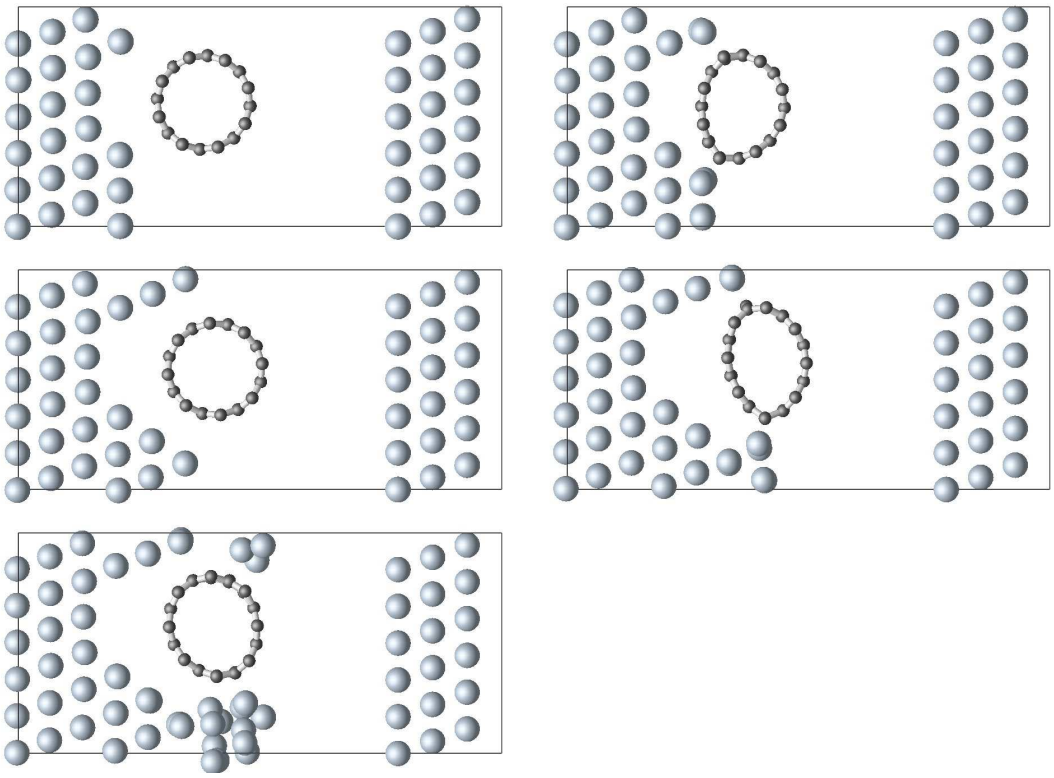

Figure 6.22: The fully relaxed geometries of the surface roughness calculation. left to right: one, two, three, four, and five additional surface layers.

cases causes chemical bonding to the CNT. This is further supported by the binding energy values in Table 6.4 where the binding energies are more than an order of magnitude larger for these two cases.

6.6.2 SBH Results

The addition of single atoms and half layers (single step edges) had only minor effects on the SBH, with a typical change smaller than 0.02 eV. The full relaxation of these systems allows the CNT to move unimpeded to a geometry that is similar to the pristine case – i.e. no chemical bonding and a similar binding distance. Thus, we focus our analysis on the addition of extra layers, as in Figure 6.22. Tables 6.4 and 6.5 show the resulting SBH for the CNT/metal systems with surface roughness.

Table 6.4: The SBH and binding energy for different amounts of surface roughness for the (8,0) CNT on Al(111).

System	Binding E (eV)	Φ_M (eV)	Φ^p_{SBH} (eV)	Φ^n_{SBH} (eV)
Clean Al	-0.17	4.04	0.37	0.16
1 Surface Layer	-0.19	4.04	0.39	0.14
2 Surface Layers	-3.30	4.09	0.38	0.10
3 Surface Layers	-0.05	4.08	0.52	0.00
4 Surface Layers	-4.91	4.10	0.34	0.14
5 Surface Layers	-	-	-	-

Table 6.5: The SBH and binding energy for different amounts of surface roughness for the (8,0) CNT on Pd(111).

System	Binding E (eV)	Φ_M (eV)	Φ^p_{SBH} (eV)	Φ^n_{SBH} (eV)
Clean Pd	-2.96	5.26	0.29	0.21
1 Surface Layer	-2.82	5.09	0.43	0.20
2 Surface Layers	-3.97	5.02	0.42	0.19

The data in table 6.4 presents no apparent trend in the SBH with addition of surface roughness layers for the CNT/Al(111) system. However, if we divide the systems into two different case-types a trend is visible. For the cases where the CNT is not distorted (1 and 3 layers) the SBH increases with additional layers. While for the case where the CNT is heavily distorted (2 and 4 layers) the SBH is decreasing. Further evidence for why this is the case is provided by the density of states, in the following section.

Table 6.5 shows the SBH results for the CNT/Pd(111) system with surface roughness. Most notably in this system, the extra layers of metal surrounding the CNT open the band gap of the CNT further (0.1 eV). This is reflected only in an increase of the p-type SBH – i.e. the location of the system Fermi energy with respect to the conduction band does not change.

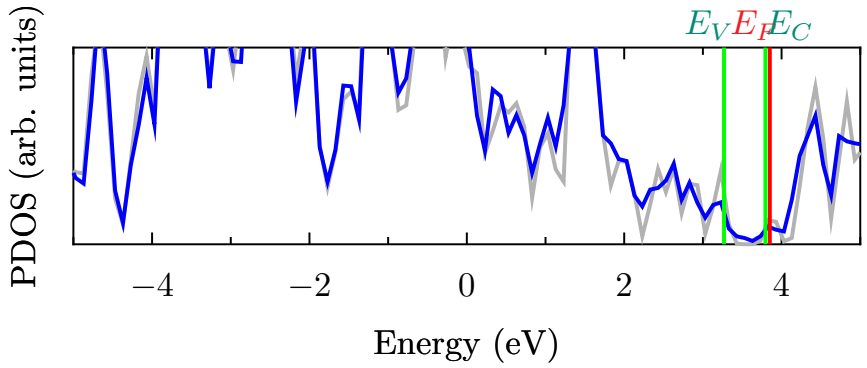

Figure 6.23: PDOS for CNT on Al(111) with 3 layers of surface roughness. Blue: The p-projection on a C-atom far from the CNT/metal interface. Gray: PDOS for the same p-projection on a C-atom of the isolated CNT.

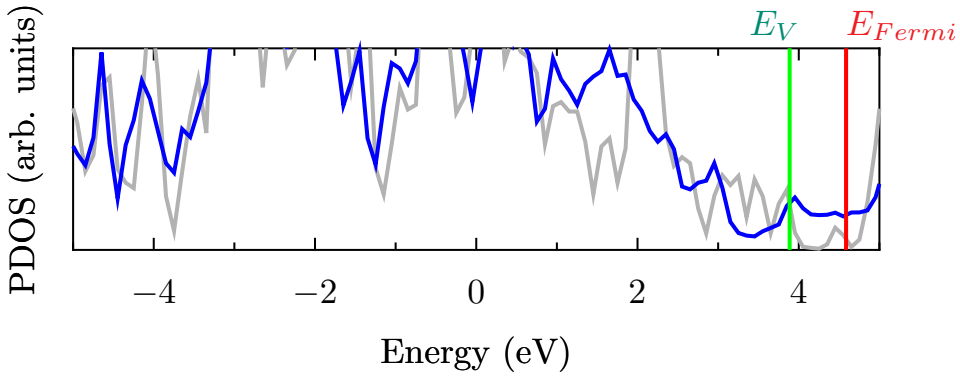

Figure 6.24: PDOS for CNT on Al(111) with 5 layers of surface roughness. Blue: The p-projection on a C-atom far from the CNT/metal interface. Gray: PDOS for the same p-projection on a C-atom of the isolated CNT.

6.6.3 PDOS Analysis

The PDOS for all the cases of surface roughness were analysed. For the cases where the CNT is not distorted the system with three surface roughness layers and the system with five layers can illustrate the reasons for the trend seen, Figures 6.23 and 6.24, respectively. The CNT is effectively in a valley where a portion of the dipoles that are normal to the surface steps will cancel each other out. This leads to less raising of the CNT band energies (and less decrease in the CNT work function). Thus the p-type SBH for these cases is increasing with surface layers. However, once the

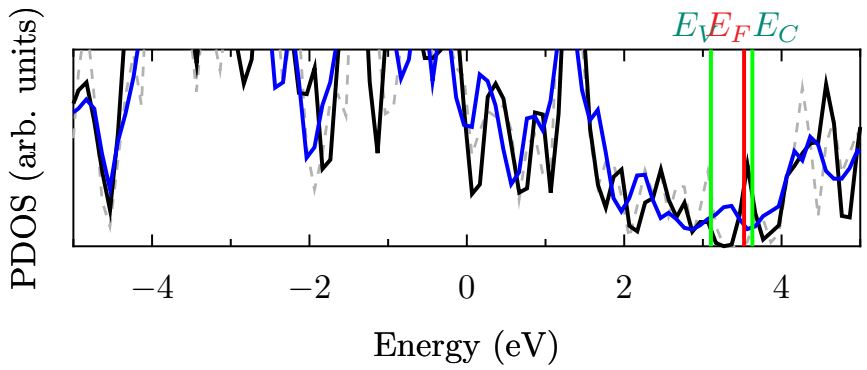

Figure 6.25: PDOS for CNT on Al(111) with 2 layers of surface roughness. Blue: The p-projection on a C-atom far from the CNT/metal interface. Gray: PDOS for the same p-projection on a C-atom of the isolated CNT. Black: PDOS for the projection on the C-atom for the isolated *distorted* CNT.

CNT is covered by metallic layers (system with 5-surface layers), the system Fermi energy rests inside the conduction band of the CNT – i.e. there are no barriers.

For the cases where the CNT is highly distorted a different picture emerges. The distorted CNT has an altered band structure – i.e. the bands are not only shifted, but band gaps are also changed. This altered structure can pin the Fermi energy of the system at an energy that is within the clean CNT energy gap, seen in Figure 6.25. In the figure, the blue line is the PDOS projection for the C-atom in the full system, while the black and gray lines are for the isolated CNT in the distorted and non-distorted geometries, respectively. The valence and conduction energy levels in the figure refer to the band edges for the isolated undistorted CNT.

6.6.4 Summary

Surface roughness has some notable effects on the CNT/metal SBH. In particular if the surface roughness causes chemical bonding or alters the magnitude of the surface dipole, the SBH is shifted. Again, the electrostatic control of the SBH is likely to occur in the vicinity of the surface dipole, but as in the clean surface cases, this surface dipole is localized.

Table 6.6: Schottky barrier heights of functionalized-CNT/metal systems. Reference CNT systems are taken as the isolated functionalized CNT. All values are in eV.

Func. Grp.	Metal	Φ^p_{SBH}	Φ^n_{SBH}
No Func.	Al(111)	0.37	0.16
2H	Al(111)	0.25	0.20
CCl_2	Al(111)	0.33	0.22
No Func.	Pd(111)	0.29	0.21
2H	Pd(111)	0.27	0.20
CCl_2	Pd(111)	0.28	0.22

6.7 Chemical Functionalization of the CNT

As we saw in Chapter 5 chemical functionalization can have an effect on the electronic structure (in particular the work function) of a CNT. We investigate here the effect of chemical functionalizations on the SBH of CNT/metal junctions.

In Chapter 5, we classified two groups of chemical functionalizations to CNTs: electropositive and electronegative. We choose one case from each classification to include in the CNT/metal systems: 2 H atoms for the electropositive case, and dichlorocarbene (–CCl_2) for the electronegative case. In both cases the functional group is placed on the side of the CNT that is opposite the interface. Furthermore, they are both in the *skewed* geometry discussed in Chapter 5.

6.7.1 SBH Results

The SBHs for the chemically functionalized CNTs are determined using the potential profile line-up. However, with the use of periodic boundary conditions, the system we are actually simulating is a 1D infinite CNT with a periodic infinite array of the same functional group. Thus, we consider a reference systems that are the isolated and functionalized CNT.

The SBH results are summarized in Table 6.6. The addition of chemical functionalization alters the band gap of the CNT. We see a small closing for the 2H case and a small opening for the CCl_2 case. Similar to the surface roughness, the changes

in the band gap are reflected only in a change to the p-type SBH. For the Al(111) cases the largest change is seen with the addition of 2 H atoms, this electropositive addition likely increases the surface dipole through the introduction of an implicit dipole across the CNT. For the Pd(111) case, no notable changes occur with the functionalization of the CNT. This is likely because the surface dipole in these cases is due to the bonding at the surface and is less affected by the external electrostatic interactions.

6.8 Chemisorbtion on CNT

One proposed use of CNTs is as gas sensors. To this end we investigate the effects of chemisorption on the SBH in CNT/metal systems. In particular, we are interested in O_2 and NH_3 chemisorption to the side walls of the CNT.

6.8.1 Methodological Changes for O_2

There are two extra computational considerations when dealing with O_2. First the electronic ground state of the O_2 molecule is a triplet state, thus the calculation must take spin-polarization into account – i.e. the spin-up and spin-down components of the charge density must be treated separately. Second, it has been discussed previously by Giannozzi *et al.* that GGAs do not capture this triplet state for the O_2 molecule, while LDA does capture the correct configuration [151]. Thus, for this portion of the study we switch to LDA.

The switch to LDA requires a re-calculation of the Al and Pd lattice parameters. The Al lattice parameter using LDA is found to be $a_0 = 7.476$ a.u. $= 3.96$ Å and the bulk modulus is $K = 81.4$ GPa. The Pd lattice parameter using LDA is found to be $a_0 = 7.329$ a.u. $= 3.88$ Å and the bulk modulus is $K = 223.0$ GPa. These values are close to the values of PBE and experimental values in Table 4.1.

Table 6.7: Schottky barrier heights for CNT/Al(111) with chemisorption of O_2 and NH_3, also shown is the clean CNT/Pd(111) SBH calculated using LDA.

System	Φ^p_{SBH} (eV)	Φ^n_{SBH} (eV)
Clean Al	0.56	0.07
NH_3 on CNT	0.59	0.04
O_2 on CNT	0.47	0.15
O_2 and NH_3 on CNT	0.48	0.15
Clean Pd	0.35	0.21

6.8.2 Geometries

There are numerous possible geometries when considering the addition of a molecular species to the CNT/metal systems. To this end we relax the systems fully from a starting point that is near the CNT. After relaxation the molecules are loosely bound to the outer wall of the CNT.

6.8.3 Results

The full results for the chemisorption study are found in Table 6.7. The addition of O_2 did not alter the size of the band gap. This is different than the cases of chemical functionalization seen in the previous section. With respect to the clean system (no adsorbates, etc.) the presence of the O_2 molecule shifts the band structure upwards in energy, resulting in a smaller p-type SBH. The NH_3 chemisorption has only minor effects on the SBH.

6.8.4 PDOS Analysis

Figure 6.26 shows the PDOS for the CNT/Al(111) system with an oxygen molecule chemisorbed to the CNT side wall. Note, that the potential line-up is performed using a C-atom that is chosen to be both far from the surface and the oxygen molecule. The features of the clean CNT PDOS are still visible in this case, and the decrease in p-type SBH represents a further upward shift of the CNT energy bands.

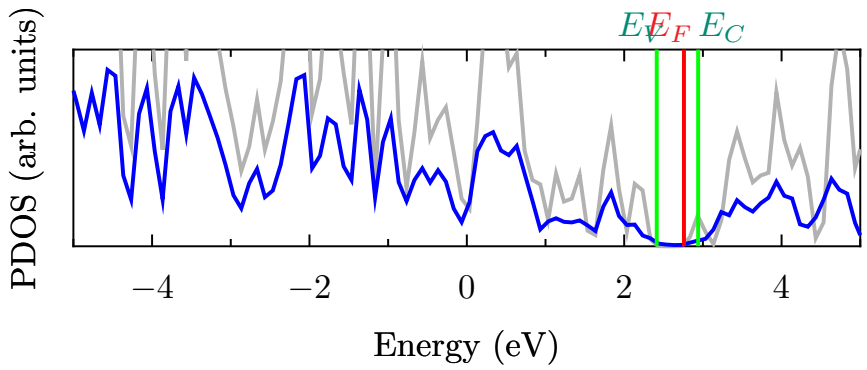

Figure 6.26: Blue: PDOS (2p-projection) for the CNT/Al(111) system with an oxygen molecule adsorbed to the CNT side wall. Gray: PDOS for same C-atom of the clean CNT.

For the case of O_2 we look at the charge density differences. Here we are interested in the difference between the CNT/Al(111)+O_2 system and the CNT/Al(111) system alone:

$$\Delta\rho = \rho_{CNT/Al(111)+molecule} - (\rho_{CNT/Al(111)} + \rho_{O_2}). \tag{6.19}$$

This is different than the $\Delta\rho$ from before, where we were looking at the charge transfer from the metal to the CNT or vice versa. Here, we are interested in charge transfer to or from the O_2 molecule. A significant amount of charge transfer occurs across the CNT/O_2 interface. The O_2 molecule effectively becomes a charge acceptor in the system. Thus, the O_2/CNT system has an implicit dipole with respect to the CNT/metal system. Also, we see that the original surface dipole is not affected. The dipole now present on the CNT raises the CNT band energies and thus increases the n-type SBH.

6.9 Junctions

As mentioned earlier, a more realistic CNT/metal system would include a region in which the CNT is not in contact with the metal. To this end, we investigate systems that we call here "junctions." We use the term junction because the geometries of

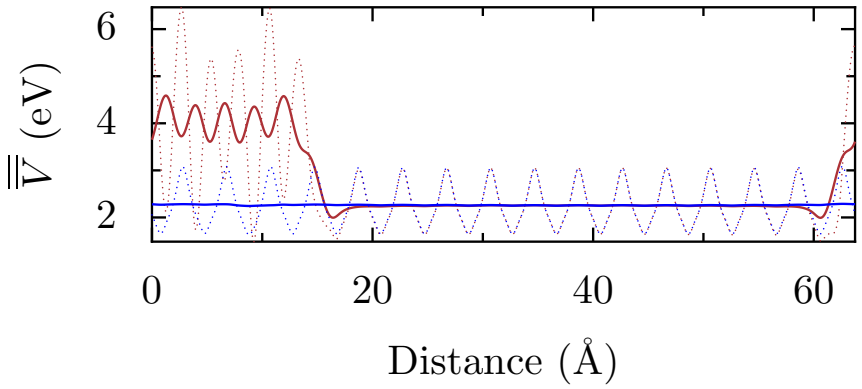

Figure 6.27: Macroscopic average of potential in CNT/metal junction. The electrostatic potential is averaged to the axis parallel to the CNT. Red: The full system. Blue: The isolated CNT of the same length.

these systems more closely matches the typical lead-conductor-lead junction geometry from transport calculations.

The junction geometry consists of the CNT in top contact with the metal (as seen earlier). However, in this system the CNT is extended into a vacuum region. The metal surface that is contacted remains the (111) surface, however, the metal is no longer a 2D semi-infinite slab, in that the direction parallel to the longitudinal axis of the CNT must be truncated to accommodate the new vacuum region. Thus, the metal geometry is more akin to a metal wire that is infinite in 1D perpendicular to the CNT axis.

Furthermore, we look at two lengths of the CNT portion of the junction. One with 64 C-atoms in the vacuum and another with 128 C-atoms in the vacuum, herein called the *short*- and *long*-junctions, respectively. the general geometry for the short junction can be found in Figures 6.28 and 6.29 for the Al and Pd cases, respectively. As in previous sections, the structures here are fully relaxed with a special **k**-point.

6.9.1 Potential Lineup

Interestingly, with this geometry we can perform a potential profile lineup in the original form of Eqn. 6.6. That is, the inclusion of the vacuum region, allows access to

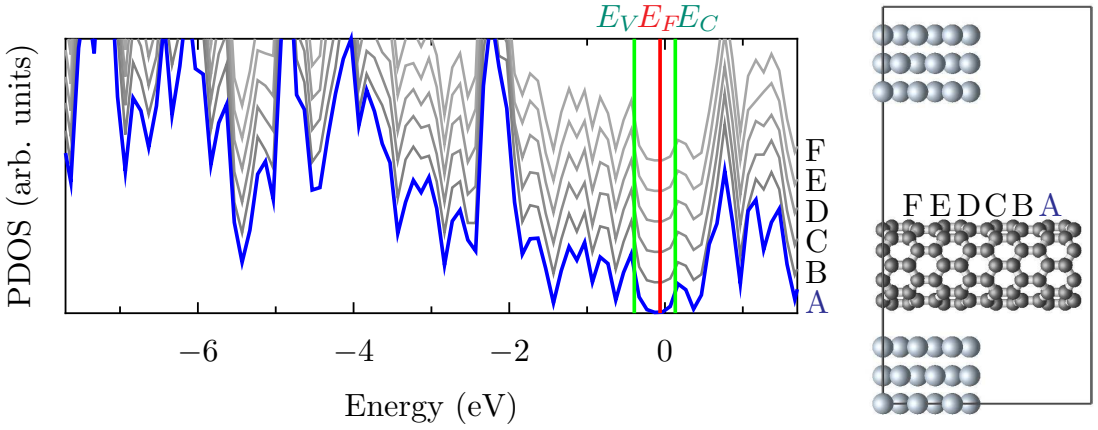

Figure 6.28: PDOS of C-atom p-projected states along the CNT/Al(111) junction

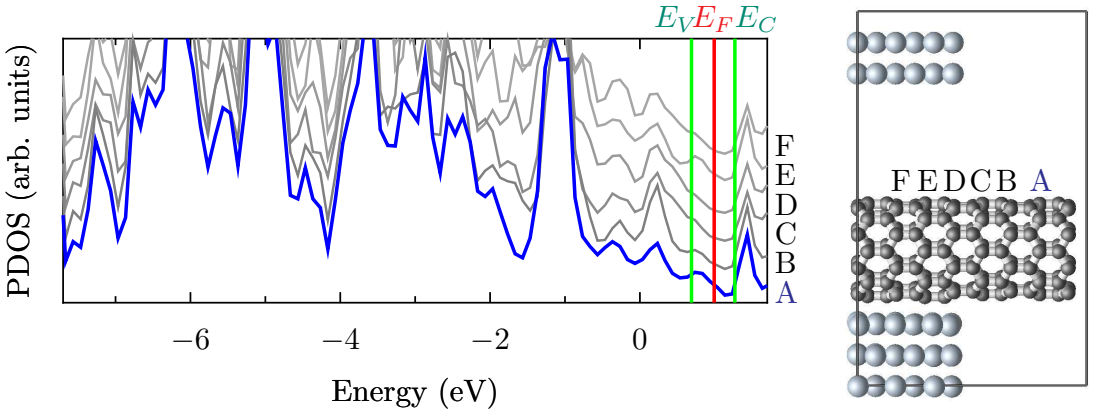

Figure 6.29: PDOS of C-atom p-projected states along the CNT/Pd(111) junction.

the periodic electrostatic potential along the longitudinal axis of the CNT. Figure 6.27 shows the lineup of the macroscopic averages of the long-junction. The macroscopic average of the electrostatic potential for the region of CNT that crosses the vacuum lines up well with that of the isolated CNT. The macroscopic average is taken with a window width that corresponds to one layer of the zig-zag in the CNT that is two atoms thick.

We check to determine that the Fermi level of the full system is still driven by the Fermi energy in the metal. For the short junction this is certainly the case, and

Table 6.8: Schottky barrier heights for CNT/Al(111) and CNT/Pd(111) junctions

System	Metal	Φ^p_{SBH} (eV)	Φ^n_{SBH} (eV)
No Junction	Al(111)	0.37	0.16
Short Junction	Al(111)	0.30	0.23
No Junction	Pd(111)	0.29	0.21
Short Junction	Pd(111)	0.30	0.28

we can continue to use the SBH line-up in the same form as before. However, for the long-junction, the Fermi energy of the full system is different than that of the metal system. Thus we will limit our discussion to that of the short junction.

6.9.2 SBH Results

The results for the CNT/metal junctions are summarized in Table 6.8. We see that for the Al case the addition of the vacuum layer leads to an decrease in the p-type SBH. While for the Pd(111) case these is no change. This difference can be explained by considering the nature of the surface dipole for the two cases. In the CNT/Al case, the dipole is created by a delocalized charge transfer region, see Figure 6.16. When the metal is truncated into a step that the CNT extends away from, a stronger dipole can form at the edge of the metal and further raise the CNT band energies. For the CNT/Pd case, the dipole is more localized in the bonding between the CNT and the metal, see Figure 6.17, and is thus less affected by the truncation of the metal surface and extension of the CNT.

We investigate the PDOS of the short-junction geometries. Following the PDOS for the 2p states for C-atoms along the CNT, Figure 6.28, we see little change in the structure of the PDOS. The band features of the CNT are still clearly visible. Similarly, we investigate the case of the short CNT/Pd(111) junction. Here the PDOS do not change significantly as a function of distance from the interface.

In summary, there are small changes in SBH when the geometry is changed to include a vacuum region. This small change and the unchanged PDOS, show that

the use of our smaller unit cell – e.g. no vacuum region – provides a very close estimate to the case where the metal surface is truncated. Most of the changes can be attributed to the edge effects of the metal and the spreading of the charge along the CNT (especially in the Al(111) case).

6.10 Conclusion

We combined the metal surfaces and CNTs in a study for the Schottky barrier heights (SBH) that form at the interface. The Al(111) and the Pd(111) surfaces are taken as examples of low and high work function metals. We contacted them with the semiconducting (8,0) CNT. In all cases we find that a surface dipole forms that locally shifts the band structure of the CNT. Control of this electrostatic dipole will give increased control of the SBH. However the dipole effects are likely to be local due to the geometry of the CNT metal contact.

Surface roughness can effect the SBH through either modulation of the interfacial dipole or band splitting through distortion of the CNT. Similarly, chemisorption and chemical functionalization can introduce implicit dipoles into the interfacial system and drive the band energies of the CNT either up or down, ultimately altering the SBH. Overall the CNT/Al system were more susceptible to SBH changes due to external electrostatic interactions while the CNT/Pd system are less altered. This is likely due to the more diffuse dipole in the Al case versus the localization of the dipole in the bonding region for the Pd case.

Chapter 7

Conclusions

In this thesis we have employed first-principles calcuations based on density functional theory (DFT) to investigate fundamental properties of molecular scale devices. We focus initially on the constituent components of said devices, followed by studies of larger device geometries.

7.1 Summary

First we have studied the interaction between oligothiophene molecules; a component in a proposed molecular actuating system. The functionality of conjugated polymer systems often relies on oxidation or reductions, in most cases mediated by the presence of counterions. The effect that the common counterion hexafluorophosphate (PF_6^-) has on the intermolecular interactions between charged oligothiophenes was investigated here using ab initio quantum chemistry methods. Counterions were explicitly included in the simulations of oxidized oligothiophenes and in the dimerization process. Our calculations provide quantitative and qualitative insight into the intermolecular interactions in oligothiophene-counterion systems and show that the intermolecular π-stacking of oligothiophenes is not adversely affected by the presence of counterions and that in fact oligothiophene dimerization is further stabilized by

their presence.

Next we have studied the relaxations, surface energies, and work functions of low index metallic surfaces using pseudopotential plane-wave density-functional calculations within the generalized gradient approximation. We have focused on the (100), (110), and (111) surfaces of Al, Pd, Pt, and Au and the (0001) surface of Ti, chosen for their use as contact or lead materials in nanoscale devices. We considered clean, mostly non-reconstructed surfaces in the slab-supercell approximation. Particular attention was paid to the convergence of these quantities with respect to slab thickness; furthermore, different methodologies for the calculation of work functions and surfaces energies are compared. We have found that the use of bulk references for calculations of surface energies and work functions can be detrimental to convergence unless numerical grids are closely matched, especially when surface relaxations are being considered. We have reported data for all surfaces and metals considered and have followed as an example the convergence of these quantities with respect to slab thickness for palladium.

Next we have studied the work function of single wall carbon nanotubes (CNTs) and functionalized carbon nanotubes. We report the work functions calculated within density functional theory using pseudopotentials and plane-wave basis-sets. We have used the metallic (5,5) CNT and semiconducting (8,0) CNT as our pristine systems and functionalize them with a number of different chemical moieties that can be categorized as either monovalent and divalent. We find that functional additions that are electronegative in nature tend to increase the work function of the CNT, while electropositive additions tend to decrease it. These results are rationalized through the investigation of charge redistribution on the carbon nanotube and changes in the electrostatic potential due to the functional additions. Furthermore, we have addressed the spurious dipole interactions that can occur as an artifact of using periodic boundary conditions by employing a self consistent electrostatic correction scheme.

Finally, we have combined the metal surfaces and CNTs in a study for the Schottky barrier heights (SBH) that form at the interface. We have taken the Al(111) and the Pd(111) surfaces as examples of low and high work function metals and contacted them with the semiconducting (8,0) CNT. We find that in all cases a surface dipole forms that locally shifts the band structure of the CNT. We have investigated the effects of surface roughness and functionalization on SBH in these systems, and find that control over the electrostatics at the interface can lead to greater control of the SBH.

Appendix A

Macroscopic Averaging

Macroscopic averaging is a technique through which periodic oscillations can be averaged. For illustration purposes we follow the example of a metal slab with a vacuum region. The slab layers have a uniform spacing, Fig. A.1. For this case we are interested in the macroscopic average of the electrostatic potential, $\overline{\overline{v}}$. The first step is to take a planar average of the potential to an axis that is in a direction of interest (if 3D homogeneity is not present), in this case that is the axis normal to the metal surface, nominally called the z-axis here.

$$\overline{v}(z) = \frac{1}{S}\int_S v(x,y,z)dxdy, \tag{A.1}$$

represented by the dotted line in the figure.

The macroscopic average is then taken by the convolution of the resulting function with a filter function.

$$\overline{\overline{v}}(\tau) = \int w(\tau - \tau')\overline{v}(\tau)d\tau \tag{A.2}$$

The filter can be chosen as a one-dimensional step function:

$$w(z) = \frac{1}{\alpha}\Theta\left(\frac{1}{\alpha} - |z|\right). \tag{A.3}$$

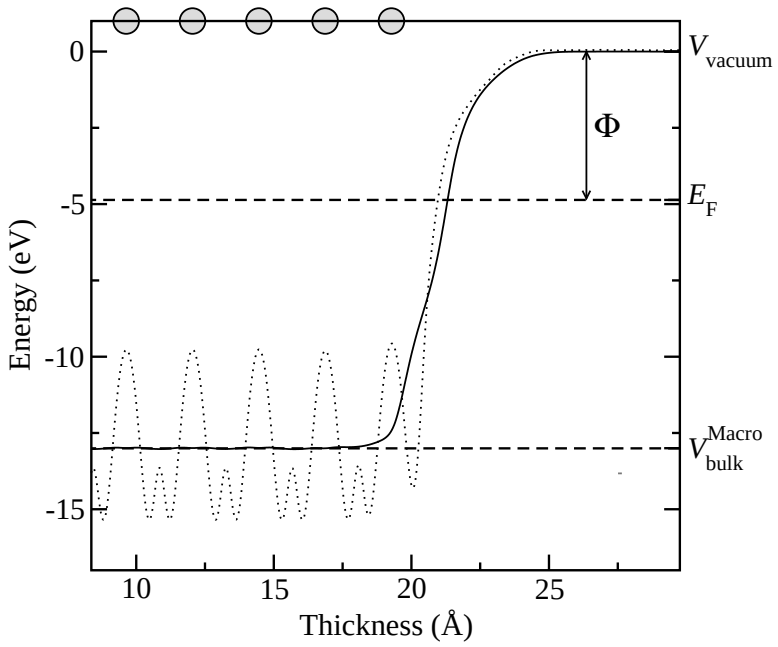

Figure A.1: The methodology of calculating work function from macroscopic averages of the potential. The total electrostatic potential of the slab (dotted line) is averaged and referenced to the macroscopic average of a bulk system (dashed line). The work function, Φ, can be taken as the difference of the vacuum level potential in the slab system and the Fermi level of the bulk system. The gray circles represent the atomic layers of the slab. This example is a 9 layer (5 shown) Au(111) unrelaxed slab.

We are left with the macroscopic average as:

$$\overline{\overline{v}}(z) = \frac{1}{\alpha}\int_{z-\alpha/2}^{z+\alpha/2} \overline{v}(z')dz'. \tag{A.4}$$

If we choose the window, α, to match that of the layer spacing in our slab, the macroscopic average will be a flat function in the interior of the slab, solid line in the figure.

Appendix B

Magnetic Bulk Palladium

Recent calculations in the literature have shown that when evaluated within the generalized gradient approximation (GGA) Pd yields an erroneous magnetic bulk ground state [60, 61]. In light of these observations we have performed a similar evaluation of the ground state of Pd using PBE-GGA and the pseudopotential discussed in Chapter 4. Similar to the results of Alexandre *et al.* we find a magnetic ground state for bulk Pd. We plot both the total energy and the total magnetization as a function of FCC lattice parameter for Pd evaluated with GGA in Fig B.1 and for comparison the same plot is generated for Pd within LDA in Fig B.2.

Finally, we have calculated the surface properties of the Pd(100) with spin-polarization. In all cases the slab maintains a total magnetization, however, this has little effect on the converged surface properties discussed in Chapter 4. The changes in the relaxations and surfaces energies are negligible, while the change in the work functions is seen as an increase of 0.03 eV.

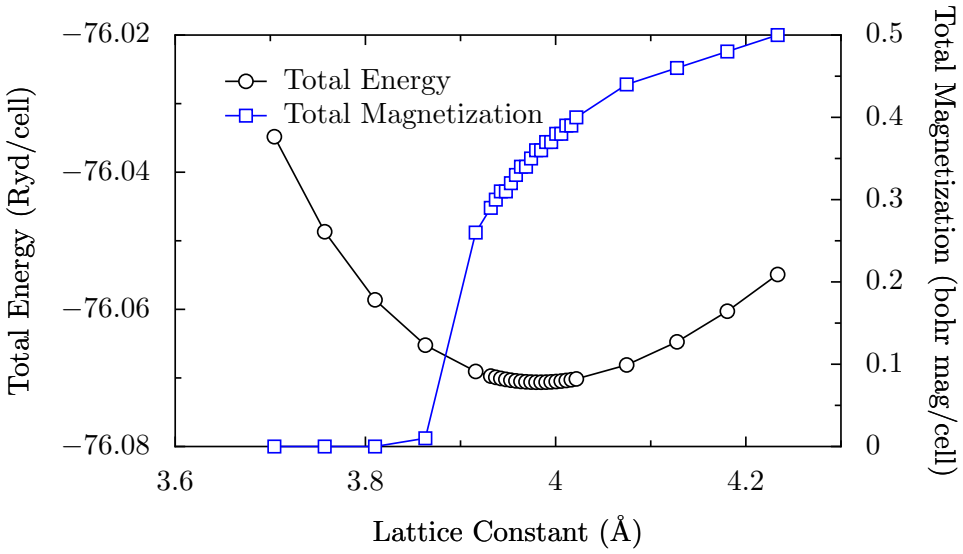

Figure B.1: Total energy per unit cell and total magnetization per unit cell plotted versus the FCC lattice constants of bulk Pd using the GGA-PBE exchange-correlation functional with spin-polarization.

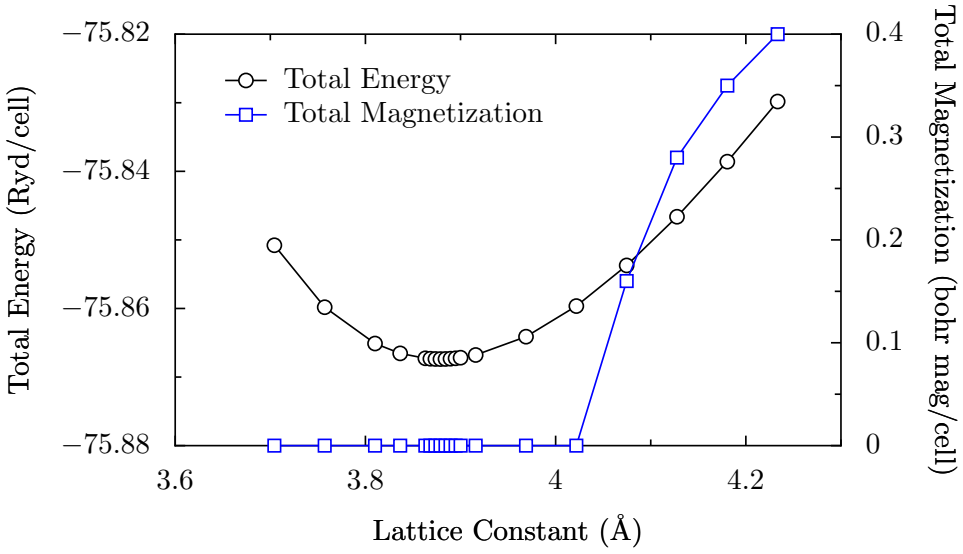

Figure B.2: Total energy per unit cell and total magnetization per unit cell plotted versus the FCC lattice constants of bulk Pd using the LDA exchange-correlation functional with spin-polarization.

Appendix C

Electrostatic Corrections

This appendix presents some further information about the electrostatic corrections seen in Chapter 5 and Ref. [123]. The two sections here are, first, a presentation of the computational work-flow and timing data for the correction. Second a discussion of special cases of 1D periodicity where a 2D generalization of the potential may fail, such is the case for PVDF.

C.1 Work Flow and Timing

As was discussed in Chapter 2, the total energy minimization is done through iteration until self consistency of the charge density. The flow for this type of calculation starts with choice of a trial density, calculation of the respective potentials generated by said density, diagonalization of the resulting Hamiltonian, and calculation of the resulting density. The correction can be added into this loop during the calculation of the potentials, and thus made to also be self-consistent, Fig. C.1. However, there is some benefit to waiting until a few steps of the minimization have been carried out, e.g. that the initial trial density does not generate any mulitpoles that shouldn't exist and are subsequently erroneously corrected for. After turning on the correction it is sufficient to correct every few steps until self consistency, however, in the case of the

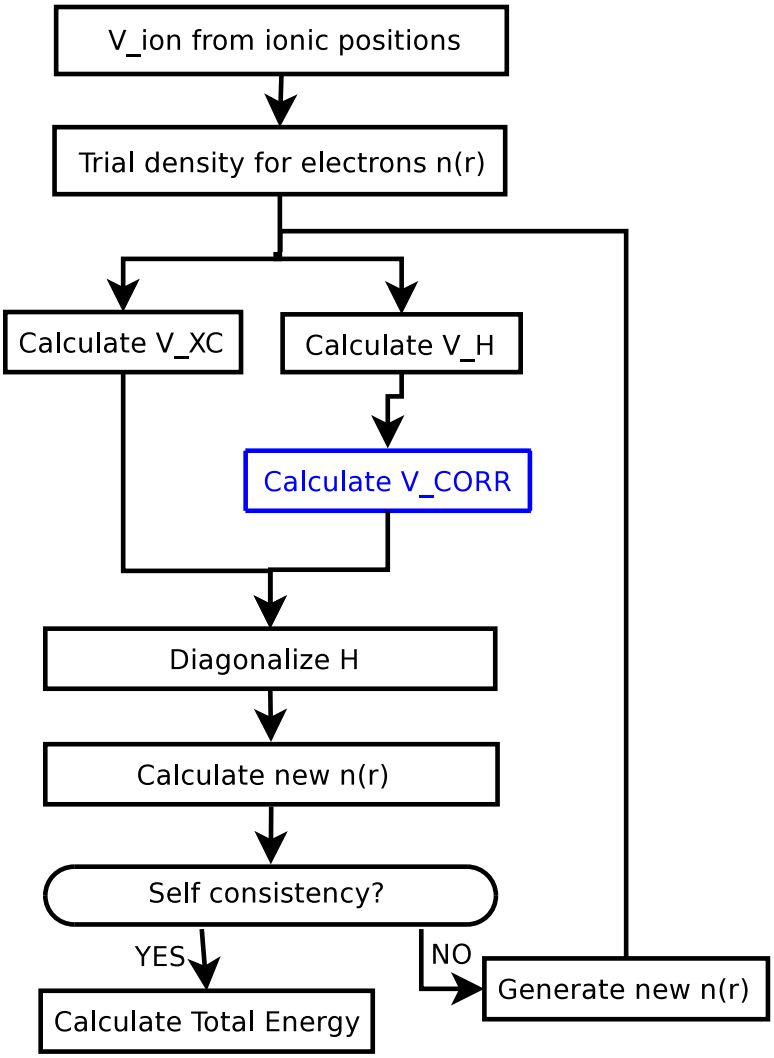

Figure C.1: A schematic of the steps to self-consistency for a DFT calculation including the addition of a corrective potential to the electrostatic potential computed in periodic boundary conditions

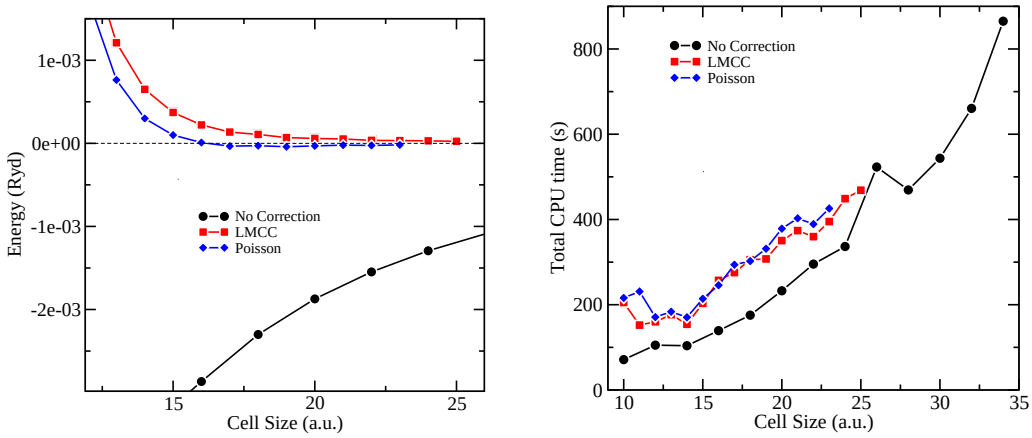

Figure C.2: Energy convergence versus cell-size for the LMCC, exact potential (Poisson), and not corrected calculation (left). Time comparison for all of the calculations (right).

2D generalization, the computational cost in negligible and correction can occur ever step.

Figure C.2 shows the energy convergence versus cell-size for the test system is polyvinylidene fluoride (PVDF), it has a large dipole across the cell and is periodic in one direction (taken here a the z-axis). In Figure C.2 it is clear that the non-corrected calculation will not converge to the correct energy for any tractable cell-size. However, both the Gaussian counter charge (referred to here as LMCC) and the density counter charge (DCC, referred to here as Poisson) converge quickly (by 22 a.u. and 17 a.u., respectively). The figure also shows a time comparison for all of the methods. The LMCC and Poisson methods are comparable in cost for this system because it is only a 1D-periodic system, thus it was possible to average the potentials to a single plane (decreasing the cost of calculating the correction from $O(N^5)$ to $O(N^3)$, where N is grid resolution in one direction).

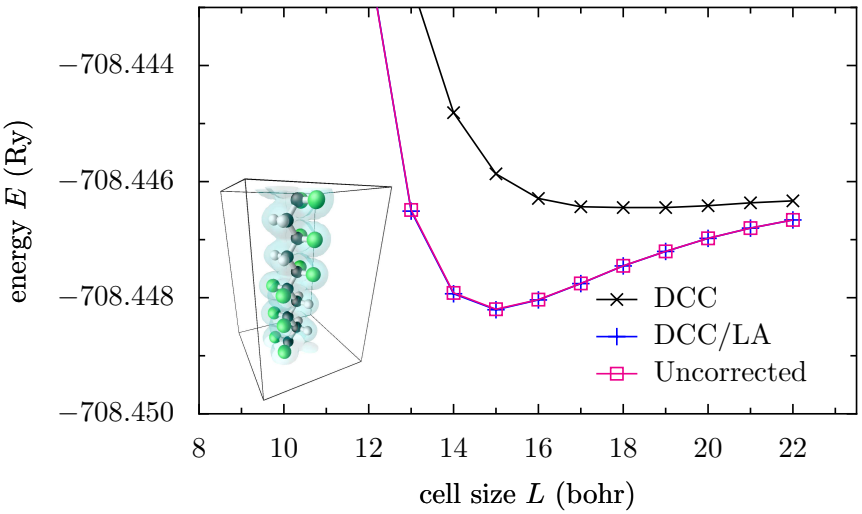

Figure C.3: Total energy versus cell size for the PVDF (inset) that has an oscillating dipole along the direction of the chain. The DCC correction is applied using both a planar average of the entire system (DCC/LA) and a DCC that incorporated the charge fluctuation through the use of a Bessel function expansion (DCC). The uncorrected case is shown for reference.

C.2 1D Generalization

A case where calculating only a 2D correction for the 1D period case could fail to capture the correct electrostatics for the correction. Such is the case for a PVDF molecule that has an oscillating dipole along the chain, see the inst of Fig. C.3. The figure shows the total energy versus cell size for the PVDF along the direction of the chain. The DCC correction is applied using both a planar average of the entire system (DCC/LA) and a DCC that incorporated the charge fluctuation through the use of a Bessel function expansion (DCC). The uncorrected case is shown for reference.

Appendix D

Special K-Points

The unit-cells that we are concerned with in this study typically contain around 200 atoms as well as include some vacuum region. Thus, they are computationally expensive within DFT. Figure 6.12 shows a typical unit cell with a 64 atom CNT and 6 layers of Al (108 atoms). A vacuum region is included to isolate the slab with the CNT on the surface.

These are complicated structures, and it is in our interest to optimize the geometry. However, the 2D periodicity of the slab leads to a necessity for a larger than gamma-point k-point sampling. Typically the forces and energies in these structures were found to converge with respect to k-point sampling with a Monkhorst-Pack k-point mesh of 6x3x1.

It can be shown that a single special k-point can be found that exploits the symmetry of the k-space and in effect very closely approximates the electronic structure [152, 153]. For simple cubic structures and the diamond cubic structure this k-point occurs at the point $(\frac{1}{4}, \frac{1}{4}, \frac{1}{4})$ in the Brillouin zone. This k-point, in general, gives better results for periodic systems than the $\mathbf{\Gamma}$-point, and in some cases it is very close to the well converged results.

Appendix E

Projected Density of States: Line-up

We use a similar method that utilizes the PDOS of the C-atoms of the CNT to lineup the band energies of the CNT/metal system with those of the isolated CNT. This method proceeds in a similar manner to that of the potential profile lineup, noting that the same energy shift is still present for the same reasons as discussed previously. However, we find that this methodology is too sensitive to band splittings that can occur when the CNT form chemical bonds to the metal surface, and thus we do not use this method for the results in the body of the thesis.

In this projection scheme, having used a 4-electron pseudopotential for carbon, a C-atom has a projection for the 2s state and the 2p states. While it is the band energies resulting from the p-electrons that we are ultimately interested in, in principle the s-projections should change less between the CNT/metal and isolated CNT systems. Thus we use the s-projections to determine the value for the energy shift.

The shift is the energy offset of one PDOS versus the other. The top panel of Fig. E.1 show the respective PDOS calculated for the (8,0) CNT on the Al(111) surface, the atom used for the projections is on the CNT, opposite the contact with the metal. The solid lines are the s-projections for the CNT/metal system (blue) and

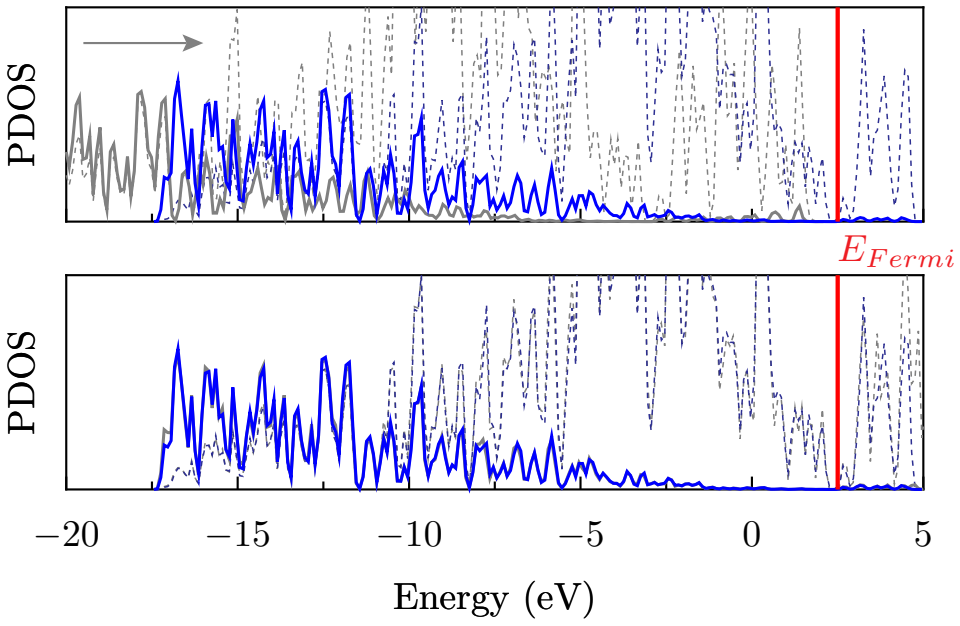

Figure E.1: Calculation of the PDOS energy shift for CNT on Al(111), the atom used for the projections is on the CNT, opposite the contact with the metal. Top panel: The unshifted PDOS, solid lines are s-projections and dashed are the p-projections. Blue represents the full CNT/metal system and gray the isolated CNT. The lineup has been calculated using the s-projections.

the isolated system (gray). The p-projections are shown for reference as the dashed lines. The line-up can be achieved through a method of lowest root mean squared differences (RMS), taking:

$$\Delta\text{PDOS}(E)_{RMS} = \left(\sum_{N} \left(\text{PDOS}_{Sys}(E_0) - \text{PDOS}_{CNT}(E - E_0)\right)^2\right)^{1/2}, \qquad \text{(E.1)}$$

where $\Delta E = E - E_0$ is the shift in energy. The result of applying this method and shift can be seen in the lower panel of Fig E.1. From the figure, it is clear that the line-up for this case is quite good, and even the p-projections are well matched. Fig. E.2 shows the same type of line-up for the CNT on Pd(111) system. Here the p-projections do not match nearly as well as the previous case, but the s-projections provide a good lineup. The lowest energy peaks correspond well and applying the RMS and shift to the p-projections yields a good lineup of the CNT band features.

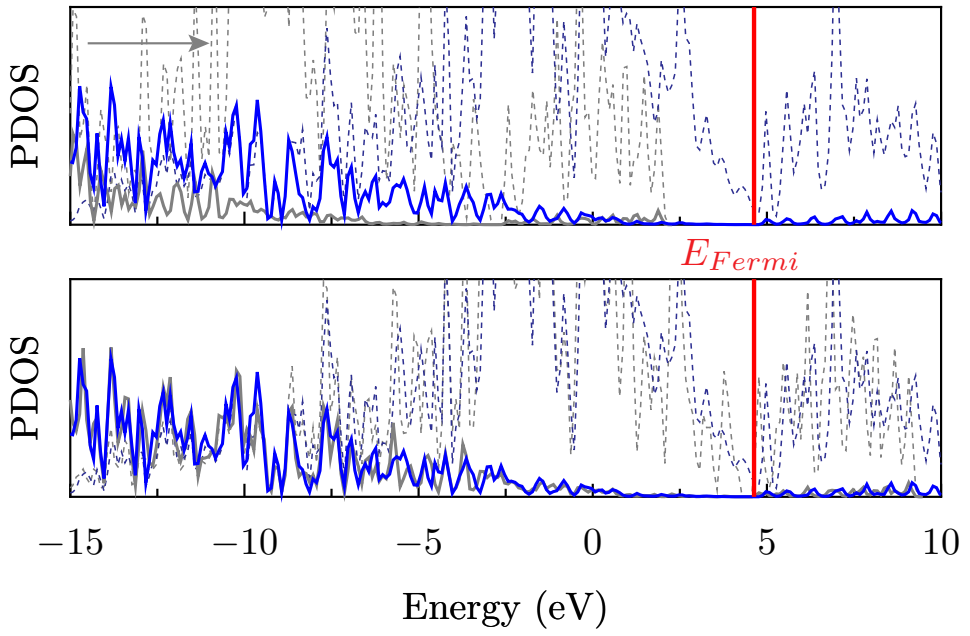

Figure E.2: Calculation of the PDOS energy shift for CNT on Pd(111), the atom used for the projections is on the CNT, opposite the contact with the metal. Top panel: The unshifted PDOS, solid lines are s-projections and dashed are the p-projections. Blue represents the full CNT/metal system and gray the isolated CNT. The lineup has been calculated using the s-projections.

Bibliography

[1] R. Feynman. There's plenty of room at the bottom: an invitation to open up a new field of physics. *Engineering and Science (California Institute of Technology)*, 23(5):22–36, 1960.

[2] B. Yu and M. Meyyappan. Nanotechnology: Role in emerging nanoelectronics. *Solid-State Electronics*, 50:536–544, 2006.

[3] Latha Venkataraman, Jennifer E. Klare, Colin Nuckolls, Mark S. Hybertsen, and Michael L. Steigerwald. Dependence of single-molecule junction conductance on molecular conformation. *Nature*, 442(7105):904–907, 2006.

[4] P. Avouris, J. Appenzeller, R. Martel, and S.J. Wind. Carbon nanotube electronics. *Proceedings of the IEEE*, 91(11):1772–1784, 2003.

[5] R. Martel, T. Schmidt, H. R. Shea, T. Hertel, and Ph. Avouris. Single- and multi-wall carbon nanotube field-effect transistors. *Applied Physics Letters*, 73(17):2447–2449, 1998.

[6] Robert G. Parr and Weitao Yang. *Density-functional Theory of Atoms and Molecules*. Oxford University Press US, 1989.

[7] Attila Szabo and Neil S. Ostlund. *Modern Quantum Chemistry: Introduction to Advanced Electronic Structure Theory*. Dover Publications, 1996.

[8] Richard M. Martin. *Electronic Structure: Basic Theory and Practical Methods*. Cambridge University Press, 2004.

[9] P. Hohenberg and W. Kohn. Inhomogeneous Electron Gas. *Phys. Rev. B*, 136(3):864–871, 1964.

[10] W. Kohn and L.J. Sham. Self-Consistent Equations Including Exchange and Correlation Effects. *Physical Review A*, 140(4):1133–1138, 1965.

[11] J.P. Perdew, K. Burke, and M. Ernzerhof. Generalized Gradient Approximation Made Simple. *Phys. Rev. Lett.*, 77(18):3865–3868, 1996.

[12] S. Baroni, A. Dal Corso, S. de Gironcoli, P. Giannozzi, C. Cavazzoni, G. Ballabio, S. Scandolo, G. Chiarotti, P. Focher, A. Pasquarello, K. Laasonen, A. Trave, R. Car, N. Marzari, and A. Kokalj. Quantum-ESPRESSO. http://www.pwscf.org.

[13] M. C. Payne, M. P. Teter, D. C. Allan, T. A. Arias, and J. D. Joannopoulos. Iterative minimization techniques for ab initio total-energy calculations: molecular dynamics and conjugate gradients. *Rev. Mod. Phys.*, 64(4):1045–1097, Oct 1992.

[14] A.J. Heeger, S. Kivelson, and J.R. Schrieffer. Solitons in conductiong polyers. *Rev. Mod. Phys.*, 60:781–850, 1988.

[15] M. Gross, D.C. Müller, H. Nothofer, U. Scherf, D. Neher, C. Bräuchle, and K. Meerholz. Improving the performance of doped π-conjugated polymers for use in organic light-emitting diodes. *Nature (London)*, 405:661–665, 2000.

[16] A. Moliton and R.C. Hiorns. Review of lectronic and optical properties of semiconducting π-conjugated polymers: applications in optoelectronics. *Polym. Int.*, 53:1397–1412, 2004.

[17] T. Pappenfus, R. Chesterfield, C. Frisbie, K. Mann, J. Casado, J. Raff, and L. Miller. A π-stacking Terthiophene-Based Quinodimethane Is an n-Channel Conductor in a Thin Film Transistor. *J. Am. Chem. Soc.*, 124:4184–4185, 2002.

[18] J-L Bredas, D. Beljonne, V. Coropceanu, and J. Cornil. Charge-Transfer and Energy-Transfer Processes in π-Conjugated Oligomers and Polymers: A Molecular Picture. *Chem. Rev.*, 104:4971–5003, 2004.

[19] Y. Yu, E. Gunic, B. Zinger, and L.L. Miller. Spectra and Reactivity of Methoxyoligothiophene Cation Radicals. *Journal of the American Chemical Society*, 118:1013–1018, 1996.

[20] D.A. Scherlis and N. Marzari. π-Stacking in Thiophene Oligomers as the Driving Force for Electroactive Materials and Devices. *Journal of the American Chemical Society*, 127:3207–3212, 2005.

[21] T. Satou, T. Sakai, T. Kaikawa, K. Takimiya, T. Otsubo, and Y Aso. alpha,omega-bis(quinquethienyl)alkanes as a pi-dimer model of polythiophene. *ORGANIC LETTERS*, 6:997–1000, 2004.

[22] M. R. Gandhi, P. Murray, G. M. Spinks, and G. G. Wallace. Mechanism of electromechanical actuation in polypyrrole. *Synthetic Metals*, 73:247–256, 1995.

[23] Wen Lu, Andrei G. Fadeev, Baohua Qi, Elisabeth Smela, Benjamin R. Mattes, Jie Ding, Geoffrey M. Spinks, Jakub Mazurkiewicz, Dezhi Zhou, Gordon G. Wallace, Douglas R. MacFarlane, Stewart A. Forsyth, and Maria Forsyth. Use of Ionic Liquids for pi -Conjugated Polymer Electrochemical Devices. *Science*, 297(5583):983–987, 2002.

[24] John D. Madden, Ryan A. Cush, Tanya S. Kanigan, and Ian W. Hunter. Fast contracting polypyrrole actuators. *Synthetic Metals*, 113:185–192, 2000.

[25] Nicholas E. Singh-Miller, Damian A. Schelis, and Nicola Marzari. Effect of Counterions on the Interactions of Charged Oligothiophenes. *Journal of Physical Chemistry B*, 110:24822–24826, 2006.

[26] L.L. Miller and K.R. Mann. π-Stacks in Solution and in Conducting Polymers. *Acc. Chem. Res.*, 29(9):417–423, 1996.

[27] Geert Brocks. pi-dimers of oligothiophene cations. *J. Chem. Phys.*, 112(12):5353–5363, 2000.

[28] Geert Brocks. Charged oligothiophene dimers and π-stacks: the bipolaron revisited. *Synthetic Metals*, 119:253–254, 2001.

[29] D.A. Scherlis and N. Marzari. π-Stacking in Charged Thiophene Oligomers. *Journal of Physical Chemistry B*, 108:17791–17795, 2004.

[30] Yoshio Nogami, Jean-Paul Pouget, and Takehiko Ishiguro. Structure of highly conducting PF6–doped polypyrrole. *Synthetic Metals*, 62:257–263, 1994.

[31] Kwang Sun Ryu, Jae Hoon Jung, Jinsoo Joo, and Soon Ho Chang. Improved Conducting States Induced by an Electrochemical Charging Process in Polyaniline Film Doped with New Dopants. *Journal of The Electrochemical Society*, 149(4):A478–A482, 2002.

[32] Bernward A. Mann, Christian Holm, and Kurt Kremer. Swelling of polyelectrolyte networks. *J. Chem. Phys.*, 122(15):154903, 2005.

[33] O. Pizio, K. Bucior, A. Patrykiejew, and S. Sokolowski. Density-functional theory for fluid mixtures of charged chain particles and spherical counterions in contact with charged hard wall: Adsorption, double layer capacitance, and the point of zero charge. *J. Chem. Phys.*, 123, 2005.

[34] M. J. Frisch, G. W. Trucks, H. B. Schlegel, G. E. Scuseria, M. A. Robb, J. R. Cheeseman, J. A. Montgomery, Jr., T. Vreven, K. N. Kudin, J. C. Burant, J. M. Millam, S. S. Iyengar, J. Tomasi, V. Barone, B. Mennucci, M. Cossi, G. Scalmani, N. Rega, G. A. Petersson, H. Nakatsuji, M. Hada, M. Ehara, K. Toyota, R. Fukuda, J. Hasegawa, M. Ishida, T. Nakajima, Y. Honda, O. Kitao,

H. Nakai, M. Klene, X. Li, J. E. Knox, H. P. Hratchian, J. B. Cross, V. Bakken, C. Adamo, J. Jaramillo, R. Gomperts, R. E. Stratmann, O. Yazyev, A. J. Austin, R. Cammi, C. Pomelli, J. W. Ochterski, P. Y. Ayala, K. Morokuma, G. A. Voth, P. Salvador, J. J. Dannenberg, V. G. Zakrzewski, S. Dapprich, A. D. Daniels, M. C. Strain, O. Farkas, D. K. Malick, A. D. Rabuck, K. Raghavachari, J. B. Foresman, J. V. Ortiz, Q. Cui, A. G. Baboul, S. Clifford, J. Cioslowski, B. B. Stefanov, G. Liu, A. Liashenko, P. Piskorz, I. Komaromi, R. L. Martin, D. J. Fox, T. Keith, M. A. Al-Laham, C. Y. Peng, A. Nanayakkara, M. Challacombe, P. M. W. Gill, B. Johnson, W. Chen, M. W. Wong, C. Gonzalez, and J. A. Pople. Gaussian 03, Revision C.02. Gaussian, Inc., Wallingford, CT, 2004.

[35] F. Jensen. *Introduction to Computational Chemistry*. John Wiley & Sons, New York, 1999.

[36] S. Tepavcevic, A. T. Wroble, M. Bissen, D. J. Wallace, Y. Choi, and L. Hanley. Photoemission Studies of Polythiophene and Polyphenyl Films Produced via Surface Polymerization by Ion-Assisted Deposition. *J. Phys. Chem. B*, 109:7134, 2005.

[37] U. Salzner, P Pickup, R Poirier, and J Lagowski. Accurate Method for Obtaining Band Gaps in Conducting Polymers Using a DFT/Hybrid Approach. *Journal of Physical Chemistry A*, 102(15):2572–2578, 1998.

[38] Alessio Filippetti. Electron affinity in density-functional theory in the local-spin-density approximation. *Phys. Rev. A*, 57(2):914–919, Feb 1998.

[39] C. Toher, A. Filippetti, S. Sanvito, and Kieron Burke. Self-Interaction Errors in Density-Functional Calculations of Electronic Transport. *Phys. Rev. Lett.*, 95(14):146402, 2005.

[40] J. Hafner, C. Wolverton, and G. Ceder. Toward computational materials design: the impact of density functional theory on materials research. *MRS Bulletin*, 31:659–668, 2006.

[41] N. Marzari. Toward computational materials design: the impact of density functional theory on materials research. *MRS Bulletin*, 31:681–687, 2006.

[42] S. Heinze, J. Tersoff, R. Martel, V. Derycke, J. Appenzeller, and Ph. Avouris. Carbon Nanotubes as Schottky Barrier Transistors. *Phys. Rev. Lett.*, 89(10):106801, Aug 2002.

[43] M W Finnis and V Heine. Theory of lattice contraction at aluminium surfaces. *J. Phys. F: Met. Phys.*, 4(3):L37–L41, 1974.

[44] W. R. Tyson and W. A. Miller. Surface free energies of solid metals: Estimation from liquid surface tension measurements. *Surf. Sci.*, 62:267–276, 1977.

[45] J. C. Boettger. Nonconvergence of surface energies obtained from thin-film calculations. *Phys. Rev. B*, 49(23):16798–16800, Jun 1994.

[46] M. Methfessel, D. Hennig, and M. Scheffler. Trends of the surface relaxations, surface energies, and work functions of the 4d transition metals. *Phys. Rev. B*, 46(8):4816–4829, Aug 1992.

[47] Juarez L.F. Da Silva, Catherine Stampfl, and Matthias Scheffler. Converged properties of clean metal surfaces by all-electron first-principles calculations. *Surf. Sci.*, 60:703–715, 2006.

[48] N. D. Lang and W. Kohn. Theory of Metal Surfaces: Work Function. *Phys. Rev. B*, 3(4):1215–1223, Feb 1971.

[49] Peter J. Feibelman and D. R. Hamann. Quantum-size effects in work functions of free-standing and adsorbed thin metal films. *Phys. Rev. B*, 29(12):6463–6467, Jun 1984.

[50] S. Ciraci and Inder P. Batra. Theory of the quantum size effect in simple metals. *Phys. Rev. B*, 33(6):4294–4297, Mar 1986.

[51] C. M. Wei and M. Y. Chou. Theory of quantum size effects in thin Pb(111) films. *Phys. Rev. B*, 66:233408, 2002.

[52] C.J. Fall, N. Binggeli, and A. Baldereschi. Deriving accurate work functions from thin-slab calculations. *J. Phys.: Condens. Matter*, 11(13):2689–2696, 1999.

[53] L. Vitos, A. Ruban, and H.L. Skriver. The surface energy of metals. *Surf. Sci.*, 411:186, 1998.

[54] G. A. Benesh and Daniel Gebreselasie. Relaxation of Al(001) and Al(110): Surface embedded Green function total-energy and force calculation. *Phys. Rev. B*, 54(8):5940–5945, Aug 1996.

[55] Hendrik J. Monkhorst and James D. Pack. Special points for Brillouin-zone integrations. *Phys. Rev. B*, 13(12):5188–5192, Jun 1976.

[56] Nicola Marzari, David Vanderbilt, Alessandro De Vita, and M. C. Payne. Thermal Contraction and Disordering of the Al(110) Surface. *Phys. Rev. Lett.*, 82(16):3296–3299, Apr 1999.

[57] Andrew M. Rappe, Karin M. Rabe, Efthimios Kaxiras, and J. D. Joannopoulos. Optimized pseudopotentials. *Phys. Rev. B*, 41(2):1227–1230, Jan 1990.

[58] David Vanderbilt. Soft self-consistent pseudopotentials in a generalized eigenvalue formalism. *Phys. Rev. B*, 41(11):7892–7895, Apr 1990.

[59] F.D. Murnaghan. The compressibility of media under extreme pressures. *Proc. Nat. Acad. Sci.*, 30:244–247, 1944.

[60] Simone S. Alexandre, Maurizio Mattesini, José M. Soler, and Félix Yndurain. Comment on "Magnetism in Atomic-Size Palladium Contacts and Nanowires". *Phys. Rev. Lett.*, 96(7):079701, 2006.

[61] D. A. Stewart. Magnetism in coaxial palladium nanowires. *J. Appl. Phys.*, 101(9):09D503, 2007.

[62] Charles Kittel. *Introduction to Solid State Physics (seventh ed.)*. John Wiley & Sons, 1996.

[63] J. A. Rayne. Elastic Constants of Palladium from 4.2-300°K. *Phys. Rev.*, 118(6):1545–1549, Jun 1960.

[64] R. E. MacFarlane, J. A. Rayne, and C. K. Jones. Anomalous temperature dependence of shear modulus c_{44} for platinum. *Phys. Lett.*, 18:91–92, 1965.

[65] J. R. Neighbours and G. A. Alers. Elastic Constants of Silver and Gold. *Phys. Rev.*, 111(3):707–712, Aug 1958.

[66] E. S. Fisher and C. J. Renken. Single-Crystal Elastic Moduli and the hcp → bcc Transformation in Ti, Zr, and Hf. *Phys. Rev.*, 135(2A):A482–A494, Jul 1964.

[67] J. Perdereau, J. P. Biberian, and G. E. Rhead. Adsorption and surface alloying of lead monolayers on (111) and (110) faces of gold. *J. Phys. F: Met. Phys.*, 4(5):798–806, 1974.

[68] D. Wolf, H. Jagodzinski, and W. Moritz. Diffuse LEED intensities of disordered crystal surfaces : III. LEED investigation of the disordered (110) surface of gold. *Surf. Sci.*, 77:265–282, 1978.

[69] G. L. Kellogg. Direct Observations of the (1 × 2) Surface Reconstruction on the Pt(110) Plane. *Phys. Rev. Lett.*, 55(20):2168–2171, Nov 1985.

[70] D. G. Fedak and N. A. Gjostein. Structure and Stability of the (100) Surface of Gold. *Phys. Rev. Lett.*, 16(5):171–172, Jan 1966.

[71] P. Heilmann, K. Heinz, and K. Muller. The superstructures of the clean Pt(100) and Ir(100) surfaces. *Surf. Sci.*, 83:487–497, 1979.

[72] J. Furthmüller, G. Kresse, J. Hafner, R. Stumpf, and M. Scheffler. Site-Selective Adsorption of C Atoms on Al(111) Surfaces. *Phys. Rev. Lett.*, 74(25):5084–5087, Jun 1995.

[73] J. R. Noonan and H. L. Davis. Truncation-induced multilayer relaxation of the A1(110) surface. *Phys. Rev. B*, 29(8):4349–4355, Apr 1984.

[74] J. Burchhardt, M. M. Nielsen, D. L. Adams, E. Lundgren, and J. N. Andersen. Structure of Al(111)-($\sqrt{3} \times \sqrt{3}$)$R30°$-Na: A LEED study. *Phys. Rev. B*, 50(7):4718–4724, Aug 1994.

[75] Mikael Borg, Martin Birgersson, Maria Smedh, Anders Mikkelsen, David L. Adams, Ralf Nyholm, Carl-Olof Almbladh, and Jesper N. Andersen. Experimental and theoretical surface core-level shifts of aluminum (100) and (111). *Phys. Rev. B*, 69(23):235418, 2004.

[76] J. H. Petersen, A. Mikkelsen, M. M. Nielsen, and D. L. Adams. Structure of Al(100)-$c(2\times2)$-Li: A binary surface alloy. *Phys. Rev. B*, 60(8):5963–5968, Aug 1999.

[77] A. Kiejna, J. Peisert, and P. Scharoch. Quantum-size effect in thin Al(110) slabs. *Surf. Sci.*, 432:54–60, 1999.

[78] Schöchlin, J. and Bohnen, K.P. and Ho, K.M. Structures and dynamics at the Al(111)-surface. *Surf. Sci.*, 324:113–121, 1995.

[79] H. Ohtani, M.A. Van Hove, and G.A. Somorjai. Leed intensity analysis of the surface structures of Pd(111) and of CO adsorbed on Pd(111) in a ($\sqrt{3} \times \sqrt{3}$)R30 ° arrangement. *Surf. Sci.*, 187(2-3):372–386, 1987.

[80] Y. Kuk, L. C. Feldman, and P. J. Silverman. Transition from the Pseudomorphic State to the Nonregistered State in Epitaxial Growth of Au on Pd(111). *Phys. Rev. Lett.*, 50(7):511–514, Feb 1983.

[81] J. Quinn, Y. S. Li, D. Tian, H. Li, F. Jona, and P. M. Marcus. Anomalous multilayer relaxation of Pd001. *Phys. Rev. B*, 42(17):11348–11351, Dec 1990.

[82] R. J. Behm, K. Christmann, G. Ertl, and M. A. Van Hove. Adsorption of CO on Pd(100). *J. Chem. Phys.*, 73(6):2984–2995, 1980.

[83] C. J. Barnes, M. Q. Ding, M. Lindroos, R. D. Diehl, and D. A. King. A LEED structural study of the Pd110-(1x1) surface and an alkali-metal-induced (1x2) surface reconstruction. *Surf. Sci.*, 162(1-3):59–73, 1985.

[84] M. Skottke, R. J. Behm, G. Ertl, V. Penka, and W. Moritz. LEED structure analysis of the clean and (2 x 1)H covered Pd(110) surface. *J. Chem. Phys.*, 87(10):6191–6198, 1987.

[85] D. L. Adams, H. B. Nielsen, and M. A. Van Hove. Quantitative analysis of low-energy-electron diffraction: Application to Pt(111). *Phys. Rev. B*, 20(12):4789–4806, Dec 1979.

[86] Roland Feder, Heribert Pleyer, Peter Bauer, and Norbert Muller. Spin polarization in low-energy electron diffraction: Surface analysis of Pt(111). *Surf. Sci.*, 109:419–434, 1981.

[87] J. F. Van Der Veen, R. G. Smeenk, R. M. Tromp, and F. W. Saris. Relaxation effects and thermal vibrations in a Pt(111) surface measured by medium energy ion scattering. *Surf. Sci.*, 79:219–230, 1979.

[88] J. A. Davies, T. E. Jackman, D. P. Jackson, and P. R. Norton. Surface relaxation of the platinum (100)-(1 x 1) surface at 175 k. *Surf. Sci.*, 109:20–28, 1981.

[89] Erik C. Sowa, M. A. Van Hove, and D. L. Adams. The missing-row model for the reconstructed Pt(110)-(1 x 2) surface: A leed intensity analysis showing multilayer distortions. *Surf. Sci.*, 199:174–182, 1988.

[90] E. Vlieg, I. K. Robinson, and K. Kern. Relaxations in the missing-row structure of the (1 x 2) reconstructed surfaces of Au(110) and Pt(110). *Surf. Sci.*, 233:248–254, 1990.

[91] Noboru Takeuchi, C. T. Chan, and K. M. Ho. Au(111): A theoretical study of the surface reconstruction and the surface electronic structure. *Phys. Rev. B*, 43(17):13899–13906, Jun 1991.

[92] Byung Deok Yu and Matthias Scheffler. Physical origin of exchange diffusion on fcc(100) metal surfaces. *Phys. Rev. B*, 56(24):R15569–R15572, Dec 1997.

[93] B. M. Ocko, Doon Gibbs, K. G. Huang, D. M. Zehner, and S. G. J. Mochrie. Structure and phases of the Au(001) surface: Absolute x-ray reflectivity. *Phys. Rev. B*, 44(12):6429–6443, Sep 1991.

[94] K. P. Bohnen and K. M. Ho. Surface structure of gold and silver (110)-surfaces. *Electrochim. Acta*, 40:129–132, 1995.

[95] W. Moritz and D. Wolf. Multilayer distortion in the reconstructed (110) surface of Au. *Surf. Sci.*, 163:L655–L665, 1985.

[96] M. Copel and T. Gustafsson. Structure of Au(110) Determined with Medium-Energy-Ion scattering. *Phys. Rev. Lett.*, 57(6):723–726, Aug 1986.

[97] G. Teeter and J. L. Erskine. Surface relaxation of Ti(0001): Influence of hydrogen contamination. *Phys. Rev. B*, 61(20):13929–13935, May 2000.

[98] Vincenzo Fiorentini and M. Methfessel. Extracting convergent surface energies from slab calculations. *J. Phys.: Condens. Matter*, 8(36):6525–6529, 1996.

[99] Alexander Y. Lozovoi and Ali Alavi. Reconstruction of charged surfaces: General trends and a case study of Pt(110) and Au(110). *Phys. Rev. B*, 68(24):245416, Dec 2003.

[100] Ann E. Mattsson and Walter Kohn. An energy functional for surfaces. *J. Chem. Phys.*, 115(8):3441–3443, 2001.

[101] R. Armiento and A. E. Mattsson. Functional designed to include surface effects in self-consistent density functional theory. *Phys. Rev. B*, 72(8):085108, 2005.

[102] Alfonso Baldereschi, Stefano Baroni, and Raffaele Resta. Band Offsets in Lattice-Matched Heterojunctions: A Model and First-Principles Calculations for GaAs/AlAs. *Phys. Rev. Lett.*, 61(6):734–737, Aug 1988.

[103] C. J. Fall, N. Binggeli, and A. Baldereschi. Theoretical maps of work-function anisotropies. *Phys. Rev. B*, 65(4):045401, Dec 2001.

[104] C. J. Fall, N. Binggeli, and A. Baldereschi. Work Functions at Facet Edges. *Phys. Rev. Lett.*, 88(15):156802, Apr 2002.

[105] J. K. Grepstad, P. O. Gartland, and B. J. Slagsvold. Anisotropic work function of clean and smooth low-index faces of aluminium. *Surf. Sci.*, 57:348–362, 1976.

[106] Adam Kiejna, Georg Kresse, Jutta Rogal, Abir De Sarkar, Karsten Reuter, and Matthias Scheffler. Comparison of the full-potential and frozen-core approximation approaches to density-functional calculations of surfaces. *Phys. Rev. B*, 73(3):035404, 2006.

[107] R. Gomer. Metallicity of Ultrathin Metal Layers. *Acc. Chem. Res.*, 29(6):284–291, 1996.

[108] G. N. Derry and Zhang Ji-Zhong. Work function of Pt(111). *Phys. Rev. B*, 39(3):1940–1941, Jan 1989.

[109] C. J. Fall, N. Binggeli, and A. Baldereschi. Work-function anisotropy in noble metals: Contributions from d states and effects of the surface atomic structure. *Phys. Rev. B*, 61(12):8489–8495, Mar 2000.

[110] Herbert B. Michaelson. The work function of the elements and its periodicity. *J. Appl. Phys.*, 48(11):4729–4733, 1977.

[111] F. R. de Boer, R. Boom, W. C. M. Mattens, A. R. Miedema, and A. K. Niessen. *Cohesion in Metals*. North Holland, Amsterdam, 1988.

[112] Sumio Iijima. Helical microtubules of graphitic carbon. *Nature*, 354:56–58, 1991.

[113] O. Dubay and G. Kresse. Accurate density functional calculations for the phonon dispersion relations of graphite layer and carbon nanotubes. *Phys. Rev. B*, 67(3):035401, Jan 2003.

[114] Stephanie Reich, Christian Thomsen, and Janina Maultzsch. *Carbon Nanotubes: Basic Concepts and Physical Properties*. Wiley-VCH, 2004.

[115] V. Georgakilas, K. Kordatos, M. Prato, D.M. Guldi, M. Holzinger, and A. Hirsch. Organic Functionalization of Carbon Nanotubes. *Journal of the American Chemical Society*, 124(5):760–761, 2002.

[116] Michael S. Strano, Christopher A. Dyke, Monica L. Usrey, Paul W. Barone, Mathew J. Allen, Hongwei Shan, Carter Kittrell, Robert H. Hauge, James M. Tour, and Richard E. Smalley. Electronic Structure Control of Single-Walled Carbon Nanotube Functionalization. *Science*, 301(5639):1519–1522, 2003.

[117] K. Kamaras, M. E. Itkis, H. Hu, B. Zhao, and R. C. Haddon. Covalent Bond Formation to a Carbon Nanotube Metal. *Science*, 301(5639):1501–, 2003.

[118] Satoru Suzuki, Yoshio Watanabe, Yoshikazu Homma, Shin ya Fukuba, Stefan Heun, and Andrea Locatelli. Work functions of individual single-walled carbon nanotubes. *Applied Physics Letters*, 85(1):127–129, 2004.

[119] Ken ichi Okazaki, Yoshihiro Nakato, and Kei Murakoshi. Absolute potential of the Fermi level of isolated single-walled carbon nanotubes. *Phys. Rev. B*, 68(3):035434, 2003.

[120] Bin Shan and Kyeongjae Cho. First Principles Study of Work Functions of Single Wall Carbon Nanotubes. *Phys. Rev. Lett.*, 94(23):236602, 2005.

[121] Veronica Barone, Juan E. Peralta, Jamal Uddin, and Gustavo E. Scuseria. Screened exchange hybrid density-functional study of the work function of pristine and doped single-walled carbon nanotubes. *J. Chem. Phys.*, 124(2):024709, 2006.

[122] Jijun Zhao, Jie Han, and Jian Ping Lu. Work functions of pristine and alkali-metal intercalated carbon nanotubes and bundles. *Phys. Rev. B*, 65(19):193401, Apr 2002.

[123] I. Dabo, B. Kozinsky, N.E. Singh-Miller, and N. Marzari. Electrostatics in Periodic-boundary Conditions and Real-space Corrections. *Phys. Rev. B*, 77:115139, 2008.

[124] G. Makov and M. C. Payne. Periodic boundary conditions in ab initio calculations. *Phys. Rev. B*, 51(7):4014–4022, Feb 1995.

[125] M. R. Jarvis, I. D. White, R. W. Godby, and M. C. Payne. Supercell technique for total-energy calculations of finite charged and polar systems. *Phys. Rev. B*, 56(23):14972–14978, Dec 1997.

[126] Jörg Neugebauer and Matthias Scheffler. Adsorbate-substrate and adsorbate-adsorbate interactions of Na and K adlayers on Al(111). *Phys. Rev. B*, 46(24):16067–16080, Dec 1992.

[127] Peter A. Schultz. Local electrostatic moments and periodic boundary conditions. *Phys. Rev. B*, 60(3):1551–1554, Jul 1999.

[128] Bin Shan and Kyeongjae Cho. Ab initio study of Schottky barriers at metal-nanotube contacts. *Phys. Rev. B*, 70(23):233405, 2004.

[129] R. Saito, G. Dresselhaus, and M.S. Dresselhaus. *Physical Properties of Carbon Nanotubes*. Imperial College Press, London, 1998.

[130] Charles W. Bauschlicher. Hydrogen and fluorine binding to the sidewalls of a (10,0) carbon nanotube. *Chemical Physics Letters*, 322:237–241, 2000.

[131] Siu-Pang Chan, Gang Chen, X. G. Gong, and Zhi-Feng Liu. Chemisorption of Hydrogen Molecules on Carbon Nanotubes under High Pressure. *Phys. Rev. Lett.*, 87(20):205502, Oct 2001.

[132] Ruifang Li, Zhenfeng Shang, Guichang Wang, Yinming Pan, and Xuezhuang Zhao. Theoretical investigation on the hydrogenation of armchair single-walled carbon nanotubes. *Journal of Molecular Structure: THEOCHEM*, 635:203–210, 2003.

[133] K.A. Park, K. Seo, and Y.H. Lee. Adsorption of Atomic Hydrogen on Single-Walled Carbon Nanotubes. *Journal of Physical Chemistry B*, 109(18):8967–8972, 2005.

[134] Young-Su Lee and Nicola Marzari. Cycloaddition Functionalizations to Preserve or Control the Conductance of Carbon Nanotubes. *Phys. Rev. Lett.*, 97(11):116801, 2006.

[135] N.F. Mott. Note on the contact between a metal and an insulator or semiconductor. *Proceedings of the Cambridge Philosophical Society*, 34:568, 1938.

[136] W. Schottky. Halbleitertheorie der sperrschicht. *Naturwissenschaften*, 26(52):843, 1938.

[137] François Léonard and J. Tersoff. Role of Fermi-Level Pinning in Nanotube Schottky Diodes. *Phys. Rev. Lett.*, 84(20):4693–4696, May 2000.

[138] J. Appenzeller, J. Knoch, V. Derycke, R. Martel, S. Wind, and Ph. Avouris. Field-Modulated Carrier Transport in Carbon Nanotube Transistors. *Phys. Rev. Lett.*, 89(12):126801, Aug 2002.

[139] François Léonard and J. Tersoff. Novel Length Scales in Nanotube Devices. *Phys. Rev. Lett.*, 83(24):5174–5177, December 1999.

[140] Ali Javey, Jing Guo, Qian Wang1, Mark Lundstrom, and Hongjie Dai. Ballistic carbon nanotube field-effect transistors. *Nature*, 424:654–657, 2003.

[141] J. Appenzeller, M. Radosavljević, J. Knoch, and Ph. Avouris. Tunneling Versus Thermionic Emission in One-Dimensional Semiconductors. *Phys. Rev. Lett.*, 92(4):048301, Jan 2004.

[142] W. Zhu and E. Kaxiras. The Nature of Contact between Pd Leads and Semiconducting Carbon Nanotubes. *Nano Letters*, 6(7):1415–1419, 2006.

[143] J. J. Palacios, P. Tarakeshwar, and Dae M. Kim. Metal contacts in carbon nanotube field-effect transistors: Beyond the Schottky barrier paradigm. *Physical Review B (Condensed Matter and Materials Physics)*, 77(11):113403, 2008.

[144] Khorgolkhuu Odbadrakh, Pawel Pomorski, and Christopher Roland. Ab initio band bending, metal-induced gap states, and Schottky barriers of a carbon and a boron nitride nanotube device. *Phys. Rev. B*, 73(23):233402, 2006.

[145] S. Dag, O. Gulseren, S. Ciraci, and T. Yildirim. Electronic structure of the contact between carbon nanotube and metal electrodes. *Applied Physics Letters*, 83(15):3180–3182, 2003.

[146] Susumu Okada and Atsushi Oshiyama. Electronic Structure of Semiconducting Nanotubes Adsorbed on Metal Surfaces. *Phys. Rev. Lett.*, 95(20):206804, 2005.

[147] Noejung Park and Suklyun Hong. Electronic structure calculations of metal-nanotube contacts with or without oxygen adsorption. *Phys. Rev. B*, 72(4):045408, 2005.

[148] Noejung Park, Donghoon Kang, Suklyun Hong, and Seungwu Han. Pressure-dependent Schottky barrier at the metal-nanotube contact. *Applied Physics Letters*, 87(1):013112, 2005.

[149] Wenguang Zhu and Efthimios Kaxiras. Schottky barrier formation at a carbon nanotube—metal junction. *Applied Physics Letters*, 89(24):243107, 2006.

[150] Yongqiang Xue and Supriyo Datta. Fermi-Level Alignment at Metal-Carbon Nanotube Interfaces: Application to Scanning Tunneling Spectroscopy. *Phys. Rev. Lett.*, 83(23):4844–4847, Dec 1999.

[151] P. Giannozzi, R. Car, and G. Scoles. Oxygen adsorption on graphite and nanotubes. *The Journal of Chemical Physics*, 118(3):1003–1006, 2003.

[152] A. Baldereschi. Mean-value point in the brillouin zone. *Phys. Rev. B*, 7(12):5212–5215, Jun 1973.

[153] D. J. Chadi and Marvin L. Cohen. Special points in the brillouin zone. *Phys. Rev. B*, 8(12):5747–5753, Dec 1973.